University of Southampton

Faculty of Environmental and Life Sciences

School of Ocean and Earth Science

Biogeochemical Cycling of Iron and Chromium in the North Atlantic Ocean: Insights from Stable Iron and Chromium Isotopes

by

Wenhao Wang

ORCID ID 0000-0003-4198-6681

Thesis for the degree of Doctor of Philosophy

August 2020

University of Southampton

Abstract

Faculty of Environmental and Life Sciences

School of Ocean and Earth Science

Doctor of Philosophy

Biogeochemical Cycling of Iron and Chromium in the North Atlantic Ocean:

Insights from Stable Iron and Chromium Isotopes

by

Wenhao Wang

Many trace metals are essential for phytoplankton growth, but there is ongoing debate about the consequences of global warming on primary productivity because the processes that regulate the supply of these metals are poorly understood. This thesis utilises the stable isotope compositions of iron (Fe) and chromium (Cr) to provide new insights as to the provenance of metal inputs to the ocean, and the effects of biogeochemical cycling and redox processes on metal availability.

Chemical processes in the hydrothermal plume are demonstrated to regulate the evolution of the Fe isotope signature (δ^{56}Fe) of hydrothermal Fe at hydrothermal vent fields (Beebe and Von Damm) in the Caribbean Sea. The δ^{56}Fe of total dissolvable Fe evolves to higher values as Fe-sulfide particles fall out of the plume at Beebe. The δ^{56}Fe value of dissolved Fe (dFe) in the near-field plumes was lower (as low as −4.08‰) than it was in the hydrothermal vent fluids (−0.28‰), due to oxidation of Fe(II) and precipitation of the Fe-(oxyhydr)oxides that form. The vent fluid Fe/H_2S ratio and the Fe(II) oxidation rate are shown to be the principal controls on the δ^{56}Fe signature of dFe that is delivered to the ocean interior.

For the first time, the Fe and Cr isotopic compositions of seawater in samples collected through hydrothermal plumes on the Mid-Atlantic Ridge (TAG and Rainbow vent fields) were measured. It is shown that the Fe and Cr isotope profiles through the hydrothermal plumes are the mirror image of each other, providing compelling evidence for coupled cycling of Fe and Cr. Oxidation of Fe(II) and precipitation of Fe-(oxyhydr)oxides account for the low δ^{56}Fe values of dFe (as low as −1.91‰ at TAG and −6.95‰ at Rainbow). At the same time, Cr(VI) appears to be reduced to Cr(III), as indicated by elevated Cr isotope (δ^{53}Cr) values compared to background seawater (by up to +0.13‰ and +0.60‰ respectively). The δ^{56}Fe of dFe evolves to heavier values (−0.44 to 0.23‰) in the distal part of the plume, likely controlled by exchange of Fe between the dissolved and particulate fraction. The δ^{56}Fe value of the 'stabilised' Fe can nevertheless be used to distinguish input of hydrothermal Fe from other Fe sources (e.g. atmospheric dust). Scavenging of Cr(III) by Fe-(oxyhydr)oxide particles in the hydrothermal plume means that high-temperature hydrothermal systems are a sink for seawater Cr, potentially removing up to 20% of the riverine input.

Full water column depth profiles of dissolved Cr and δ^{53}Cr were obtained for three stations in the sub-tropical North Atlantic. Subsurface waters were depleted in Cr, and enriched in heavy Cr isotopes, relative to deeper waters. High δ^{53}Cr values (up to 1.4‰) in subsurface waters are not directly controlled by levels of oxygen or biological uptake, but are consistent with preferential removal of light Cr isotopes onto authigenic Fe particles. Regeneration of Cr in deeper waters leads to subtly increased levels of Cr at individual sites, but this trend is more obvious at the global scale. Removal and regeneration of relatively isotopically light Cr can account for the distributions of Cr and Cr isotopes in the global ocean and the systematic relationship between δ^{53}Cr-ln[Cr] reported by other studies.

Table of Contents

Table of Contents ..... **i**

Table of Tables ..... **v**

Table of Figures ..... **vi**

Research Thesis: Declaration of Authorship ..... **ix**

Acknowledgements ..... **xi**

Definitions and Abbreviations ..... **xiii**

Chapter 1 Introduction **1**

1.1 Marine biogeochemical cycles of iron and chromium 1

1.1.1 Historical background of trace metal study in the oceans 1

1.1.2 Marine biogeochemical cycling of iron 1

1.1.3 Marine biogeochemical cycling of Cr 3

1.2 Iron and chromium isotope systematics in the ocean 5

1.2.1 Oceanic iron isotope cycle 5

1.2.2 Iron isotope systematics 7

1.2.3 Oceanic chromium isotope cycle 8

1.2.4 Chromium isotope systematics 10

1.3 Thesis outline 12

Chapter 2 Behaviour of iron isotopes in hydrothermal systems: Beebe and Von Damm vent fields on the Mid-Cayman ultraslow-spreading ridge **14**

2.1 Introduction 14

2.2 Sampling sites 15

2.3 Methods 17

2.3.1 Sample collection 17

2.3.2 Fe isotope analysis 17

2.3.3 Ancillary analyses 19

2.4 Results 19

2.4.1 Hydrothermal vent fluids 19

2.4.2 Dissolved and total dissolvable Fe concentrations in the hydrothermal plumes 21
2.4.3 Isotopic composition of dissolved and total dissolvable Fe in the hydrothermal plumes 22
2.4.4 Incubation experiment 23
2.5 Discussion 24
2.5.1 Fe isotope composition of the hydrothermal vent fluids 24
2.5.2 Fractionation of Fe isotopes in the buoyant plume 24
2.5.3 Evidence for Fe-sulfide precipitation in the buoyant plume 27
2.5.4 Controls on the δ^{56}Fe signature of dissolved Fe in hydrothermal plumes 29
2.6 Conclusions 31

Chapter 3 Impact of hydrothermal venting on iron and chromium supply to the North Atlantic Ocean 33

3.1 Introduction 33
3.2 Sampling sites 35
3.3 Methods 37
3.3.1 Sample collection 37
3.3.2 Incubation experiment 38
3.3.3 Fe and Cr isotope analysis 39
3.3.4 Ancillary analyses 41
3.3.5 Dilution factor calculations 41
3.4 Results 42
3.5 Discussion 45
3.5.1 Fe isotope behavior in the near-field hydrothermal plume 45
3.5.2 Cr isotope behavior in the near-field hydrothermal plume 51
3.5.3 Evolution of the hydrothermal δ^{56}Fe signal in the distal plume 53
3.5.4 Quantifying the hydrothermal contribution to the Fe inventory in the North Atlantic 56
3.5.5 Constraining the effect of hydrothermal activity on the oceanic Cr budget 60
3.6 Conclusions 62

Chapter 4 Biogeochemical cycling of chromium and chromium isotopes in the sub-tropical North Atlantic Ocean 64

4.1 Introduction 64

4.2 Materials and methods 66

4.2.1 Sample collection and oceanographic setting 66

4.2.2 Cr isotope analysis 68

4.2.3 Analysis of dissolved Fe concentration and other ancillary analyses 70

4.3 Results 70

4.4 Discussion 73

4.4.1 Potential sources of Cr to the North Atlantic 73

4.4.2 Removal of Cr in subsurface waters 74

4.4.3 Regeneration of Cr in deeper waters 76

4.4.4 Global correlation between seawater Cr and δ^{53}Cr 78

4.5 Conclusions 79

Chapter 5 Conclusions and outlook 81

5.1 Key findings 81

5.1.1 Iron isotope behaviour in hydrothermal systems 81

5.1.2 Coupled cycling of iron and chromium in hydrothermal plumes 82

5.1.3 Chromium biogeochemical cycling in the sub-tropical North Atlantic Ocean 82

5.2 Recommendations for further research 83

Appendix A Supporting information for Chapter 2 85

A.1 Compositions of all vent fluid samples collected on cruise JC82 85

A.2 The δ^{56}Fe values versus Mg concentration in Beebe and Von Damm vent fluids 86

A.3 Fe isotope compositions of dissolved and total dissolvable Fe in hydrothermal plumes at the Beebe and the Von Damm vent fields 87

A.4 Literature data for Fe isotope compositions in end-member vent fluids from contrasting types of hydrothermal systems 88

A.5 Literature data for Fe isotope compositions in hydrothermal plumes from contrasting types of hydrothermal systems 90

Appendix B Supporting information for Chapter 3 94

B.1 Supplementary information for analytical methods 94
B.2 Fe data for all samples measured in this study 98
B.3 Cr data for all samples measured in this study..... 101
B.4 Fe isotope compositions (δ^{56}Fe) of dFe in seawater samples from 8 stations of the GA13 transect 102

Appendix C Supporting information for Chapter 4 103

C.1 Cr data for all seawater samples measured in this study..... 103

List of Reference.....105

Table of Tables

Table 2-1 Composition of hydrothermal vent fluids from Beebe and Von Damm.....20

Table 3-1 Fe and Cr isotope compositions for method validation samples. 40

Table 3-2 Results of the Fe incubation experiments. 44

Table 3-3 Parameters used to calculate estimated variables (*f*, *F* and *X*; Section 3.5.1) that are utilised to constrain the Rayleigh model for investigating the effects of precipitation of Fe-sulfides and Fe-(oxyhydr)oxides. 49

Table 3-4 Results of the isotope mass balance calculation for the distal particle-rich plume sample. 56

Table 3-5 Quantification of the importance of hydrothermal source to the dissolved Fe inventory using two-component isotope mixing model.....58

Table 3-6 Quantification of the global high-temperature hydrothermal removal flux of Cr based on data from TAG and Rainbow vent fields respectively, and comparison with river input flux of Cr. 61

Table 4-1 Range of concentrations and fluxes of Cr inputs and outputs to/from the ocean.....65

Table of Figures

Figure 1-1 Schematic showing sources of Fe to the oceans and associated Fe isotope compositions. 6

Figure 1-2 Summary of iron isotope fractionation for different processes and/or reactions that may occur in oceanic settings. 7

Figure 1-3 Schematic showing the sources, sink, and internal cycling of Cr in the oceans. 9

Figure 1-4 Summary of chromium isotope fractionation associated with different processes and/or reactions occurring in oceanic settings. 11

Figure 2-1 Location of the Beebe and Von Damm vent fields on the Mid-Cayman spreading ridge. 16

Figure 2-2 (a) Concentrations of dissolved Fe (dFe) and total dissolvable Fe (TDFe), relative to vent fluid (VF) dilution factor at Beebe and Von Damm vent fields. **(b)** Fe isotope compositions of dFe and TDFe (δ^{56}dFe and δ^{56}TDFe), relative to vent fluid dilution factor at Beebe and Von Damm..... 22

Figure 2-3 (a) δ^{56}Fe relative to the fraction of dFe(II) oxidised to Fe(III). The observed δ^{56}dFe values in the near-field buoyant plumes at Beebe and Von Damm are explained by a Rayleigh fractionation model. **(b)** δ^{56}Fe relative to the fraction of TDFe lost from the plume at Beebe. 26

Figure 2-4 (a) Repeat sub-sampling of a niskin bottle (JC82-CTD11-N4) to show changes in dFe and δ^{56}dFe over time. **(b)** Variation in δ^{56}dFe as a function of the proportion of dFe removed from solution over the course of the incubation experiment. 28

Figure 2-5 Range of δ^{56}Fe of dFe measured to date in hydrothermal plumes..... 30

Figure 3-1 Locations of sampling stations at the TAG and Rainbow hydrothermal sites on the MAR, and LSS and Eh anomalies in water columns above the TAG and Rainbow vent fields. 36

Figure 3-2 Depth profiles of dissolved Fe and Cr concentrations, and δ^{56}Fe and δ^{53}Cr values, at the TAG station (**top panels**) and the Rainbow station (**bottom panels**). 43

Figure 3-3 Rayleigh models of Fe and Cr isotope fractionation in the TAG and Rainbow hydrothermal plumes. **Left panels**: δ^{56}Fe relative to the fraction of dFe(II)

oxidised to Fe(III). **Right panels**: δ^{53}Cr relative to the proportion of Cr(VI) reduced to Cr(III) and removed. 48

Figure 3-4 Cross plot of δ^{53}Cr values versus logarithmic Cr concentration, for new data from this study together with seawater data from the literature. 53

Figure 3-5 Evolution of dFe and δ^{56}dFe during hydrothermal plume dispersal. 55

Figure 3-6 (a) dFe concentration and δ^{56}dFe value in the upper 1000 m of the water column for stations around TAG. **(b)** δ^{56}dFe value in the deep layer from stations close to TAG and Rainbow. **(c)** dFe concentration and δ^{56}dFe value relative to apparent oxygen utilisation (AOU) from stations around Rainbow. 59

Figure 3-7 Schematic showing the coupled cycling of Fe and Cr in the hydrothermal plume. ...62

Figure 4-1 (a) Locations of sampling stations (1, 4 and 6) in the sub-tropical North Atlantic Ocean. **(b)** Salinity profiles for the three sampling stations. 67

Figure 4-2 Biogeochemical properties (dissolved oxygen, Chl-*a* concentration and turbidity) at Stations 1, 4, and 6. 71

Figure 4-3 (a) Full water column depth profiles of Cr concentration, δ^{53}Cr values, and dissolved Fe concentrations at Stations 1, 4, and 6. **(b)** Profiles of Cr concentrations, δ^{53}Cr values, and dissolved and colloidal Fe concentrations for the upper 900 m water depths at Stations 1, 4 and 6. 72

Figure 4-4 (a) δ^{53}Cr as a function of turbidity, Chl-*a* concentration, and dissolved oxygen, respectively. **(b)** Cr as a function of dFe concentration (left), δ^{53}Cr as a function of dFe concentration (middle), Cr as a function of apparent oxygen utilization (right). 76

Figure 4-5 Cr and δ^{53}Cr compared to dissolved oxygen concentrations in deep ocean waters (> 1000 m depth; excluding samples from the oxygen minimum zones).....77

Figure 4-6 (a) Relationship between δ^{53}Cr and ln[Cr] for new data from this study. **(b)** Relationship between δ^{53}Cr and ln[Cr] for the global open ocean seawater.....79

Research Thesis: Declaration of Authorship

Print name: **Wenhao Wang**

Title of thesis: **Biogeochemical Cycling of Iron and Chromium in the North Atlantic Ocean: Insights from Stable Iron and Chromium Isotopes**

I declare that this thesis and the work presented in it are my own and has been generated by me as the result of my own original research.

I confirm that:

1. This work was done wholly or mainly while in candidature for a research degree at this University;
2. Where any part of this thesis has previously been submitted for a degree or any other qualification at this University or any other institution, this has been clearly stated;
3. Where I have consulted the published work of others, this is always clearly attributed;
4. Where I have quoted from the work of others, the source is always given. With the exception of such quotations, this thesis is entirely my own work;
5. I have acknowledged all main sources of help;
6. Where the thesis is based on work done by myself jointly with others, I have made clear exactly what was done by others and what I have contributed myself;
7. None of this work has been published before submission

Signature: ..... Date:.....

Acknowledgements

First of all, I would like to express my sincere gratitude to my main thesis supervisor Prof. Rachael James, for her mentorship, guidance, insights, time and patience during the entire period of my PhD study. The opportunity to take on this exciting project is truly a prospect for my own personal development and in my progression as a scientist; I am very much motivated by Rachael's trust in me to carry out this work, her efforts in helping shape the project and review and revise the manuscripts, as well as her kind support and encouragement over the past four years.

I would also like to give sincere thanks to my co-supervisors Prof. Maeve Lohan, Prof. Douglas Connelly and Prof. Alessandra Tagliabue. I am very grateful for the continuous inspiration and help from Maeve; in addition, working with her on board RRS *James Cook* provided me with first hand exposure to large scale multi-disciplinary science. I received comments and praise for my work from Doug and Alessandra when I had a chance chatting with them. All my supervisors set an example of a world-class scientist, I do benefit a lot under their supervision.

A huge thank you to Dr. Alastair Lough and Dr. Heather Goring-Harford, from both of whom I received training to be a clean laboratory user and learned the methodologies for accurately determining stable Fe and Cr isotope compositions. Experiments central to this thesis would not have been achieved without their help. Enormous thanks to Prof. Andy Milton, Dr. Matt Cooper and Dr. Kate Peel for providing technical expertise and generous assistance with mass spectrometer operations alongside other practices in the clean lab. I also want to thank Prof. Andy Cundy for dropping in discussion meetings as panel chair for each of my progression review.

I appreciate the opportunity to participate on the NERC-funded UK GEOTRACES GA13 cruise (JC156) and to work as a member of the trace metal team and cooperate with diverse groups. I am also grateful to my supervisors for arranging the utilisation/collection of samples from the other two research cruises (JC082 and JC150). I gratefully acknowledge the support of NMF staff and captain and crew of RSS *James Cook*. I want to acknowledge the additional data (trace metal concentration and iron incubation), which are a great complement to this work, provided by Dr. Alastair Lough, Dr. Joesph Resing, Dr. Travis Mellet, David González-Santana and Koko Kunde.

I consider myself extremely lucky to have been studying within the NOC community with so many friends who are really warm. I am thankful for my office companion, Koko Kunde, over the years, who shows enthusiasm for work and life and pursuit of excellence. I appreciate the help, advice and encouragement from Dr. Amber Annett, Dr. Antony Birchill and Dr. Neil Waytt, whenever inside the laboratory or during a casual chat, on site or virtually. Special thanks go to Dr. Lise Artigue and

Clément Demacy; it has been pleasant memories working together and wishing you all the best in your future endeavors.

I would like to thank my housemates Hashan Kokuhennadige and Nathan Hubot, the birthday and the New Year's Eve dinners were indeed impressive. Besides, taking part in the Parkrun group as well as the Hillwalking squad has been nice experiences for me to refresh my mind and push the envelope. I would also like to show my thanks to all the Chinese friends who either stay at or have left from NOC, especially Dr. Chuang Xuan, Dr. Chongguang Luo, Dr. Xiongwei Niu, Dr. Yujiang Xie, Guantong Lv and Xiaode Zhou, for all the supports and companies.

My greatest appreciations go to my mum, dad and all my family, who give me unconditional and selfless love and understanding throughout the time - thank you for supporting me to fulfill my dreams.

When writing up this thesis, the world is experiencing an unprecedented challenge. However, people do have the hope, and they believe things will settle back to their original rhythms, season after season. Travelling back in time cannot change the future, but at this point it might be worth thinking what 'time' has taught us. 'I just try to live every day as if I've deliberately come back to this one day, to enjoy it, as if it was the full final day of my extraordinary, ordinary life. We are all travelling through time together, every day of our lives. All we can do is to do our best, to relish this remarkable ride.' ---- Richard Curtis *About Time*

Definitions and Abbreviations

AAIW ..... Antarctic Intermediate Water

ABW ..... Antarctic Bottom Water

Al ..... aluminium

AOU ..... apparent oxygen utilisation

aq ..... aqueous

BVF ..... Beebe vent field

cFe ..... colloidal iron

Chl-a ..... Chlorophyll-a

Cr ..... chromium

$CrO4^{2-}$ ..... chromate

CLSW ..... Classical Labrador Sea Water

CTD ..... conductivity, temperature and depth

dCr ..... dissolved chromium

dFe ..... dissolved iron

ESACW ..... East South Atlantic Central Water

Fe ..... iron

FeS ..... iron-sulfide

FIA ..... flow injection analysis

FeOOH ..... iron-(oxyhydr)oxide

HCl ..... hydrochloric acid

HEM ..... hematite

HNLC ..... high nutrient low chlorophyll

HNO_3 ..... nitric acid

H_2O_2 ..... hydrogen peroxide

H_2S ..... hydrogen sulfide

ICP-MS ..... inductively coupled plasma mass spectrometry

Definitions and Abbreviations

ISOW ..... Iceland-Scotland Overflow Water

LDPE ..... low density polyethylene

LPFe..... labile particulate iron

LSS..... light scattering sensor

MAR ..... Mid-Atlantic Ridge

MC-ICP-MS..... multicollector inductively coupled plasma mass spectrometry

Mg..... magnesium

mM ..... millimole per litre

Mn..... manganese

MnO_2..... manganese oxide

MQ..... Milli-Q water

MW ..... Mediterranean Water

NEADW ..... North East Atlantic Deep Water

NWABW..... North West Atlantic Bottom Water

nM..... nanomole per litre

O_2 ..... dissolved oxygen

OTE..... Ocean Test Equipment

PE ..... polyethylene

PFA..... perfluoroalkoxy

PES ..... polyethersulfone

pCr ..... particulate chromium

pFe ..... particulate iron

ROV..... remotely operated vehicle

sFe..... soluble iron

SD..... standard deviation

SML ..... surface mixed layer

SW..... seawater

TAG ..... Trans-Atlantic Geotraverse

TDFe .....total dissolvable iron

UCDW.....Upper Circumpolar Deep Water

VDVF.....Von Damm vent field

VF .....vent fluid

WNACW .....West North Atlantic Central Water

$\delta^{53}Cr$ .....chromium isotopic signature relative to NBS979 reference standard

$\delta^{56}Fe$ .....iron isotopic signature relative to IRMM reference standard

ε.....isotope fractionation factor

τ.....residence time

µM.....micromole per litre

Chapter 1 Introduction

1.1 Marine biogeochemical cycles of iron and chromium

1.1.1 Historical background of trace metal study in the oceans

Intense investigations on the concentrations, distributions, and chemical behaviors of trace metals in the world's oceans were initiated in the 1970s, with major advances in instrumental analysis and the development of clean sampling techniques (*Bruland and Lohan, 2006*). New instrumentation included the graphite furnace atomic absorption spectrometer and, more recently, inductively coupled plasma mass spectrometry (ICP-MS), which have enabled the rapid and precise analysis of seawater samples with vanishingly low metal concentrations. The development of sensitive shipboard methods for analysis of trace metal concentrations, such as stripping voltammetry and flow injection analysis (FIA) with either chemiluminescence or spectrophotometric detection, has allowed near real-time data collection during expeditions. Along with improvements in instrumental detection limits, has been an appreciation of the importance of clean sampling and analytical techniques for acquiring reliable and 'oceanographically consistent' data, free from contamination by metals that may be present in a ship or a laboratory (*Patterson, 1974; Boyle et al., 1977b*). Between 1972 and 1978, the international Geochemical Ocean Sections Study (GEOSECS) undertook a global survey of the three-dimensional distributions of chemical tracers in the oceans (*Moore, 1984*). However, this programme principally focused on analysis of nutrient elements and the inorganic carbonate system, and it was not until the early 2000s, when the international 'GEOTRACES' programme emerged, that a systematic effort was made to determine the large-scale distribution of trace metals and their isotopes in the marine environment (e.g. *Anderson, 2020*). At the same time, the development of the multiple-collector ICP-MS has facilitated high-precision analysis of metal isotope compositions in seawater.

The overarching aim of this thesis is to capitalize on these developments to better understand the sources and internal cycling of iron (Fe) and chromium (Cr) in the North Atlantic Ocean through the analysis of stable Fe and Cr isotopes.

1.1.2 Marine biogeochemical cycling of iron

Phytoplankton in the oceans are responsible for approximately half of the photosynthetic fixation of carbon (primary productivity) on Earth (*Field et al., 1998*). The high cellular requirements for iron (Fe) along with its low solubility and concentrations in seawater (*Moore et al., 2013*) render Fe the

key limiting nutrient for primary productivity in ~40% of the world's oceans (*Moore et al., 2001; Boyd and Ellwood, 2010*). These regions have been termed high nutrient low chlorophyll (HNLC) regions. Shipboard Fe-enrichment experiments confirmed that phytoplankton growth was limited by Fe availability (*Martin and Fitzwater 1988*) and led John Martin to formulate the 'Fe hypothesis' which proposed that variations in atmospheric CO_2 during glacial and interglacial cycles were driven by changes in Fe supply to the Southern Ocean (*Martin, 1990*). The recognition of the significance of Fe in the global carbon cycle has led to the incorporation of Fe cycling into global climate models (*Tagliabue et al., 2017*).

Iron is delivered to the oceans from multiple sources, while their individual fluxes vary spatially and temporarily. In the open ocean, the main source of dissolved Fe (dFe) has been considered to be atmospheric dust deposition (e.g. *Duce and Tindale, 1991*), although dust-derived particles are found to play additional role in scavenging seawater Fe (*Ye and Völker, 2017*). The North Atlantic Ocean is heavily influenced by the Sahara dust (*Shelley et al., 2015*) and receives the highest atmospheric input (~43%) of the global ocean basins (*Jickells et al., 2005*). River waters have higher dissolved Fe concentrations than seawater, however, aggregation of Fe colloids and/or Fe-binding ligands causes removal of up to 90% of dFe in estuaries (*Boyle et al., 1977a; Bergquist and Boyle, 2006; Escoube et al., 2009*). As a result, the vast majority of Fe from this source does not reach the open ocean. Other freshwater fluxes of Fe to the ocean include sub-glacial and iceberg meltwaters (*Person et al., 2019; Hopwood et al., 2019*) but this source of Fe is largely restricted to polar regions. Diagenetic recycling of seabed sediments is another source of dissolved Fe to the ocean, and studies have demonstrated that Fe supply from continental margins may extend far beyond the coastal zone (*Elrod et al., 2004; Lam and Bishop, 2008; John et al., 2018*). Despite previous consensus that hydrothermal activity is not a major source of Fe because of precipitation of Fe-sulfides and Fe-(oxyhydr)oxides as the vent fluids mix with seawater (*German et al., 1991*), GEOTRACES efforts in the Atlantic, Pacific, Southern and Arctic oceans have observed compelling signals of Fe derived from hydrothermal vent fields along mid-ocean ridges many hundreds of kilometres away from their seabed source (*Saito et al., 2013; Resing et al., 2015; Klunder et al., 2011, 2012*), contributing to the deep ocean Fe inventory (*Tagliabue et al., 2010*).

Despite being the fourth most abundant element in the Earth's crust, dissolved Fe (operationally defined as <0.2 μm) is present at extremely low concentrations in most of the oceans, typically of the order of picomole to nanomole per liter. In oxic seawater, Fe is mainly found in its oxidised Fe(III) form which is highly insoluble and tends to aggregate into larger particles (>0.2 μm) and sink towards seafloor (*Ussher et al., 2004*). Elevated Fe(II) concentrations, above those anticipated by thermodynamic theoretical calculations, have been observed in surface waters as a result of photochemical reduction (*Barbeau et al., 2001*), in reducing environments such as oxygen minimum

zones (*Lohan and Bruland, 2008*), sediment pore waters (*Severmann et al., 2006*), and hydrothermal vent fluids (*Statham et al., 2005*).

The separation between dissolved and particulate iron phases is complicated by colloids, which are typically characterised as being between 0.02 and 0.2 μm diameter and play an important role in controlling the supply and removal processes of dFe (*Wu et al., 2001; Fitzsimmons et al., 2015; Kunde et al., 2019*). On the other hand, >99% of dissolved Fe measured in the oceans appears to be Fe complexed by organic ligands (*Gledhill and Buck, 2012*), which maintains higher concentrations of dFe than the theoretically calculated solubility limit. Modelling studies have investigated the impacts of the Fe-binding ligand pool on atmospheric CO_2 levels (*Tagliabue et al., 2014*) and on long-range transport of Fe from point sources (e.g. hydrothermal vents; *Resing et al., 2015*).

Superimposed on its low concentration is the 'hybrid' nature of Fe, whereby it displays a combined nutrient-type and scavenged-type vertical distribution (*Bruland and Lohan, 2004*). Scavenging, which refers to adsorption of dFe onto biogenic and lithogenic particle surfaces, occurs throughout the water column and accounts for the short residence time of Fe (~100 yr in intermediate to deep waters) relative to the mixing time of the ocean (~1000 yr) (*Boyd and Ellwood, 2010*). Scavenging is the main removal pathway of Fe from the oceans (*Ussher et al., 2004; Boyd and Ellwood, 2010*). As Fe-containing particles sink through the ocean interior, Fe gradually undergoes remineralisation, which may lead to increased dFe concentrations with depth. Recent modelling studies have suggested that the Fe cycling in intermediate ocean waters is mainly controlled by the opposing effects of scavenging and regeneration (*Tagliabue et al., 2019*).

1.1.3 Marine biogeochemical cycling of Cr

In Earth surface environments, chromium (Cr) has two stable oxidation states, Cr(VI) and Cr(III). The oxidation state of Cr in aqueous solutions is governed by the system's redox potential (Eh) and pH conditions (*Ball and Nordstorm, 1998*). Cr(VI), which is most commonly present as oxyanion species CrO_4^{2-} (chromate) or $HCrO_4^-$ (bichromate), is highly soluble and stable at seawater pH and redox conditions (*Elderfield, 1970*). Cr(III) is the main Cr species at low Eh conditions, and usually forms hydrolyzed $CrOH^{2+}$, $Cr(OH)_3$, or $Cr(OH)_4^-$ species (dependent on pH) that are sparingly soluble (*Rai et al., 1987*). Earlier studies focusing on pollution remediation showed that, due to the contrasting geochemical behaviors of Cr(VI) and Cr(III), the Cr reduction process renders toxic Cr(VI) in the environment immobile and less toxic (e.g. *Blowes et al., 1997; Loyaux-Lawniczak et al., 2001*). As Cr is a redox sensitive element, more recent efforts have utilised the authigenic enrichments of Cr in ancient sediments as a proxy for reconstruction of paleoredox conditions (e.g. *Tribovillard et al., 2006; Reinhard et al., 2013*).

Rivers are the main source of dissolved Cr to the ocean (*Bonnand et al., 2013; Reinhard et al., 2013*). Cr is mainly in the form of Cr(III) in rocks, but weathering reactions driven by Mn-oxides oxidise Cr(III) as it is released from silicate rocks (*Frei et al., 2009*), so principally Cr(VI) is delivered to the oceans via rivers *(Cranston and Murray, 1980)*. Atmospheric deposition is a major source of many trace metals to the ocean and may result in elevated concentrations of Cr in surface seawater in some parts of the oceans (*Achterberg and van den Berg, 1997*). Whether hydrothermal vents are a net source or sink of Cr is not yet clear (*German et al., 1991; Sander and Koschinsky, 2000*), and estimated hydrothermal Cr fluxes vary by orders of magnitudes (*Rudnicki & Elderfield, 1993; Reinhard et al., 2013*). Cr is removed from the oceanic inventory through reduction of Cr(VI), scavenging onto settling particles and burial as Cr(III) in reducing and/or anoxic sediments (*Reinhard et al., 2014; Gueguen et al., 2016*). Therefore, marine sediments are considered as the major sink for seawater Cr.

Cr is present in typical concentrations of 0.9 to 6.5 nM in seawater (*Campbell and Yeats, 1981; Cranston, 1983; Jeandel and Minster, 1984; Achterberg and van den Berg, 1997; Sirinawin et al., 2000; Connelly et al., 2006; Bonnard et al., 2013; Scheiderich et al., 2015*) and has a relatively long residence time of ~3000 to 40000 years (*Campbell and Yeats, 1984; Reinhard et al., 2013; McClain and Maher, 2016*). The distribution of Cr in the oceans is similar to that of the nutrient elements, with modest depletion of Cr in surface ocean relative to the deep ocean (*Jeandel and Minster, 1987; Sirinawin et al., 2000*). Low Cr concentrations in surface waters are thought to be due to biologically mediated reduction and scavenging but this is still debated (*Achterberg and van den Berg, 1997; Connelly et al., 2006; Semeniuk et al., 2016*).

Laboratory-based studies have shown that aqueous Cr(VI) is readily reduced by a diversity of electron donors including dissolved Fe(II), Fe(II)-bearing minerals, hydrogen sulfide (H_2S) and organic matter. Reduction of Cr(VI) is effective in the presence of Fe(II) or Fe(II)-bearing minerals (*Eary and Rai, 1988; Fendorf and Li, 1996; Buerge and Hug, 1999*) and experiments have shown that Cr(VI) competes with O_2 in the oxidation of Fe(II) even in oxic environments (*Buerge and Hug, 1997; Pettine et al., 1998*):

$$Cr(VI)\ (aq) + 3Fe(II)\ (aq) \rightarrow Cr(III)\ (aq) + 3Fe(III)\ (aq) \qquad (1\text{-}1)$$

Reaction (1-1) is rapid and complete at both high and low pH although the products become insoluble at pH >4 (*Fendorf and Li, 1996*). Under anoxic conditions, dissolved H_2S may be the dominant reductant of Cr(VI) at low pH (<5.5) (*Pettine et al., 1994; Fendorf et al., 2000*). In addition, a wide range of organic molecules are also known to cause Cr reduction (*Schroeder and Lee, 1975; Deng and Stone, 1996*).

Microbial activity is another important mechanism for Cr(VI) reduction in the presence of Cr-reducing microorganisms and abundant electron donors (e.g. *Turick et al., 1996; Middleton et al., 2003*). Cr is not thought to be an essential nutrient to marine phytoplankton, however, biologically mediated reduction of Cr(VI) to Cr(III) could occur in surface seawater as suggested by field observations (*Achterberg and van den Berg, 1997; Connelly et al., 2006*) and this Cr(III) can be subsequently sequestered into phytoplankton via extracellular adsorption and/or internalization (*Semeniuk et al., 2016*).

In aqueous environments, the presence of Cr (III) at higher levels than thermodynamic predictions (*Pettine and Millero, 1990*) may reflect differences in reduction and oxidation rates. The strong kinetic stability of Cr(III) means that the rate of oxidation of Cr(III) by dissolved O_2 is sluggish (*Schroeder and Lee, 1975*), whereas Cr(III) oxidation by manganese-oxides (MnO_2) that are generated through reaction of Mn(II) with O_2 is fast (*Frei et al., 2009; Crowe et al., 2013*). Laboratory experiments investigated the oxidation kinetics of aqueous Cr(III) or Cr-bearing minerals catalysed by manganese minerals, indicated that MnO_2 is the preferred electron accepter over O_2 (*Schroeder and Lee, 1975; Eary and Rai, 1987; Oze, 2007*). It has also been argued that oxidation of Cr (III) could be induced by hydrogen peroxide (H_2O_2) that is produced in the euphotic zone of the water column and in serpentinization systems (*Pettine and Millero, 1990; Oze, 2016*).

1.2 Iron and chromium isotope systematics in the ocean

1.2.1 Oceanic iron isotope cycle

Iron has four stable isotopes ^{54}Fe, ^{56}Fe, ^{57}Fe and ^{58}Fe, with natural atomic abundances of 5.82%, 91.66%, 2.19% and 0.33%, respectively. Fe isotopic compositions are given as the ratio of ^{56}Fe to ^{54}Fe, normalised to the $^{56}Fe/^{54}Fe$ ratio of the IRMM-14 reference material, and expressed in δ notation as follows:

$$\delta^{56}Fe\ (‰) = [(^{56}Fe/^{54}Fe)_{sample}/(^{56}Fe/^{54}Fe)_{IRMM\text{-}14} - 1] \times 1000 \quad (1\text{-}2)$$

Fe isotopes are a promising tool for understanding the mechanisms driving the oceanic cycle of Fe, and studies are now emerging that utilise Fe isotopes to assess upper water column recycling (*Ellwood et al., 2015, 2019*) and the balance between different processes that regulate Fe behavior along ocean transport pathways (*Abadie et al., 2017; Klar et al., 2018*). In the euphotic zone, biological activity plays an important role in Fe transformation between the dissolved and particulate pools and therefore the Fe isotope dynamics (*Ellwood et al., 2015, 2020*). Remineralisation of organic matter and reversible scavenging with settling lithogenic particles in

the intermediate and deeper waters can redistribute dissolved Fe that is supplied from various sources (*Abadie et al., 2017; Klar et al., 2018*).

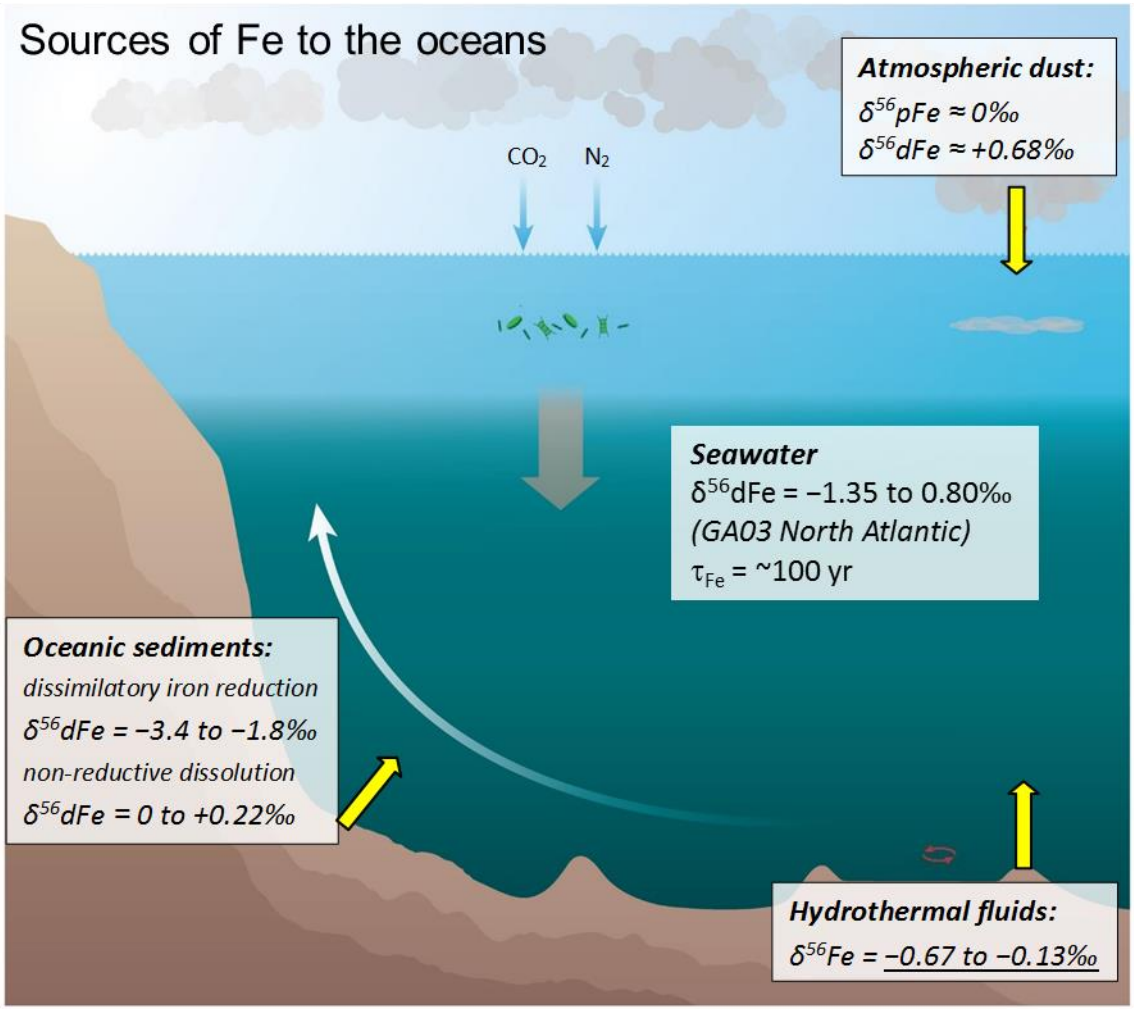

Figure 1-1 Schematic showing sources of Fe to the oceans and associated Fe isotope compositions. τ_{Fe} represents the residence time of Fe. References are given in the text.

The distinct δ^{56}Fe signatures of the different sources of Fe allow the identification and quantification of these sources to the oceans (*Conway and John, 2014*; Figure 1.1). The δ^{56}Fe signature of atmospheric aerosols is ~0‰ (*Waeles et al., 2007*), although the δ^{56}Fe value of Fe that dissolves from dust may be higher (~+0.68‰, *Conway and John, 2014*). Sedimentary Fe produced by dissimilatory Fe reduction carries a negative δ^{56}Fe signature (−3.4 to −1.8‰, *Homoky et al., 2009; Severmann et al., 2010; John et al., 2012*), whereas sedimentary Fe produced by non-reductive dissolution processes has a higher δ^{56}Fe value, ~0.22 ± 0.18‰ (*Homoky et al., 2013*). The δ^{56}Fe value of hydrothermal vent fluids is also distinct, −0.67 to −0.12‰ (*Sharma et al., 2001; Beard et al., 2003;*

Severmann et al., 2004; Rouxel et al., 2008; Bennett et al., 2009; Klar et al., 2017; Nasemann et al., 2018), raising the possibility that Fe isotopes could be used to trace hydrothermal inputs of Fe to the oceans.

1.2.2 Iron isotope systematics

Differences in the ^{56}Fe to ^{54}Fe ratio of a product and that of a reactant are given by the isotope fractionation factor (α):

$$\alpha = (^{56}Fe/^{54}Fe)_{Product}/(^{56}Fe/^{54}Fe)_{Reactant} \quad (1\text{-}3)$$

Alternatively, Fe isotope fractionation can be expressed as the difference between the $\delta^{56}Fe$ values of the product and the reactant, and conveniently expressed using ε notation:

$$\varepsilon\ (‰) = \delta^{56}Fe_{Product} - \delta^{56}Fe_{Reactant} \quad (1\text{-}4)$$

The fractionation factor expressions α and ε are related by the approximation:

$$\varepsilon\ (‰) \approx 1000 \times \ln(\alpha) \approx 1000 \times (\alpha - 1) \quad (1\text{-}5)$$

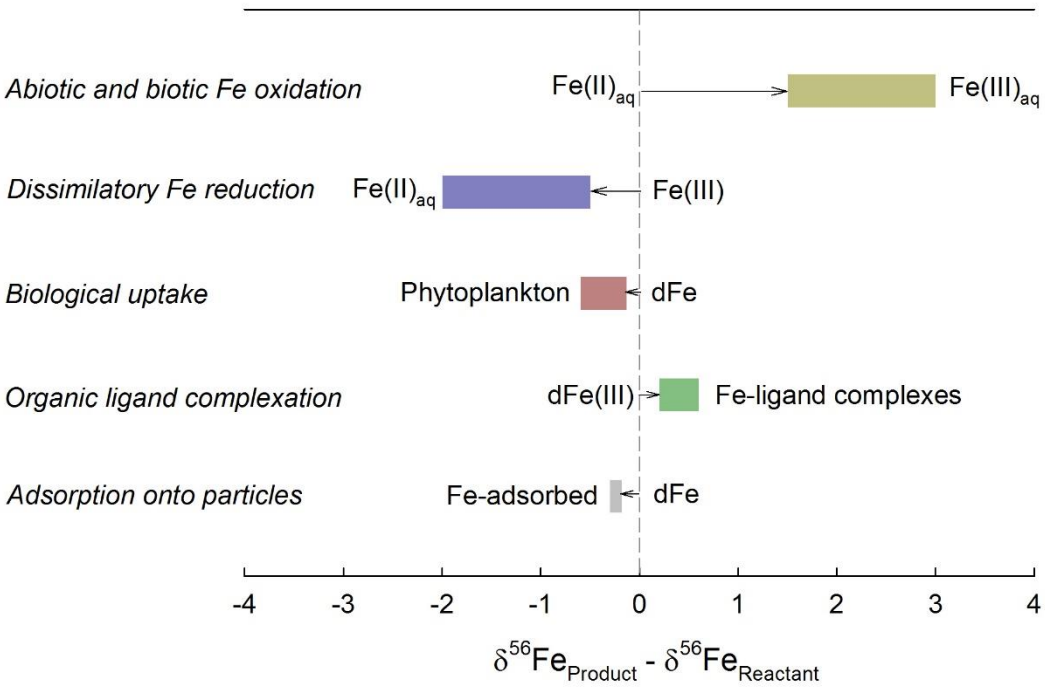

Figure 1-2 Summary of iron isotope fractionation for different processes and/or reactions that may occur in oceanic settings. References are given in the text.

Natural variations in stable Fe isotope compositions are caused by biological and abiotic redox processes that induce either kinetic or equilibrium fractionation effects (*Anbar, 2004; Johnson et al., 2018*). A brief summary of Fe isotope fractionation processes that may occur in oceanic settings is given in Figure 1.2.

Laboratory studies have shown that abiotic oxidation of $Fe(II)_{aq}$ enriches heavy Fe isotopes in $Fe(III)_{aq}$ (aq = aqueous), and the difference between $\delta^{56}Fe(III)_{aq}$ and $\delta^{56}Fe(II)_{aq}$ can be up to 3‰ at 20°C (*Johnson et al., 2002; Welch et al., 2003*). These findings are in agreement with thermodynamic calculations (*Anbar et al., 2005*). Fe isotope fractionation ($\delta^{56}Fe(III) - \delta^{56}Fe(II)_{aq}$ = 1.5 to 2.2‰) has also been observed during microbial Fe(II) oxidation (*Croal et al., 2004; Balci et al., 2006*).

Likewise, reduction of Fe(III) in the presence of dissimilatory Fe reducing bacteria has been shown to produce aqueous Fe(II) with $\delta^{56}Fe$ values that are 0.5-2‰ lower than the initial Fe(III) substrate (*Beard et al., 1999, 2003; Johnson et al., 2005; Icopini et al., 2004; Crosby et al., 2005*). Overall, large Fe isotope fractionations can occur during redox conversions, and reduced Fe(II) species are predicted to be isotopically lighter relative to Fe(III).

Previous studies have suggested that isotopically light Fe is preferentially utilised by diazotrophs and higher plants (*Zhu et al., 2002; Guelke and Von Blanckenburg, 2007*). Results from field observations along with mesocosm experiments in the Southern Ocean and the south-west Pacific are consistent with preferential uptake of light Fe isotopes by marine phytoplankton, with $\delta^{56}Fe_{Phytoplankton} - \delta^{56}Fe_{Seawater}$ = –0.13 to –0.60‰ (*Radic et al., 2011; Ellwood et al., 2015, 2020*). On the other hand, removal of relatively isotopically heavy Fe in (sub)surface seawater of the North Atlantic has been observed (*Conway and John., 2014; Klar et al., 2018*), hinting at a potentially different biological fractionation mechanism.

Organic ligand complexation with Fe seems to fractionate Fe isotopes. Experimentally derived equilibrium fractionation between Fe(III)-siderophore complexes and inorganic Fe(III) indicated a 0.2 to 0.6‰ difference between the two forms of Fe, with the ligand-binding Fe enriched in heavier Fe isotopes (*Dideriksen et al. 2008; Morgan et al., 2010*). Scavenging of dFe by particles may have a small isotope effect, with adsorbed Fe reported to be 0.18-0.30‰ lighter than the $\delta^{56}Fe$ of dFe (*John and Adkins, 2012; Radic et al., 2011*).

1.2.3 Oceanic chromium isotope cycle

Chromium has four stable isotopes ^{50}Cr (4.35%), ^{52}Cr (83.79%), ^{53}Cr (9.50%) and ^{54}Cr (2.36%). Cr isotopic compositions are given as the ratio of ^{53}Cr to ^{52}Cr, normalised to the $^{53}Cr/^{52}Cr$ ratio of a

manufactured Cr standard (chromium nitrate, referred to as NBS979), and expressed in δ notation as follows:

$$\delta^{53}Cr\ (‰) = [(^{53}Cr/^{52}Cr)_{sample}/(^{53}Cr/^{52}Cr)_{NBS979} - 1] \times 1000 \quad (1\text{-}6)$$

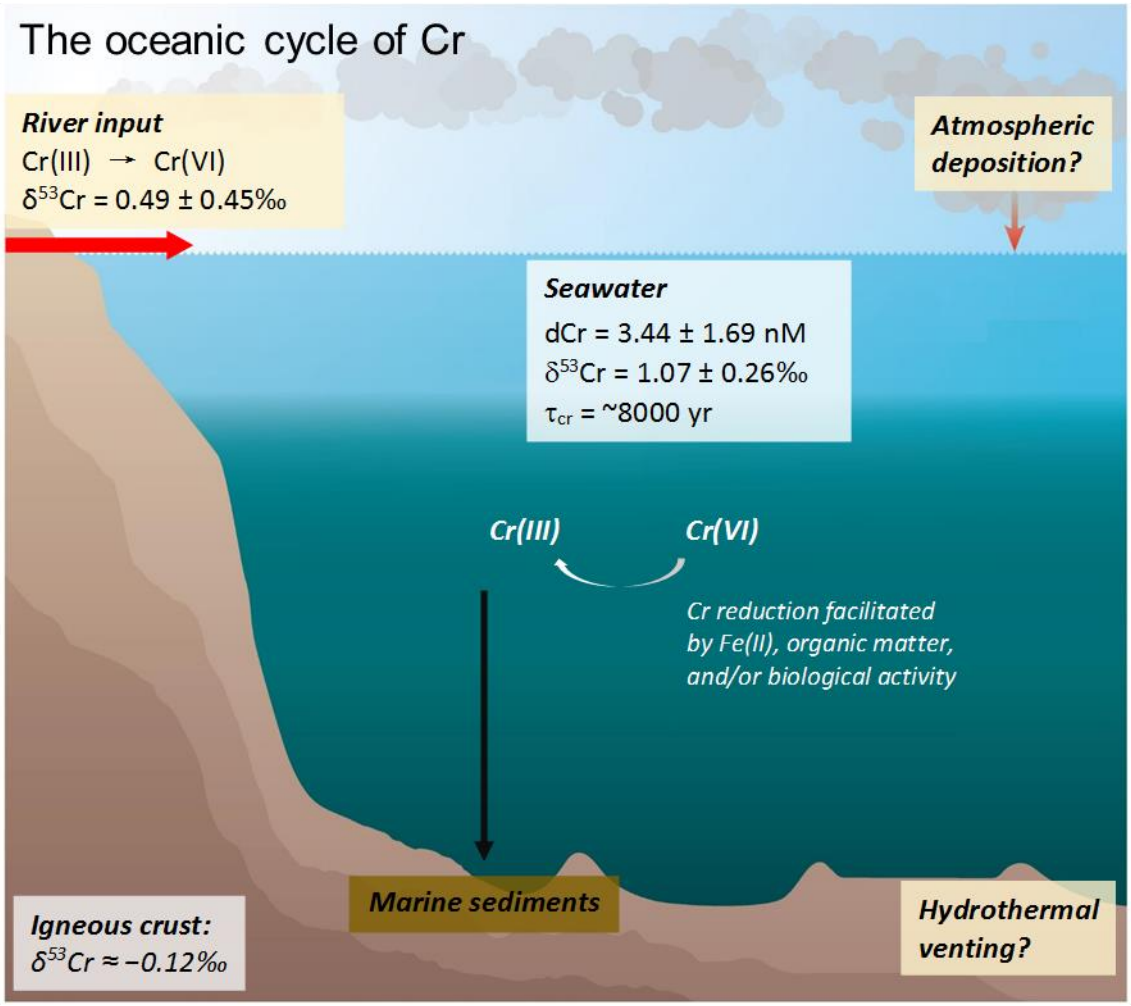

Figure 1-3 Schematic showing the sources, sink, and internal cycling of Cr in the oceans. τ_{Cr} represents the residence time of Cr. References for relevant data are given in the text.

A schematic of the oceanic Cr isotope cycle is shown in Figure 1.3. The $\delta^{53}Cr$ values for previously reported unpolluted river waters range from −0.3 to 1.7‰ (*Frei et al., 2014; Paulukat et al., 2015; D'Arcy; 2016; Wu et al., 2017; Andronikov et al., 2019*), generally higher than the value for silicate rocks (−0.12 ± 0.10‰; *Schoenberg et al., 2008*). The $\delta^{53}Cr$ signature of seawater from the open ocean measured to date is in the range between 0.4 and 1.6‰ (*Bonnand et al., 2013; Scheiderich et al., 2015; Goring-Harford et al., 2018; Moos and Boyle, 2019; Rickli et al., 2019; Janssen et al., 2020; Moos et al., 2020*). The variation in seawater $\delta^{53}Cr$ is suggested to be driven by reduction and

removal of Cr in surface waters and/or in oxygen minimum zones, and release of Cr(III) from settling particles (*Scheiderich et al., 2015*).

Cr(VI) in seawater can be reduced to Cr(III) by a diversity of electron donors including Fe(II) and organic matter. Cr(III) is relatively particle reactive and is subsequently scavenged onto settling particles and buried in reducing and anoxic sediments (*Reinhard et al., 2014; Gueguen et al., 2016*) which are the major sink for seawater Cr (*Reinhard et al., 2013*). The measured mean $\delta^{53}Cr$ values in the authigenic fractions of the reducing and anoxic marine sediments are reported to be between 0.45 and 0.61‰ in Peru margin sediments (*Gueguen et al., 2016; Bruggmann et al., 2019*) and between 0.38 and 0.53‰ in Cariaco Basin sediments (*Gueguen et al., 2016; Reinhard et al., 2014*). These values are systematically lower than the mean value for seawater ($\delta^{53}Cr$ = 1.07 ± 0.35‰; *Goring-Harford et al., 2020*), suggesting that Cr isotope fractionation occurs during reduction and scavenging of Cr. Nevertheless, these sedimentary $\delta^{53}Cr$ values are intermediate between seawater $\delta^{53}Cr$ and the $\delta^{53}Cr$ value of the riverine input, suggesting that Cr isotopes are approximately in mass balance in the modern ocean.

1.2.4 Chromium isotope systematics

Differences in the ^{53}Cr to ^{52}Cr ratio of a product and a reactant can be expressed in terms of the Cr isotope fractionation factor, α:

$$\alpha = (^{53}Cr/^{52}Cr)_{Product}/(^{53}Cr/^{52}Cr)_{Reactant} \quad (1\text{-}7)$$

Alternatively, the Cr isotope fractionation factor can be expressed as the difference between the $\delta^{53}Cr$ values of the product and the reactant, and conveniently expressed using ε notation:

$$\varepsilon\ (‰) = \delta^{53}Cr_{Product} - \delta^{53}Cr_{Reactant} \quad (1\text{-}8)$$

Again, the fractionation factor expressions are related by the approximation:

$$\varepsilon\ (‰) \approx 1000 \times \ln(\alpha) \approx 1000 \times (\alpha - 1) \quad (1\text{-}9)$$

A brief summary of Cr isotope fractionation processes in the ocean is given in Figure 1.4. Given the different geochemical behaviors of Cr(VI) and Cr(III), redox dependent reactions are thought to be the most significant control on natural Cr isotope variations. Isotopic equilibrium between Cr (III) and Cr (VI) takes place on timescales of months to thousands of years at circumneutral pH conditions (depending on Cr concentrations), but its impact is likely small in aqueous systems because the amount of Cr(III) on particle surfaces that is available for exchange is limited (*Wang et al., 2015*).

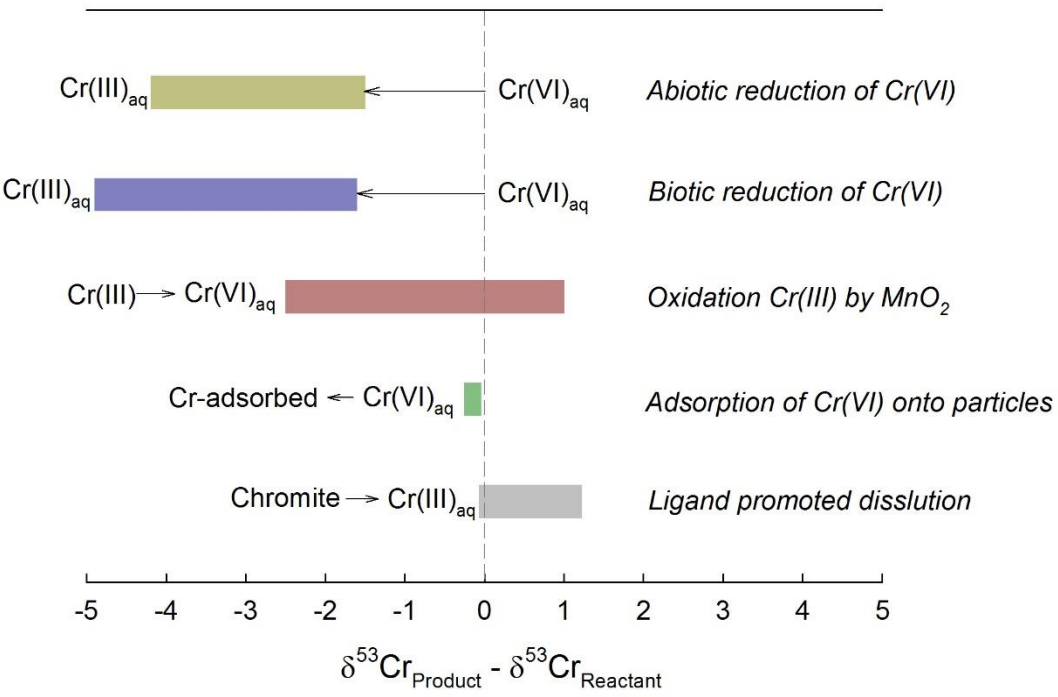

Figure 1-4 Summary of chromium isotope fractionation associated with different processes and/or reactions occurring in oceanic settings. References are given in the text.

Theoretical studies and laboratory experiments have confirmed that abiotic reduction of Cr(VI) leads to large mass-dependent fractionation, with enrichment of relatively light Cr isotopes in the Cr(III) that forms (*Ellis et al., 2002; Døssing et al., 2011; Kitchen et al., 2012; Basu and Johnson, 2012*). The direction of fractionation holds regardless of the reductant (Fe(II), Fe(II)-bearing minerals, organic matter), while the kinetic fractionation factors are variable (δ^{53}Cr(III) – δ^{53}Cr(VI) = −1.5 to −4.2‰). It has also been suggested that the fractionation factor may be influenced by the rate of Cr reduction and removal, with smaller fractionation associated with faster Cr removal (*Jamieson-Hanes et al., 2014*). Experimentally determined isotope fractionation factors for biotic Cr reduction have a relatively large range (δ^{53}Cr(III) – δ^{53}Cr(VI) = −1.6 to −4.9 ‰: *Sikora et al., 2008; Basu et al., 2014; Zhang et al., 2018, 2019*), depending on the type and concentration of electron donors as well as respiration pathways (aerobic vs. anaerobic).

Cr isotope fractionation caused by oxidation of Cr(III) by MnO_2 minerals is not well constrained as yet, and laboratory studies have reported variable δ^{53}Cr values for the resultant Cr(VI) pool ($\delta^{53}Cr_{Cr(VI)}$ = −2.5 to +1‰: *Bain and Bullen, 2005; Ellis et al., 2008*). This variation has been attributed to the multi-step path of the Cr oxidation reaction during which the formation and dissimilation of the unstable intermediates Cr(IV) and Cr(V) occurs (*Zink et al., 2010*).

Equilibrium fractionation of Cr isotopes between dissolved Cr(VI) and Cr(VI) adsorbed onto alumina, goethite and kaolin mineral surfaces was determined to be small ($\delta^{53}Cr_{adsorbed} - \delta^{53}Cr_{dissolved}$ = ~ –0.04 to –0.26‰: *Ellis et al., 2004; Frank et al., 2019*). Note that the adsorption of Cr(VI) in oceanic settings is likely to be even smaller because of the presence of seawater matrices that compete with Cr (VI) for adsorption sites (*Frank et al., 2019*). By contrast, Cr(III) species can be effectively scavenged onto Fe(III) (oxyhydr)oxides (*Frei et al., 2013*), clay minerals and sand (*Richard and Bourg, 1991*) as well as biogenic particles (*Semeniuk et al., 2016*); however, Cr isotope fractionation during scavenging of Cr(III) onto particles has not been reported.

Acid leaching experiments have shown that dissolution of chromites (Cr_2O_3) does not induce measurable Cr isotope fractionation between solid and dissolved pools of Cr(III) (*Crowe et al., 2013*). In contrast, dissolution promoted by strong organic ligands has been shown to result in variable $\delta^{53}Cr$ values of dissolved Cr(III) ($\delta^{53}Cr_{Cr(III)}$ = −0.27 to 1.23‰, *Saad et al., 2017*); further investigations on the role of ligands in the Cr isotope biogeochemistry would be recommended.

1.3 Thesis outline

As stated above, the overarching aim of this thesis is to utilise stable Fe and Cr isotopes to better understand sources and internal cycling of Fe and Cr in the North Atlantic Ocean.

In support of this, **Chapter 2** investigates Fe isotope behavior in hydrothermal vent fluids and near-field plumes at the Beebe and Von Damm vent fields on the mid-Cayman ultraslow spreading ridge. Samples were previously collected from RRS *James Cook* cruise JC82 (February 2012); results on size-fractionated Fe concentrations at these two sites have been published by *Lough et al. (2019a)* and *Lough et al. (2019b)*. This chapter is in preparation for journal *Geochimica et Cosmochimica Acta* for publication.

Chapter 3 presents dissolved Fe and Cr isotope data and examines the coupled Fe and Cr cycling in hydrothermal plumes and seawater above the TAG and Rainbow hydrothermal vents on the Mid-Atlantic Ridge. These samples were collected as part of GEOTRACES GA13 cruise on board RRS *James Cook* (JC156; December 2017 - February 2018). Alastair Lough, David González-Santana and Joesph Resing contribute to the measurements of dissolved Fe, Fe(II) and Mn concentrations respectively; Travis Mellet conducted Fe incubation experiments. Results from this chapter will be submitted to *Earth and Planetary Science Letters*.

Chapter 4 explores the Cr and Cr isotope cycling in subsurface and deeper seawater in the sub-tropical North Atlantic. This chapter utilises samples that were collected from GEOTRACES process

study GApr04 (JC150; June - August 2017); Korinna Kunde provides analytical results on Fe concentrations. This work is intended for submission to *Marine Chemistry*.

Finally, the key conclusions of this work and scope for future work are summarised in **Chapter 5**.

Chapter 2 Behaviour of iron isotopes in hydrothermal systems: Beebe and Von Damm vent fields on the Mid-Cayman ultraslow-spreading ridge

2.1 Introduction

Iron (Fe) plays a key role in the oceanic carbon cycle because it regulates primary productivity (*Boyd et al., 2007*). Some parts of the world's ocean have very low levels of Fe, yet high levels of other major nutrients (nitrate, phosphate and silicate), which means that the operation of the carbon pump is highly inefficient and sequestration of atmospheric CO_2 is restricted (e.g. *Watson et al., 2000*). Determining and quantifying the main sources of Fe to the ocean is therefore critical. However, the relative importance of different sources of Fe to the oceans is not well understood, flux estimates from atmospheric dust, oceanic sediments and hydrothermal vents vary by orders of magnitude (*Conway and John, 2014*).

Instrumental and methodological developments mean that it is now possible to accurately determine the stable isotope ratios of dissolved Fe (δ^{56}dFe) in seawater (*John and Adkins, 2010; Lacan et al., 2010*), which facilitates 'fingerprinting' of Fe from different sources. The δ^{56}Fe signature of atmospheric aerosols is ~0‰ (*Waeles et al., 2007*), although the δ^{56}Fe value of Fe that dissolves from dust may be higher (~+0.68‰, *Conway and John, 2014*). Sedimentary Fe produced by dissimilatory Fe reduction carries a negative δ^{56}Fe signature (−3.4 to −1.8‰, *Homoky et al., 2009; Severmann et al., 2010; John et al., 2012*), whereas sedimentary Fe produced by non-reductive dissolution processes has a higher δ^{56}Fe value, ~0.22 ± 0.18‰ (*Homoky et al., 2013*). The δ^{56}Fe value of hydrothermal vent fluids is also distinct, ~−0.67 to −0.12‰ (*Sharma et al., 2001; Beard et al., 2003; Severmann et al., 2004; Rouxel et al., 2008; Bennett et al., 2009; Klar et al., 2017; Nasemann et al., 2018*), raising the possibility that Fe isotopes could be used to provide new information that would help to square the oceanic cycle of Fe.

It is usually assumed that hydrothermal activity is not a major source of Fe because of precipitation of Fe-sulfides and Fe-(oxyhydr)oxides as Fe-rich high temperature hydrothermal vent fluids mix with seawater (*German et al., 1991*). However, recent studies have shown that a substantial portion of hydrothermal Fe may remain in the dissolved (<0.2 µm) phase (e.g. *Bennett et al., 2008; Hawkes et al., 2013; Kleint et al., 2016*), and this Fe may be transported for thousands of kilometres away from the mid-ocean ridge (*Resing et al., 2015*). In support of this, modelling studies have shown improved ability to reproduce Fe distributions when hydrothermal Fe sources were included

(*Tagliabue et al., 2010*). However, these models did not consider the behaviour of Fe in the hydrothermal plume, or variations in Fe fluxes from different vent sites (*Tagliabue and Resing, 2017*). Extending the models to incorporate these parameters, as well as increasing observations of Fe concentrations and Fe isotope distributions, particularly for hydrothermal systems, is critical for providing reliable predictions of future changes in the distribution of Fe and other micronutrients.

Hydrothermal plumes are created as vent fluids mix with seawater, and steep gradients in pH and Eh lead to precipitation of metals as sulfides and oxides (*Mottl and McConachy, 1990; Rudnicki and Elderfield, 1993*). Process studies at the East Scotia Ridge and the Vanuatu back-arc (*Klar et al., 2017; Lough et al., 2017; Nasemann et al., 2018*) indicated that significant changes in δ^{56}dFe occurred during plume rise and dispersal. The δ^{56}Fe value of hydrothermal Fe increased from −0.29‰ in the hydrothermal fluid to 0.07 to 0.49‰ as the vent fluids started to mix with seawater (*Klar et al., 2017*), presumably because of the formation of Fe-sulfides that are preferentially enriched in light Fe isotopes (*Butler et al., 2005*). In the later stages of plume mixing, the δ^{56}Fe value of dissolved Fe was observed to decrease, reaching values of as low as −2.5‰ (*Lough et al., 2017*), as a result of partial Fe(II)-Fe(III) oxidation and precipitation of the Fe(III) that forms, which leaves the remaining dissolved Fe enriched in light Fe isotopes (*Welch et al., 2003*). This remaining dFe may be stabilised in the form of colloids and organic complexes, contributing to the dissolved Fe budget of the wider deep ocean (*Klar et al., 2017*).

The aim of this study was to determine the behavior of iron isotopes in two hydrothermal systems, the Beebe vent field (BVF) and the Von Damm vent field (VDVF), located along the ultraslow Mid-Cayman spreading ridge in the Caribbean Sea. This fills an important gap in knowledge, because ultraslow-spreading centres are under-sampled globally, and models of hydrothermal Fe inputs based on ridge spreading rates have typically assumed that vents located along ultraslow-spreading ridges represent an insignificant source of Fe (*Tagliabue et al., 2010; Resing et al., 2015*).

2.2 Sampling sites

The Mid-Cayman spreading centre is an ultraslow-spreading ridge (full spreading rate <20 mm/yr) bisecting the Cayman Trough in the Caribbean Sea (Figure 2.1), and it is isolated from other parts of the global ridge system (*Connelly et al., 2012; German et al., 2010*).

The Beebe hydrothermal site is located at 18°32.785’N 81°43.080’W and in a water depth of 4960 m depth on the axis of the Mid-Cayman spreading ridge. It is the deepest hydrothermal vent field discovered to date. Hydrothermal fluids circulate through mafic and ultramafic lithologies and the vent field consists of at least six discrete sulfide mounds, three of which host active sites of fluid venting (Beebe Woods, Beebe 125 and Deepest Vents; *Webber et al., 2015*). The temperature of

the vent fluids is as high as 401°C, the pH of the vent fluids is ~3 (*Connelly et al., 2012*). The Beebe vent field is also referred to as the 'Piccard' vent field in the literature; here the name 'Beebe' is used as this is the name listed in the InterRidge database after venting was visually confirmed at the seafloor (*Connelly et al., 2012*).

The Von Damm vent field is located at 18°22.605'N 81°47.875'W in a water depth of 2300 m, on the upper slopes of an oceanic core complex, 13 km west of the spreading axis and ~20 km away from Beebe (Figure 2.1). Tectonic exposure of lower crustal and upper mantle rocks gives rise to a heterogeneous basement (*Hodgkinson et al., 2015*). Hydrothermal fluids have been collected from a series of talc chimneys, called Main Spire, Hotter than Hole, X15 and Chimlets. The Von Damm vent field emits particle-poor fluids, of lower temperature (up to 215°C) and intermediate pH (6-7), and hydrothermal precipitates mainly comprise magnesium silicate minerals (*Hodgkinson et al., 2015*). The vent fluids at Von Damm are highly enriched in dissolved H_2, CH_4, and low-molecular weight hydrocarbons compared to seawater, reflecting the influence of active serpentinization within the system (*McDermott et al., 2015*).

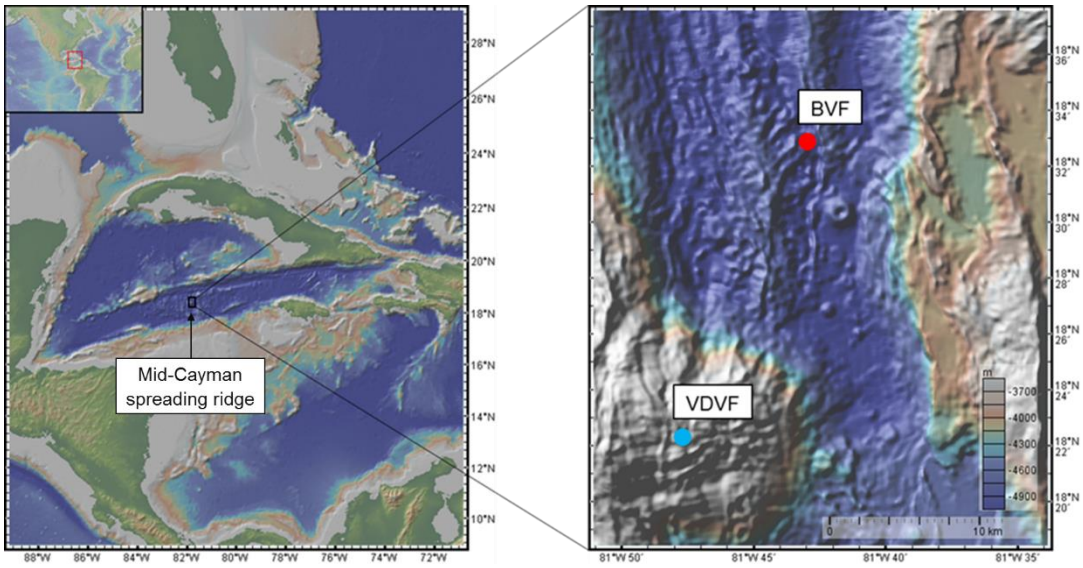

Figure 2-1 Location of the Beebe and Von Damm vent fields on the Mid-Cayman spreading ridge. Map courtesy of http://www.geomapapp.org

Both vent sites are bathed in water that has a temperature of 3.98°C, a salinity of 34.988, and an O_2 concentration of ~220 µM (*Connelly et al., 2012*), similar to North Atlantic Deep Water (NADW). This water mass likely enters the Caribbean via the Oriente Fracture Zone from the Windward Passage to the southwest (*Johns et al., 2002*).

2.3 Methods

2.3.1 Sample collection

Hydrothermal vent fluids, and fluids from the hydrothermal plume, were sampled during RRS *James Cook* cruise JC82 in February 2013. Gas tight samplers were employed to collect vent fluid samples from different chimneys, and temperatures were measured separately within the orifice using a probe deployed by the remotely operated vehicle (ROV) *Isis*. The vent fluid samples were then transferred into acid-cleaned polyethylene (PE) vials and were acidified on board to 0.015 M with ultra-pure nitric acid (Romil), for analysis back in the laboratory. Any precipitates that formed in the gas-tight samplers were re-dissolved and accounted for in the final element concentrations.

Hydrothermal plumes were detected using a Seabird 911 plus conductivity, temperature and depth (CTD) profiler system together with a light scattering sensor (LSS) and an Eh electrode. The buoyant part of the hydrothermal plumes was identified by positive LSS and temperature anomalies and a negative Eh anomaly.

Water samples from the buoyant plume at Beebe were collected using 10 L Ocean Test Equipment (OTE) water sampling bottles mounted on a titanium rosette deployed from the ship. At Von Damm, plume samples were collected 1-23 m above the seafloor using 1.2 L OTE bottles attached to the ROV *Isis*. Both sets of OTE bottles were modified for trace metal sampling and were pre-cleaned. Upon retrieval of the OTE bottles, ~500 mL of unfiltered seawater was collected for analysis of total dissolvable (TD) iron and manganese (Mn). The rest of the seawater sample was then filtered through a polycarbonate membrane filter (0.2 µm, Whatman) under gentle pressure, for collection of dissolved Fe and Mn. The dissolved fraction refers to <0.2 µm and the total dissolvable fraction (combined dissolved and labile particulate fraction) refers to unfiltered seawater. Both sets of samples were stored in low density polyethylene bottles (LDPE) that had been thoroughly acid-cleaned, and were acidified to pH <2 with ultra-pure nitric acid (Romil). All sample bottles were bagged and shipped back to the laboratory for further analysis.

2.3.2 Fe isotope analysis

The iron isotope compositions of hydrothermal vent fluids and plume samples were determined using a double spike technique, adapted from *Lacan et al. (2010)*. All acids used for chemical processing were thermally distilled. Milli-Q (MQ) water was used for diluting and for cleaning. LDPE bottles and Perfluoroalkoxy (PFA) vials were thoroughly cleaned for trace metal purposes. Samples were handled under laminar flow hoods, set within Class 100 clean laboratories at the University of Southampton.

Hydrothermal plume samples (dissolved and total dissolvable phases) were pre-concentrated using NTA Superflow resin. Columns were made with PFA tubing and a PE frit, and loaded with ~1 mL of clean NTA resin. The sample pH was adjusted to between 1.7-1.8 and 10 µM UpA-grade hydrogen peroxide (H_2O_2, Sigma Aldrich) was added to the sample ~30 min prior to starting the pre-concentration procedure. Between uses and before loading a sample, the resin was cleaned with 75 mL 1.5 M HCl and 80 mL MQ. The sample was passed over the resin by gravity flow, and the resin was then rinsed with MQ water to remove residual salts. The Fe fraction was eluted with 10 mL of 1.5 M HCl, collected in an acid cleaned PFA vial (Savillex), and subsequently evaporated on a hotplate and reconstituted in 5M HCl (with 0.001% H_2O_2) for further analysis.

Fe can be efficiently separated from cations such as Cr and Ni that also bind to NTA resin, by conversion to $FeCl_4^-$ in strong HCl and purification by anion exchange. Approximately 200 µL of cleaned AG-MP1 resin (BioRad) was loaded in handmade micro columns (PE material, ~8 cm length and ~3 mm diameter). Each column was pre-cleaned by addition of 1 mL of 2 M HNO_3 and conditioned by addition of 0.2 mL of 5 M HCl (with 0.001% H_2O_2), before loading the sample in 5 M HCl (with 0.001% H_2O_2). Matrix elements were eluted with 1 mL of 5 M HCl (with 0.001% H_2O_2). Then the Fe fraction was eluted with 1 mL of 1 M HCl into a clean Savillex vial, and was dried down gently and re-dissolved in 0.3 M HNO_3.

No pre-concentration was needed for the vent fluids, as they have higher Fe concentrations. Prior to purification on the anion exchange column, the vent fluid samples were oxidised by reflux with concentrated HNO_3 and H_2O_2.

The isotopic composition of the Fe was determined by multicollector inductively coupled plasma mass spectrometry (MC-ICP-MS; Thermo Fisher Neptune Plus). Instrumental mass bias was corrected using a ^{57}Fe-^{58}Fe double spike, which was added in equi-molar concentration to the sample before chemical processing. The isotope values are reported in delta notation relative to the Fe isotope reference material IRMM-14 and expressed as:

$$\delta^{56}Fe\ (‰) = [(^{56}Fe/^{54}Fe)_{sample}/(^{56}Fe/^{54}Fe)_{IRMM\text{-}14} - 1] \times 1000 \quad (2\text{-}1)$$

Samples with ~100 ng/mL Fe were introduced to the plasma using an Apex-Q desolvator (ESI) and signals from ^{54}Fe, ^{56}Fe, ^{57}Fe, ^{58}Fe, ^{53}Cr, ^{60}Ni were quantified. Analysis by MC-ICP-MS was carried out in high-resolution mode, and each sample measurement consisted of 50 individual measurements. The instrument was carefully tuned to give sufficient mass resolution (>8000), before running a sequence that consisted of analysis of the reference material (IRMM), the internal Fe standard (ETH), Sample 1, Sample 2, and so on. The wash time was 70 s before analysis of each sample/standard and 420 s before the analysis of blanks. The mean beam intensity of a blank

solution that was analysed before and after each sample/standard was subtracted. Mass bias was corrected by iteratively deconvolving the spike-sample mix based on data reduction methodology. Analysis of the ETH iron isotope standard gave $\delta^{56}Fe = 0.51 \pm 0.09‰$ (2SD, n=45), in agreement with the consensus value (0.52 ± 0.08‰; *Lacan et al., 2010*).

The overall procedural (preconcentration and purification) Fe blank was 1.54 ± 0.74 ng (n=2). The accuracy of the method was validated through the analysis of trace metal free seawater doped with the hematite (HEM) Fe isotope standard, yielding an average $\delta^{56}Fe$ value of 0.22 ± 0.10‰ (2SD, n=5), consistent with previously published HEM values ($\delta^{56}Fe = 0.24 \pm 0.05‰$; *Klar et al., 2017*).

2.3.3 Ancillary analyses

The vent fluids were diluted 100-2500 fold with 0.3 M HNO_3 and concentrations of major and minor cations were determined by inductively coupled plasma atomic adsorption spectroscopy (ICP-AES; iCAP 6000, Thermo Scientific) and ICP-MS (X-series, Thermo Scientific). Chloride concentrations were measured by ion chromatography (Dionex), and sulfide was measured immediately after recovery of the gas tight sampler by iodometric titration.

The Fe and Mn concentrations in the hydrothermal plume samples were measured by ICP-MS (Element XR, Thermo Scientific) after pre-concentration on a chelating resin using an offline extraction system, as discussed in *Lough et al. (2019a)* and *Lough et al. (2019b)*. The initial determinations of dFe and TDFe were used to estimate the sample volume required for ~100 ng of Fe for the isotopic analysis. The reported Fe concentration data are from the MC-ICP-MS measurements; the MC-ICP-MS data were within 20% (with two exceptions) of the concentration measured by ICP-MS.

2.4 Results

2.4.1 Hydrothermal vent fluids

The chemical compositions of vent fluid samples analysed for $\delta^{56}Fe$ are shown in Table 2.1, and the compositions of all vent fluid samples collected on cruise JC82 are given in the Apppendix (Table A1). At Beebe, the vent fluids had relatively high temperatures (393 to 401 °C) and low pH (2.9 to 3.1) compared to vent fluids from Von Damm (temperatures up to 215 °C and pH = 6-7).

The sampled vent fluid compositions can be assumed to reflect two-component mixing of a hydrothermal 'end-member' fluid that contains no magnesium (Mg) with bottom seawater. Thus samples analysed for $\delta^{56}Fe$ from Beebe consisted of >90% hydrothermal fluid, whereas the sample

from Von Damm with lowest Mg consisted of ~70% hydrothermal fluid. Vent fluid samples with low Mg (as low as 2.5 mM) have nevertheless been collected from Von Damm during other sampling campaigns (*McDermott, 2015*).

Based on the extended vent fluid data (Table A1), and by extrapolation to zero-Mg, the hydrothermal end-member Mn and Fe concentrations at the Beebe vent field were, respectively, 570-595 µM and 5840-8390 µM, similar to end-member fluid compositions (567-571 µM Mn and 6660-12800 µM Fe) reported by *McDermott et al. (2018)* for the same study area. The calculated end-member H_2S concentrations (5.5-7 mM) were lower than measured previously (~12 mM; *McDermott et al., 2018*).

Table 2-1 Composition of hydrothermal vent fluids from Beebe and Von Damm. NA = not available; * calculated from all available data, which are given in the SI, except $\delta^{56}Fe$ which is given as the value measured in the sample with lowest Mg.

Sample	Vent site	Temp °C	pH	Mg mM	H_2S mM	Mn µM	Fe µM	Fe/ H_2S	$\delta^{56}Fe$ ‰
Beebe vent field									
FLU13	Beebe 125	401	3.1	2.6	NA	561	6168	NA	-0.28
FLU25	Beebe 125	401	3.1	5.5	3.2	507	3284	1.0	-0.06
FLU26	Beebe 125	401	3.0	3.0	3.2	516	5466	1.7	-0.08
Beebe 125 end-member*			***3.0***	***0***	***5.5***	***570***	***5843***	***1.1***	***-0.28***
FLU16	Deepest Vents	393	2.9	5.3	5.1	532	5744	1.1	-0.10
Deepest Vents end-member*			***2.9***	***0***	***7***	***595***	***8387***	***1.2***	***-0.10***
Beebe end-member (McDermott et al. 2018)				*0*	*12*	*567-571*	*6660-12800*	*0.6-1.0*	
Von Damm vent field									
FLU1	Main Spire	215	6.0	14.5	0.95	8	18	0.02	0.08
Main Spire Endmember*			***~5.6***	***0***	***~1.7***	***~11***	***~22***	***~0.01***	***~0.08***
FLU7	Hotter than Hole	133	6.1	25.9	0.45	12	292	0.6	-0.80
FLU8	Hotter than Hole	133	6.2	29.1	0.99	14	334	0.3	-0.36
FLU12	Chimlet 2	107	7.0	40.0	NA	10	145	NA	-0.90
Hotter than Hole/ Chimlet 2 Endmember			***~5.6***	***0***	***~1.5***	***~25***	***~541***	***~0.4***	***NA***
FLU10	X15 marker	111	6.4	28.8	0.80	12	750	0.9	-0.58
East Summit end-member (McDermott 2015)		*226*	*5.6*	*0*	*3.2*	*10*	*21*	*0.01*	

Using the same methodology, the end-member composition of Main Spire samples at the Von Damm vent field had Mn = ~11 µM and Fe = ~22 µM, within the range (8.9-11.3 µM for Mn and 21-46 µM for Fe) in low Mg (2.5-14.8 mM) fluids reported by *McDermott (2015)*. As no samples with low Mg concentrations were collected at Hotter than Hole and Chimlet 2, only minimum values for the end-member contents for non-conservative elements could be estimated; for Mn this was ~25 µM and for Fe this was ~541 µM. The estimated end-member H_2S concentrations were ~1.7 mM for Main Spire and ~1.5 mM for Hotter than Hole and Chimlet 2, slightly lower than values reported for low Mg vent fluids from East Summit (3.3 mM; *McDermott, 2015*).

At the Beebe vent field, the sample with lowest Mg had a δ^{56}Fe value of −0.28‰, within the range of high-temperature fluids from basalt-hosted hydrothermal fields on the Mid-Atlantic Ridge (−0.5 to −0.2‰; *Bennett et al., 2009; Severmann et al. 2004*). At the Von Damm vent field, the δ^{56}Fe value of the fluid sample with lowest Mg is slightly higher, 0.08‰ (Appendix, Figure A2). These two samples show Mn and Fe concentrations closest to the calculated end-member values, their Fe isotope compositions are considered to be most representative of the end-member compositions at the two vent fields.

2.4.2 Dissolved and total dissolvable Fe concentrations in the hydrothermal plumes

The dFe and TDFe concentrations in buoyant plume samples from the Beebe and Von Damm vent fields are plotted against vent fluid dilution factor in Figure 2.2a. The vent fluid (VF) dilution factor is given by $([Mn]_{VF} - [Mn]_{SW})/([Mn]_{sample} - [Mn]_{SW})$, where [Mn] represents Mn concentration and SW represents background seawater. $[Mn]_{VF}$ was 570-595 µM for Beebe and 11-25 µM for Von Damm (Table 2.1), and $[Mn]_{SW}$ was 0.1 nM (*Lough et al., 2019a*). Mn shows near-conservative behaviour during mixing of vent fluids and seawater over timescales of weeks, and therefore serves as a tracer of hydrothermal plume dispersal.

TDFe and dFe concentrations decreased with increasing vent fluid dilution factor at both vent fields, as the hydrothermal fluids mix with background seawater with low Fe (Figure 2.2a). At Beebe, concentrations of TDFe were ~31-74% (average 54 ± 15%) lower than predicted for conservative mixing between the vent fluid and seawater, indicating that Fe was removed from the plume, presumably by particle fall-out. However, at Von Damm, concentrations of TDFe in the plume were generally within the range predicted by conservative mixing, suggesting that particle fall-out at this site was minimal.

Concentrations of dFe at Beebe and Von Damm, respectively, ranged from 16.1 to 86.5 nM and 21.0 to 62.6 nM. These values are significantly higher than background seawater (~0.8 nM in North Atlantic Deep Water; *Lough et al., 2019a*). In general, the ratio of dFe/TDFe increased as the plume

becomes more dilute, varying from < ~10% in the proximal plume to up to ~60% at higher dilution factor. Thus, a higher proportion of Fe is present in the particulate fraction close to the vent source.

2.4.3 Isotopic composition of dissolved and total dissolvable Fe in the hydrothermal plumes

The δ^{56}Fe values of dFe showed notable changes as the buoyant plume becomes more dilute (Figure 2.2b). At the Beebe vent field, samples from the least dilute part of the plume had very low δ^{56}dFe values (as low as −4.08‰), indicating enrichment of light Fe isotopes relative to the end-member vent fluid. At the Von Damm vent field, δ^{56}dFe values were as low as −2.49‰. These values are lower than those reported for plume samples recovered from the Mid-Atlantic Ridge, East Scotia Ridge, East Pacific Rise, and the Vanuatu back-arc basin (−2.39 to −0.13‰: *Conway and John et al., 2014; Klar et al., 2017; Lough et al., 2017; Fitzsimmons et al., 2017; Nasemann et al., 2018*). As the plumes become more dilute, the δ^{56}dFe values increased, samples with the lowest Mn concentrations (9 nM and 2 nM) had δ^{56}dFe values of 0.29‰ and 0.22‰ at Beebe and Von Damm, respectively.

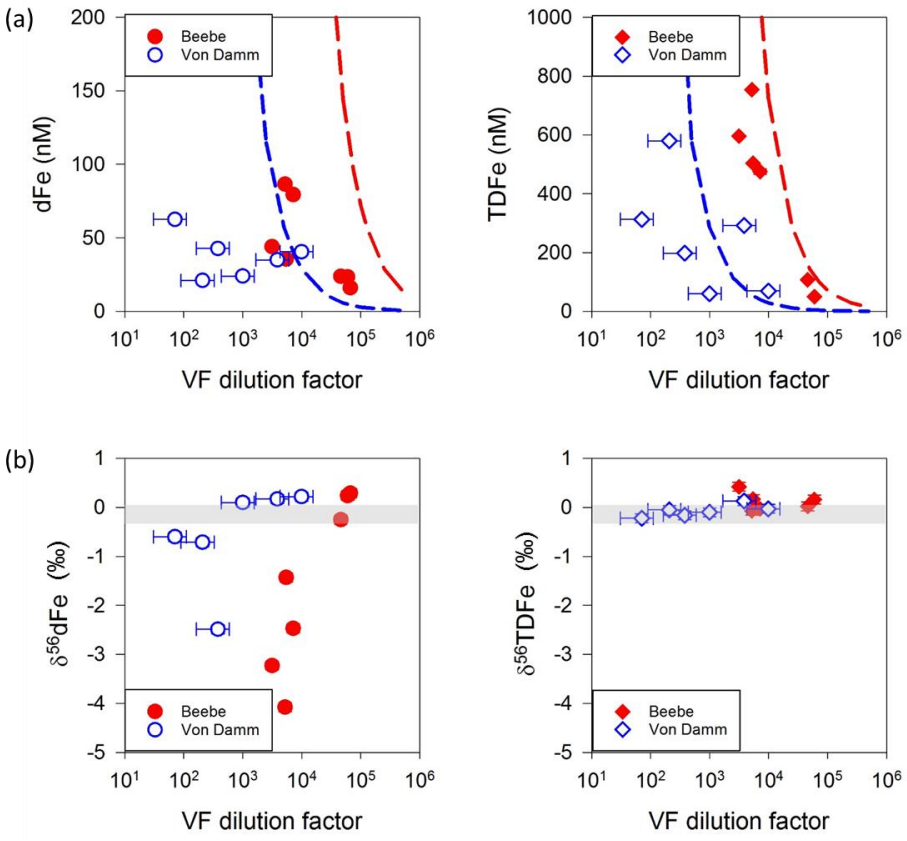

Figure 2-2 (a) Concentrations of dissolved Fe (dFe) and total dissolvable Fe (TDFe), relative to vent fluid (VF) dilution factor at Beebe and Von Damm vent fields. The dashed lines show conservative mixing of the end-member fluid with background seawater, for Beebe (red) and Von Damm (blue).

(b) Fe isotope compositions of dFe and TDFe (δ^{56}dFe and δ^{56}TDFe), relative to vent fluid dilution factor at Beebe and Von Damm. The grey band represents δ^{56}Fe of the lowest Mg vent fluids from both sites (see Table 2.1). Errors bars for dFe are smaller than the markers; error bars for δ^{56}Fe represent external reproducibility (± 0.09‰, 2SD) based on the long-term precision of the iron isotope standard (ETH). All Fe data are available and can be found in Appendix (Table A3).

The δ^{56}Fe of TDFe showed less variation during plume mixing, with values ranging from −0.22 to 0.42‰ at both sites (Figure 2.2b). The average δ^{56}TDFe value in the Beebe plume (0.11‰) was higher than that in the Von Damm plume (−0.07‰), and higher than the δ^{56}Fe value of the low-Mg Beebe vent fluid (−0.28‰). At Von Damm, the δ^{56}Fe of the vent fluid with lowest Mg (0.08‰) was intermediate relative to δ^{56}TDFe values (−0.22 to 0.13‰) measured in the plume.

The concentration of labile particulate Fe (LPFe), which is operationally defined as >0.2 µm fraction, is derived from the differences in concentrations between TDFe and dFe. By knowing the relative proportions of dissolved and labile particulate Fe (respectively X_{dFe} and X_{pFe}), the Fe isotopic composition of LPFe can be estimated by mass balance (*Chever et al., 2015*):

$$\delta^{56}\mathrm{TDFe} = \mathrm{X}_{dFe} \cdot \delta^{56}\mathrm{dFe} + \mathrm{X}_{LPFe} \cdot \delta^{56}\mathrm{LPFe} \qquad (2\text{-}2)$$

δ^{56}Fe values for this fraction ranged from 0.09 to 0.71‰ in the Beebe plume (Table A3) and were highest in the proximal plume. At Von Damm, δ^{56}Fe values of this fraction ranged from −0.38 to 0.48‰ (Table A3) but there was no obvious shift in δ^{56}Fe values as the plume becomes more dilute.

2.4.4 Incubation experiment

To investigate how concentrations of dFe and δ^{56}dFe values may evolve during the delay between sampling and filtering, an on-board incubation experiment was carried out. One 10 L water sample (sample JC82-CTD11-N4) from the buoyant plume from the Beebe vent field was stored in its OTE sampling bottle for between 6 to 16 h before it was filtered. Over this time period, the concentration of dMn stayed the same (22 ± 0.5 nmol/kg; *Lough et al., 2019a*), but the concentration of dissolved Fe decreased from 28.9 nM to 7.4 nM (Figure 2.4a). Over the same time interval, the δ^{56}Fe value of dFe increased from −0.37‰ to 0.51‰. These data indicate that isotopically light Fe was being removed from the dissolved fraction over time.

2.5 Discussion

2.5.1 Fe isotope composition of the hydrothermal vent fluids

The $\delta^{56}Fe$ values of the low-Mg Beebe vent fluids ranged from −0.28 to −0.10‰, within the range of low-Mg hydrothermal fluids from ultramafic- and basalt-hosted hydrothermal systems measured to date (−0.67 to −0.12‰; Table A4). These values are systematically lower than unaltered mid-ocean ridge basalt ($\delta^{56}Fe = 0.1 \pm 0.01$‰; *Teng et al., 2013*), which has been attributed to preferential leaching of light Fe isotopes during alteration (*Rouxel et al., 2008*). Other processes, such as secondary mineral formation in the reaction zone and Fe-sulfide precipitation in the shallow subseafloor, may also cause fractionation of Fe isotopes (*Rouxel et al., 2003; Rouxel et al., 2004*), but phase separation and variations in host rock lithology are not thought to be a control on the Fe isotope composition of vent fluids (*Beard et al., 2003; Bennett et al., 2009*).

At the Von Damm vent field, the $\delta^{56}Fe$ values of vent fluids range from −0.90 to 0.08‰, and the values decrease with increasing Mg (Figure A2). The sample with the lowest Mg (14.5 mM) is isotopically heavy ($\delta^{56}Fe = 0.08$‰) relative to fluids from other hydrothermal sites that have a low Mg content (Table A4). The hydrothermal fluids likely underwent mixing with seawater circulating in the shallow subsurface prior to venting (*McDermott, 2015; Hodgkinson et al., 2015*). This can be expected to result in precipitation of part of the Fe in the hydrothermal fluids as Fe-sulfides that are preferentially enriched in light Fe isotopes (*Butler et al., 2005*), leaving the residual Fe isotopically heavier. The combined effects of subsurface conductive cooling of hydrothermal fluids and mixing with seawater, leading to precipitation of sulfides with low $\delta^{56}Fe$ value of −2 to −1‰, have previously been documented at the Lucky Strike vent field on the Mid-Atlantic Ridge (*Rouxel et al., 2004*).

2.5.2 Fractionation of Fe isotopes in the buoyant plume

The $\delta^{56}Fe$ values of dissolved Fe sampled in the near-field plumes are lower than that of Fe in the hydrothermal fluid, and evolve towards higher $\delta^{56}Fe$ with increasing plume dilution. This strongly suggests that the $\delta^{56}Fe$ of hydrothermal iron has been modified by oxidation of Fe(II) to Fe(III) as the vent fluids mix with oxygenated seawater. Experimental and theoretical studies have shown that oxidation of $Fe(II)_{aq}$ enriches heavy Fe isotopes in $Fe(III)_{aq}$, and the difference between $\delta^{56}Fe(III)_{aq}$ and $\delta^{56}Fe(II)_{aq}$ can be up to 3.56‰ (*Welch et al., 2003; Anbar et al., 2005*). $Fe(III)_{aq}$ is not stable in seawater and forms colloidal-sized (opernationally defined as between 0.02 and 0.2 µm diameter) Fe-(oxyhydr)oxides (FeOOH), which subsequently aggregate and coagulate into larger particles (>0.2 µm) (*Lough et al., 2019a*). Under equilibrium conditions, the fractionation between

$Fe(II)_{aq}$ and FeOOH is very similar to that between $Fe(II)_{aq}$ and $Fe(III)_{aq}$, meaning that there is no or very limited isotope fractionation between $Fe(III)_{aq}$ and FeOOH (*Wu et al., 2011*). Therefore, the overall effect of oxidation of Fe(II) to Fe(III) and the formation of Fe-(oxyhydr)oxides is the preferential removal of the heavier Fe isotopes from the dissolved Fe pool.

The $\delta^{56}Fe$ value of dissolved Fe in the buoyant plume is a function of the proportion (*F*) of Fe remaining as Fe(II) and the proportion (*X*) of Fe(III) remaining in the dissolved (colloidal) fraction, and can be modelled as a Rayleigh fractionation process (*Klar et al., 2017; Lough et al., 2017; Nasemann et al., 2018*):

$$\delta^{56}\mathrm{Fe(II)} = (\delta^{56}\mathrm{Fe(II)}_0 + 1000) \cdot F^{\alpha-1} - 1000 \quad (2\text{-}3)$$

$$\delta^{56}\mathrm{Fe(III)} = (\delta^{56}\mathrm{Fe(II)}_0 + 1000) \cdot \frac{1-F^{\alpha}}{1-F} - 1000 \quad (2\text{-}4)$$

where $\delta^{56}Fe(II)$ is the isotopic composition of the remaining Fe(II), $\delta^{56}Fe(II)_0$ is the initial isotopic composition of dissolved Fe(II) before oxidation starts, $\delta^{56}Fe(III)$ is the iron isotopic composition of the accumulated Fe(III) precipitate, and α is the fractionation factor between aqueous Fe(II) and precipitated Fe(III) ($\alpha_{Fe(III)\text{-}Fe(II)}$ ~1.0035 at temperature of 4°C; *Welch et al., 2003*). To correct for the effect of sulfide precipitation during the early stages of plume mixing (see Section 2.5.3), $\delta^{56}Fe(II)_0$ is taken to be 0.19‰ (precipitation of 54% on vent fluid Fe as Fe-sulfide) at Beebe and 0.08‰ (no precipitation of Fe-sulfide after venting) at Von Damm. Assuming that FeOOH precipitates at a constant rate, the δ^{56}dFe signal delivered to the plume is given by (*Klar et al., 2017*):

$$\delta^{56}\mathrm{dFe} = \frac{F\cdot\delta^{56}\mathrm{Fe(II)} + X\cdot(1-F)\cdot\delta^{56}\mathrm{Fe(III)}}{F + X\cdot(1-F)} \quad (2\text{-}5)$$

Based on the measured ratios of dFe/TDFe in samples collected during the earliest stages of plume mixing, the proportion of Fe(III) that precipitates should be ≥83% at Beebe and ≥78% at Von Damm. As Fe(II) must reside exclusively in the dissolved fraction then, similarly, the proportion of Fe(II) that is oxidised to Fe(III) must also be ≥78%. The results of this modelling exercise are shown in Figure 2.3a. The low $\delta^{56}Fe$ values of dFe (−4.08 to −0.60‰) in the near-field plumes are well described by the Rayleigh model: the lowest δ^{56}dFe value, −4.08‰ at Beebe, is consistent with oxidation of ~94% Fe(II) to Fe(III) followed by precipitation of ~89% Fe(III) as FeOOH, which is consistent with the measured concentrations of dFe and TDFe.

Fe-(oxyhydr)oxides have relatively small particle size and tend to remain in the plume once removed from the dissolved fraction (*Lough et al., 2019a*). In support of this, calculated $\delta^{56}Fe$ values of the labile particulate fraction (LPFe) are isotopically heavy (−0.13 to 0.71‰ in the near-field plumes) compared to Fe in the dissolved fraction. The calculated δ^{56}LPFe values are generally similar to or slightly lower than the $\delta^{56}Fe$ values of the accumulated Fe(III) precipitate predicted by

Rayleigh modelling (Figure 2.3a). As discussed in the next section, the slightly lower than predicted δ^{56}LPFe values, at least at Beebe, may be due to the presence of Fe-sulfides in the labile particulate fraction.

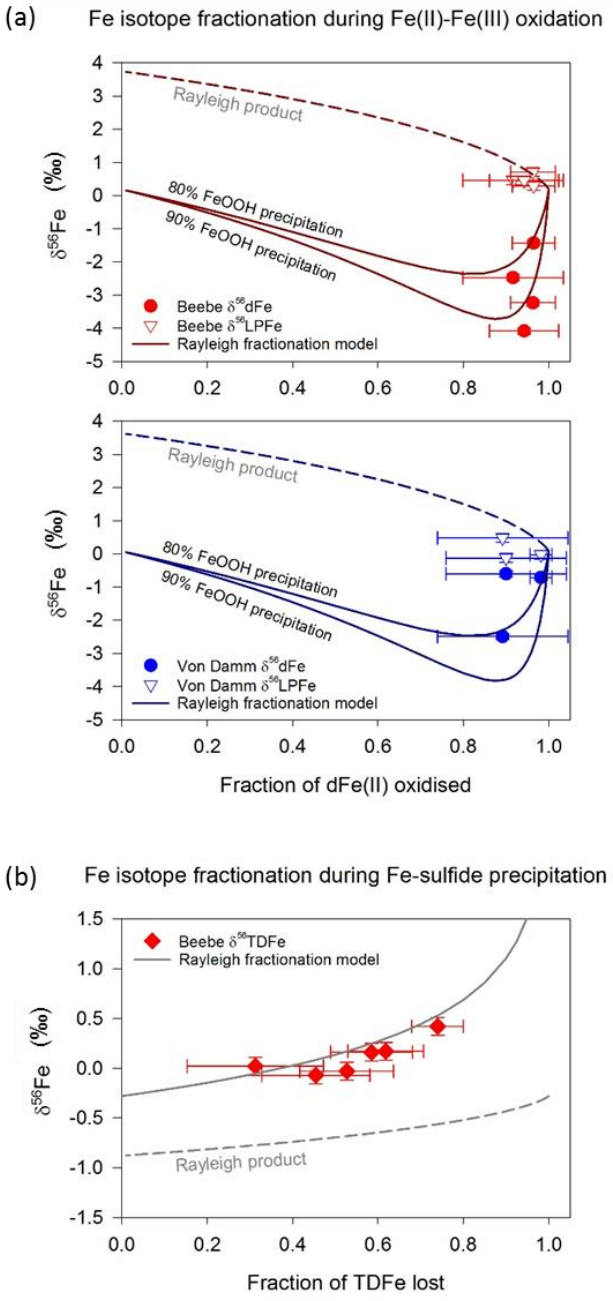

Figure 2-3 (a) δ^{56}Fe relative to the fraction of dFe(II) oxidised to Fe(III). The observed δ^{56}dFe values in the near-field buoyant plumes at Beebe and Von Damm are explained by a Rayleigh fractionation model with $\delta^{56}Fe(III) - \delta^{56}Fe(II)_{aq}$ = 3.5‰ (see text for details). The calculated δ^{56}Fe values of labile particulate Fe are generally consistent or slightly lower than predicted by the Rayleigh fractionation model. The horizontal error bars reflect the uncertainty in the proportion of dFe(II) in the dFe pool (0 to 100%). **(b)** δ^{56}Fe relative to the fraction of TDFe lost from the plume at Beebe. Solid line shows the evolution of δ^{56}TDFe predicted by Rayleigh fractionation modelling of sulfide precipitation (see text for details). The errors bars for δ^{56}Fe represent external reproducibility (± 0.09‰, 2SD) based on the long-term precision of the iron isotope standard (ETH). The horizontal error bars reflect the uncertainty in the composition of the end-member fluid.

As the buoyant plumes become more dilute (lower Mn concentration), δ^{56}Fe of dFe evolves to higher values (0.22 to 0.29‰). This can be partly explained by near-quantitative oxidation of Fe(II). In addition, exchange of Fe between particulate and dissolved fractions occurs during ascent of the plumes (*Lough et al., 2019a, 2019b*). It is likely that Fe-(oxyhydr)oxides, which have isotopically heavy δ^{56}Fe relative to $\delta^{56}Fe(II)_0$, are recycled back into the dissolved (presumably colloidal) Fe fraction through dissolution.

2.5.3 Evidence for Fe-sulfide precipitation in the buoyant plume

As discussed in Section 2.5.1, when hot Fe- and H_2S-rich vent fluids come into contact with cold seawater, Fe(II) may precipitate as Fe-sulfide (FeS and FeS_2). Precipitation of Fe-sulfide would leave the residual dissolved Fe enriched in the heavier Fe isotopes (*Butler et al., 2005*) and, based on analyses of buoyant plume particles, the estimated difference between the δ^{56}Fe value of the FeS particles and dissolved Fe ($\delta^{56}Fe_{FeS} - \delta^{56}Fe$) is −0.60‰ (*Bennett et al., 2009*). The δ^{56}Fe value of Fe remaining in the dissolved fraction can be estimated using a Rayleigh fractionation model:

$$\delta^{56}\mathrm{Fe} = (\delta^{56}\mathrm{Fe}_{\mathrm{VF}} + 1000) \cdot f^{\alpha-1} - 1000 \qquad (2\text{-}6)$$

where $\delta^{56}Fe_{VF}$ is the Fe isotope composition of the end-member vent fluid, α is the fractionation factor between FeS and Fe(II) (~0.9994; assuming $\alpha \approx e^{\delta^{56}\mathrm{Fe}_{\mathrm{FeS}} - \delta^{56}\mathrm{Fe}}$), and f is the proportion of Fe that remains in the plume, based on the ratios of measured to calculated TDFe concentrations.

While there is no evidence for sulfide formation in the buoyant plume at VDVF (*Lough et al., 2019b*), at Beebe, f has an average value of ~0.46 (Section 2.4.2). If all of the Fe lost from the plume during the initial stages of mixing was precipitated as FeS, and given that $\delta^{56}Fe_{VF}$ = −0.28‰, then the δ^{56}Fe value of dissolved Fe remaining in the plume would be ~0.19‰, far higher than the measured values in the early stages of plume mixing (−4.08 to −1.43‰). While this indicates that precipitation of Fe-(oxyhydr)oxides (that preferentially incorporate heavy Fe isotopes) is the principal control on δ^{56}dFe delivered to the buoyant plume (see Section 2.5.2), the δ^{56}Fe value of TDFe increases as the proportion of Fe predicted to have been lost from the plume increases (Figure 2.3b). This suggests that loss of Fe from the buoyant plume is primarily controlled by precipitation of Fe-sulfides that are relatively enriched in light Fe isotopes. Fe-sulfide particles are relatively dense compared to Fe-(oxyhydr)oxides and will settle out of the plume more quickly (*Lough et al., 2017*). Nevertheless, whilst fall-out of sulfides can explain the evolution of δ^{56}TDFe, the calculated δ^{56}Fe values of labile particulate Fe (0.09 to 0.71‰) are higher than the δ^{56}Fe value of the vent fluid Fe source, indicating that the labile particulate fraction is dominated by Fe-(oxyhydr)oxides.

Loss of Fe due to Fe-sulfide formation in the Beebe buoyant plume is also supported by the results of the incubation experiment. The concentration of dissolved Fe in the buoyant plume sample progressively decreased over time whereas the δ^{56}Fe value of the dFe increased (Figure 2.4a), consistent with preferential loss of light Fe isotopes from the dissolved fraction. As the half-life for Fe(II) oxidation at Beebe is short (0.28 h; *Lough et al., 2019a*), Fe(II) oxidation is essentially complete by the time the first sub-sample was collected 6 hours after the sample bottle was closed (see Section 2.4.4). This means that changes in δ^{56}dFe cannot be attributed to Fe(II) oxidation which, in any case, is expected to remove Fe that is preferentially enriched in heavy Fe isotopes, which would decrease (rather than increase) the δ^{56}Fe value of Fe that remains in the dissolved fraction (*Klar et al., 2017; Lough et al., 2017*).

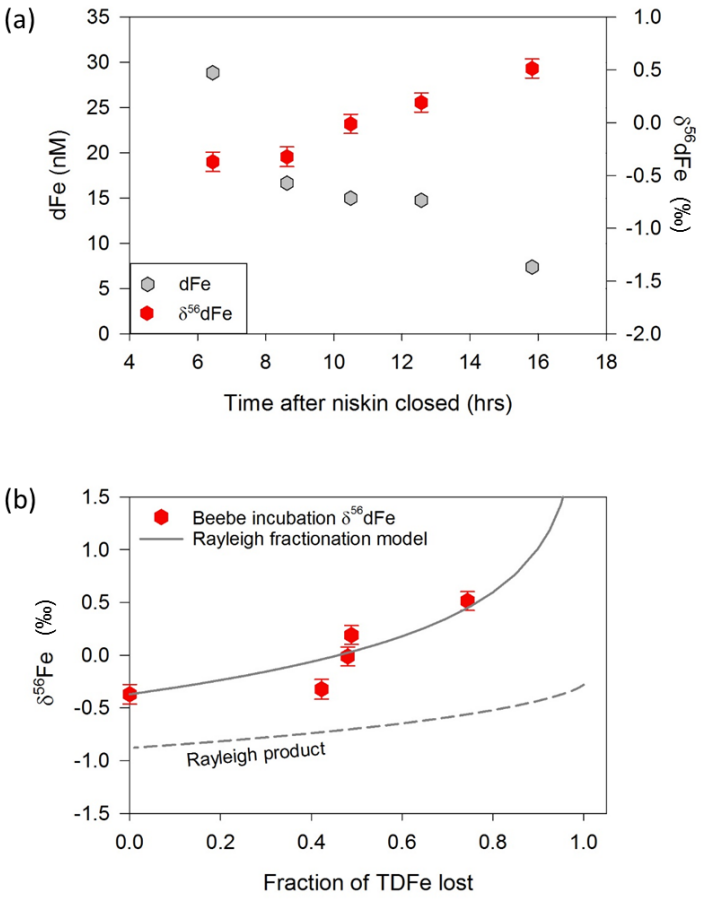

Figure 2-4 (a) Repeat sub-sampling of a niskin bottle (JC82-CTD11-N4) to show changes in dFe and δ^{56}dFe over time. The original sample was taken from the buoyant plume at Beebe. **(b)** Variation in δ^{56}dFe as a function of the proportion of dFe removed from solution over the course of the incubation experiment. Solid line shows results of a Rayleigh fractionation model for sulfide precipitation (see text for details).

Removal of Fe during the incubation experiment can be described in terms of Rayleigh fractionation (Equation 2-6). In this case, $\delta^{56}Fe_{VF}$ is rather represented by the Fe isotope composition of the first sub-sample. If removal of Fe occurs via precipitation of FeS then, as described above, α = ~0.9994, and the δ^{56}Fe value of Fe that remains in solution increases as the proportion of Fe that remains in solution decreases (Figure 2.4b). With the exception of the second sub-sample that was collected ~8 h after the sample bottle was closed, the incubation experiment data are consistent with loss of Fe via the precipitation of Fe-sulfides (Figure 2.4b). In support of this, SEM images of particles from the Beebe non-buoyant plume have revealed the presence of large FeS_2 particles (~10 µm) consisting of aggregates of smaller (<2 µm) particles (*Lough et al., 2019a*). Formation of FeS_2 nanoparticles (<0.2 µm) has also been observed in nascent plumes forming above high-temperature vents at the East Pacific Rise (*Yucel et al., 2011; Findlay et al., 2019*).

By contrast, a similar incubation experiment carried out on a buoyant plume sample collected from the E2 hydrothermal site on the East Scotia Ridge revealed that while dFe concentrations decreased over time between sampling and filtering, the δ^{56}Fe value of the dissolved Fe decreased, consistent with oxidation of Fe(II) and precipitation of the Fe(III)-(oxyhydr)oxides that form (*Lough et al., 2017*). It is important to note, however, that the oxidation half-life of Fe(II) is significantly longer at E2 (1.45 to 5.63 h; *Lough et al., 2017*) than it is at Beebe (~0.28 h), such that the number of oxidation half-lives between sampling and filtering of the sample from the E2 plume was significantly lower (1-2 half-lives) than the number of oxidation half-lives between sampling and filtering of the sample from the Beebe plume (>10 half-lives). This means that Fe(II) oxidation was continuing throughout the incubation at E2, but was essentially complete by the time the first sub-sample was taken at Beebe. Considered together, the results of the incubation experiments suggest that Fe-sulfide nanoparticles can persist during the early stages of plume mixing, and only coagulate and precipitate during the later stages of plume dispersal.

2.5.4 Controls on the δ^{56}Fe signature of dissolved Fe in hydrothermal plumes

Work done in this and other studies (*Conway and John, 2014; Fitzsimmons et al., 2017; Klar et al., 2017; Lough et al., 2017; Nasemann et al., 2018; Rouxel et al., 2018*) shows that the δ^{56}Fe signature of hydrothermal Fe is modified by the formation and precipitation of Fe-sulfides and Fe-(oxyhydr)oxides in hydrothermal plumes. The relative importance of these processes, and thus the Fe isotopic signature of hydrothermally-derived Fe that is delivered to the ocean interior, is likely influenced by both the vent fluid chemistry (including the δ^{56}Fe signature), and the chemistry of the seawater that mixes with the vent fluids when they are expelled at the seafloor (e.g. *Bennett et al., 2009; Rouxel et al., 2016; Millero et al., 1987*).

The range of measured δ^{56}dFe values in hydrothermal plumes published to date is compared to some of these parameters in Figure 2.5. To a first order, there is no obvious relationship between δ^{56}dFe values in hydrothermal plumes and the vent fluid Fe/H_2S ratio (Figure 2.5a), but if samples collected from the distal parts of plumes (15°S EPR and TAG) are excluded, together with the sample from Pele's Pit that represents mixing between seawater and a low temperature fluid with high Mg, then there is a general trend towards lower δ^{56}dFe values in the near-field hydrothermal plume with increasing Fe/H_2S. This would imply that the vent fluid Fe/H_2S ratio determines the proportion of hydrothermal Fe(II) 'left over' from precipitation of Fe-sulfides during the early stages of plume mixing that is subsequently oxidised and precipitates as Fe-(oxyhydr)oxides. Nifonea is an exception to this general trend, possibly due to sluggish Fe(II) oxidation due to complexation with organic ligands and/or the formation of Fe-(oxyhydr)oxide nanoparticles (*Nasemann et al., 2018*).

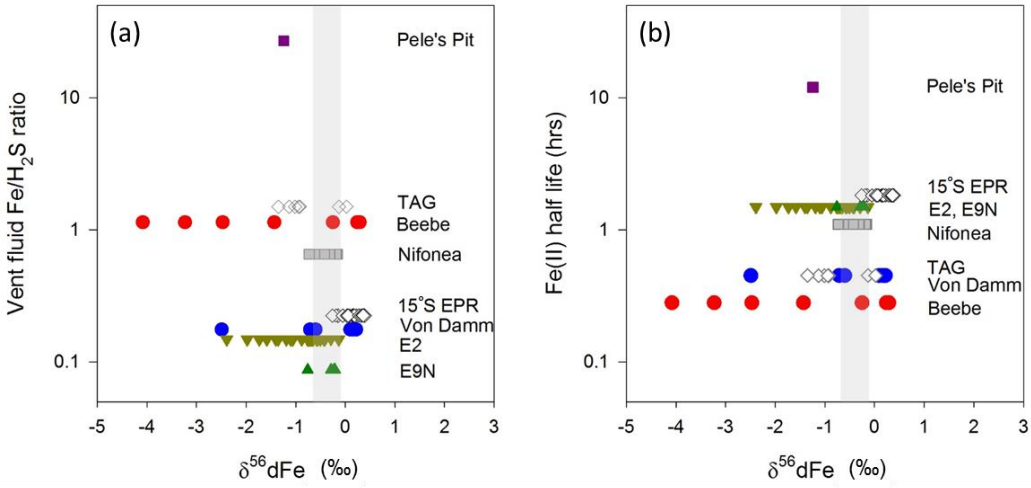

Figure 2-5 Range of δ^{56}Fe of dFe measured to date in hydrothermal plumes. Fe isotope data are from: this study (Beebe and Von Damm); *Conway and John (2014)* (TAG on the Mid-Atlantic Ridge); *Lough et al. (2017), Klar et al. (2017)* (E2 and E9N on the East Scotia Ridge); *Fitzsimmons et al. (2017)* (15°S East Pacific Rise); *Nasemann et al. (2018)* (Nifonea at Vanuatu back-arc); *Rouxel et al. (2018)* (Pele's Pit at Loihi Seamount). Additional vent fluid Fe/H_2S ratio and Fe(II) half-life data are from: *James et al. (2014)*; *Glazer and Rouxel (2009)*; *Field and Sherrell (2000)*; *Charlou et al. (1996)*. Literature data are summarised in Appendix (Table A5). In the figure, samples that were taken from section-wide studies (and therefore not representative of near-field plumes) are shown as open diamond symbols. δ^{56}Fe of the end-member hydrothermal fluids measured to date (Table A4) is indicated as the grey band.

The oxidation rate of Fe(II) is controlled by the oxygen concentration, pH, temperature and salinity of the evolving hydrothermal plume (*Millero et al., 1987*). Accordingly, Fe(II) oxidation rates tend to be faster in the Atlantic Ocean (minutes to ~1 hour; *Klar et al., 2017; Lough et al., 2019a, 2019b*), which has relatively high pH and high O_2 bottom waters, compared to the Pacific Ocean (~1-3 hours;

Nasemann et al., 2018; Field and Sherrell, 2000), where bottom waters tend to be relatively depleted in O_2 and have lower pH. Figure 2.5b suggests that, at least for samples collected from near-field hydrothermal plumes (and excluding Nifonea), there is a general trend towards lower δ^{56}dFe values with decreasing Fe(II) oxidation half-life. Thus, when the oxidation rate is fast, rapid conversion of Fe(II) to Fe(III) and precipitation of Fe-(oxyhydr)oxides produce an isotopically light δ^{56}dFe signal.

Considered together, the compiled data shown in Figure 2.5 support the idea that both the vent fluid Fe/H_2S ratio and the Fe(II) oxidation rate act as controls on the δ^{56}Fe signature of dissolved Fe that is delivered to the distal part of the hydrothermal plume and into the ocean interior. However, it is not possible to determine which of these two is the principal control from the presently available data. Analyses of δ^{56}Fe of dissolved Fe within the hydrothermal plume at Rainbow vent field on the Mid-Atlantic Ridge, that has vent fluid Fe/H_2S ratios of up to 24 and a relatively short Fe(II) oxidation half-life of ~0.29 h (*Severmann et al., 2004; Field and Sherrell, 2000*), may be useful to this end. Particles from the buoyant plume at Rainbow have been reported to have high δ^{56}Fe values (up to +1.3‰, *Severmann et al., 2004*), but there are, as yet, no published analyses of δ^{56}dFe in the Rainbow hydrothermal plume.

2.6 Conclusions

This study investigated the chemical processes that regulate the evolution of the iron isotopic signature of hydrothermal Fe during mixing between high-temperature vent fluids and seawater at the Beebe and the Von Damm vent fields on the Mid-Cayman ultraslow-spreading ridge. Hydrothermal vent fluids from Beebe had δ^{56}Fe = −0.28 ‰, similar to other vent sites, whereas vent fluids from Von Damm had slightly higher δ^{56}Fe (0.08‰), likely due to precipitation of Fe-sulfides that preferentially incorporate lighter Fe isotopes prior to venting at the seafloor. At Beebe, around 50% of hydrothermal Fe precipitates as Fe-sulfides during the early stages of mixing. Additionally, incubation experiments showed evidence for the presence of nanoparticulate Fe-sulfides in the Beebe buoyant plume that would eventually coagulate and precipitate in the distal plume. At both sites, the δ^{56}Fe value of dFe in the buoyant hydrothermal plume was significantly lower than the δ^{56}Fe value of the vent fluids (or background seawater), reaching values of as low as −4.08‰ at Beebe and −2.49‰ at Von Damm. This can be principally attributed to oxidation of Fe(II) and precipitation of the Fe(III) that forms. This is supported by analyses of δ^{56}TDFe; the estimated δ^{56}Fe values of labile particulate Fe are isotopically heavy (−0.13 to 0.71‰) compared to the dFe, suggesting that labile particulate Fe consists of Fe-(oxyhydr)oxides.

Comparisons between these data, and data collected at other hydrothermal sites, support the idea that the vent fluid Fe/H_2S ratio and the Fe(II) oxidation rate are the principal controls on the $\delta^{56}Fe$ signature of dissolved Fe that is delivered to the distal part of the hydrothermal plume and subsequently into the ocean interior. Inclusion of these parameters in ocean biogeochemical models of Fe distributions may help to better constrain the influence of inputs of hydrothermal Fe.

Chapter 3 Impact of hydrothermal venting on iron and chromium supply to the North Atlantic Ocean

3.1 Introduction

One of the most prominent findings of the GEOTRACES programme is that hydrothermal inputs of trace metals to the ocean can be detected many thousands of kilometers away from the vent fields (*Resing et al., 2015*). Hydrothermal venting at mid-ocean ridges emits fluids enriched in metals that have concentrations a million times higher than ambient seawater (*German and Seyfried, 2014*). However, the chemical processes in hydrothermal plumes that regulate the dispersal of ridge-derived metals remain poorly constrained (*German et al., 2016; Holmes et al., 2017*), making it difficult to assess the far field impacts of hydrothermal sources on the deep ocean metal inventory and, for some metals, on primary productivity in surface waters (*Tagliabue et al., 2014*).

The micronutrient iron (Fe) is a key regulator of primary productivity in large parts of the world's ocean (*Moore et al., 2001*) and therefore the biological carbon pump (*Martin, 1990*). The impact of past and future climate variabilities may be modulated by changes in Fe supply to the ocean (*Watson et al., 2000*), while the relative importance of different sources of Fe including atmospheric dust, marine sediments and hydrothermal vents is not well known (*Boyd and Ellwood, 2010*). Recent studies have shown that hydrothermal Fe may be stabilised in the dissolved (<0.2 μm) fraction in the form of organic complexes or nanoparticles (*Toner et al., 2009; Fitzsimmons et al., 2017; Findlay et al., 2019*), contradicting the previous consensus that hydrothermal activity is not a major source of Fe because of precipitation as the vent fluids mix with seawater (*German et al., 1991*).

The distribution of chromium (Cr) in the oceans is similar to that of the nutrient elements, with modest depletion of Cr in surface ocean relative to the deep ocean (*Jeandel and Minster,*

1987; Sirinawin et al., 2000). Low Cr concentrations in surface waters are thought to be due to biologically mediated reduction and scavenging but this is still debated (*Achterberg and van den Berg, 1997; Connelly et al., 2006; Semeniuk et al., 2016*). Cr in oxygenated seawater is primarily present as Cr(VI) in the form of chromate (CrO_4^{2-}) (*Elderfield, 1970*), which is the product of continental weathering (*Frei et al., 2009*). Cr is removed from the oceans through reduction to Cr(III), which is relatively insoluble and is scavenged by settling particles and subsequently buried in marine sediments (*Reinhard et al., 2014; Gueguen et al., 2016*). Whether hydrothermal vents are a net source or sink of Cr is not yet clear (*German et al., 1991; Sander and Koschinsky, 2000*), and estimated hydrothermal Cr fluxes vary by orders of magnitudes (*Rudnicki & Elderfield, 1993; Reinhard et al., 2013*).

Instrumental and methodological developments mean that it is now possible to accurately determine the stable isotope ratios of Fe (δ^{56}Fe) and Cr (δ^{53}Cr) in seawater (*Lacan et al., 2010; Bonnand et al., 2013*). Fe and Cr isotopes are emerging tools for assessing the provenance of metal inputs to the ocean, and for exploring the effects of biogeochemical cycling and redox processes. For example, the δ^{56}Fe value of dissolved Fe is in the range of −1.35‰ to 0.80‰ in the North Atlantic (*Conway and John, 2014*), reflecting the contributions of isotopically distinct Fe sources from dust dissolution (δ^{56}Fe ~0.68‰), reductive and non-reductive sedimentary release (δ^{56}Fe = −3.45‰ to −1.82‰ and 0 to 0.22‰, respectively: *Homoky et al., 2009; Homoky et al., 2013*), and hydrothermal venting (end-member vent fluid δ^{56}Fe = −0.67‰ to −0.12‰: *Beard et al., 2003; Severmann et al., 2004; Rouxel et al., 2008; Bennett et al., 2009; Klar et al., 2017; Nasemann et al., 2018*). The δ^{53}Cr values of dissolved Cr in seawater measured to date range from 0.4‰ to 1.6‰ (*Bonnand et al., 2013; Scheiderich et al., 2015; Paulukat et al., 2016; Goring-Harford et al., 2018; Moos and Boyle, 2019; Rickli et al., 2019; Janssen et al., 2020*). The variation in seawater δ^{53}Cr is thought to be driven by redox-dependent processes (*Scheiderich et al., 2015*), because Cr(VI) can be effectively reduced to Cr(III) in the presence of Fe(II) and/or organic matter, and this process is accompanied by a relatively large Cr isotope fractionation ($\delta^{53}Cr_{Cr(VI)} - \delta^{53}Cr_{Cr(III)}$ up to 4.2‰: *Døssing et al., 2011; Kitchen et al., 2012*).

While hydrothermal fluids are a source of Fe to the oceans, authigenic precipitation of hydrothermal Fe as Fe-sulfides and Fe-(oxyhydr)oxides occurs as the high-temperature vent fluids mix with seawater (*Klar et al., 2017; Lough et al., 2017*). However, it is now clear that a small fraction of hydrothermal Fe is stabilised in the form of organic complexes or nanoparticles that can be transported away from the vent fields, contributing to the dissolved Fe budget of the wider deep ocean (*Klar et al., 2017; Findlay et al., 2019*). Hydrothermal Cr, in the form of Cr(III), also precipitates as vent fluids mix with seawater via scavenging onto Fe-(oxyhydr)oxide particles (*Trocine and Trefry, 1988; German et al., 1991)*. In addition, Cr(VI) in ambient seawater may be partly reduced to Cr(III) on the surface of the Fe-(oxyhydr)oxide particles (*Sander and Koschinsky, 2000*). In support of this, hydrothermal sediments at the southern East Pacific Rise have been reported to have lower δ^{53}Cr value compared to seawater (*Bauer et al., 2019*). However, as yet, there have been no studies of the Cr isotope behaviour of dissolved Cr in hydrothermal systems.

To better understand the processes that regulate the ridge-derived fluxes of Fe and Cr dispersed through hydrothermal plumes, seawater samples were collected from directly above and close to the Trans-Atlantic Geotraverse (TAG) and Rainbow vent fields on the Mid-Atlantic Ridge. Plumes dispersing from the two vent fields mix with overlying ocean water with similar geochemistry, however, the vent fields have contrasting geologic settings. This study reports the results of analyses of dissolved Fe and Cr concentrations, dissolved Fe isotope (δ^{56}Fe) and Cr isotope (δ^{53}Cr) distributions, along with other supporting parameters. These results provide new insight into how hydrothermal Fe and Cr fluxes are modified by hydrothermal plume processes, and the role of hydrothermal venting in the oceanic Fe and Cr cycles.

3.2 Sampling sites

The Mid-Atlantic Ridge (MAR) is a slow-spreading plate boundary located along the seafloor of the Atlantic Ocean (Figure 3.1), moving at rates of less than 3 cm/yr.

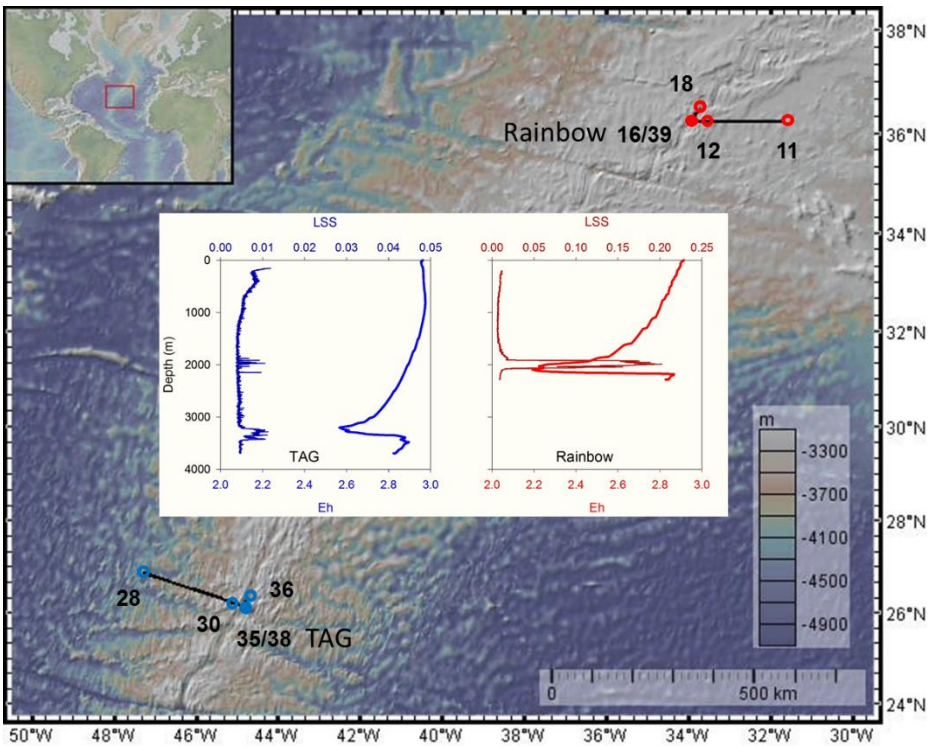

Figure 3-1 Locations of sampling stations at the TAG and Rainbow hydrothermal sites on the MAR, and LSS and Eh anomalies in water columns above the TAG and Rainbow vent fields. Map courtesy of http://www.geomapapp.org.

The Trans-Atlantic Geotraverse (TAG) vent field is located at 26°08' N 44°50' W and a depth of ~3650 m, at the base of the eastern wall of the rift valley of the MAR. Hosted in basaltic rocks, the TAG vent field consists of a series of high temperature (in excess of 360°C) black smokers that are clustered together close to the apex of a large sulfide mound (*Thompson et al., 1988*). The end-member vent fluids have pH of ~3, Fe concentration of 5.0-5.6 mM, manganese (Mn) concentrations of 0.68-0.73 mM, and H_2S content of ~3 mM (*Edmond et al., 1995; Chiba et al., 2001*). The vent field has also hosted lower temperature (265-300°C) white smoker fluids, but these have since become extinct (*Findlay et al., 2015*).

The Rainbow vent field is located at 36°14' N 33°54' W and ~2310 m depth, at the western end of a non-transform discontinuity cutting the MAR south of the Azores. The Rainbow vent field is hosted in ultramafic rocks (mainly serpentinised peridotite) and contains high

temperature (~365°C) black smokers. In contrast to TAG, the Rainbow vent fluids are characterised by low pH (2.8), high chlorinity (750 mM), high H_2 (16 mM) and abundant organic compounds (*Charlou et al., 2002*). They also have higher Fe (24 mM) and lower H_2S (1.2 mM) concentrations (*Charlou et al., 2002*). The lower pH, high concentrations of organic compounds, and high Fe are likely related to serpentinisation reactions (*Douville et al., 2002*).

At both vent sites, buoyant hydrothermal plumes rise several hundred meters into the water column. Plume dispersal is generally constrained along ridge axis trajectories (*Rudnicki et al., 1994; Edmonds and German, 2004*). In addition, upward mixing of rift valley confined waters driven by turbulence (*Ledwell et al., 2000; St Laurent et al., 2007; Vic et al., 2018; Tuerena et al., 2019*) likely occurs.

Hydrographically, the TAG and the Rainbow vent fields are overlaid by waters that mainly consist of Classical Labrador Sea Water (CLSW; *Jenkin et al., 2015*). Seawater samples collected from between 2000-3500 m water depth, within CLSW, at station USGT-18 (~1000 km away from the ridge) on the GEOTRACES GA03 transect have, on average, dissolved Mn concentrations of 0.15 nM (*Hatta et al., 2015*) and dissolved Fe concentrations and Fe isotope compositions of 0.48 nM and 0.69‰ (*Conway et al, 2014*); these values are considered to represent background seawater (CLSW) in this study.

3.3 Methods

3.3.1 Sample collection

Samples for this study were collected on board RRS *James Cook* (JC156 cruise) as part of the UK GEOTRACES North Atlantic GA13 transect between 20th of December 2017 and 1st of February 2018, using pre-cleaned 10 L Ocean Test Equipment (OTE) water sampling bottles that were mounted on a titanium rosette system. On recovery, the OTE bottles were transferred into a trace metal clean container for sub-sampling. Seawater was filtered through a Sartobran 300 (Sartorius) filter capsule (0.2 µm) or a polyethersulfone filter (PES, Supor, Pall

Gelman, 0.2 µm) under gentle pressure, and was collected into acid-cleaned low-density polyethylene (LDPE) bottles. These samples for the analysis of dissolved trace metals (dMe) were then preserved by adding UpA-grade hydrochloric acid (HCl, Romil) to 0.024 M immediately after collection, and were stored for several months before the isotope analysis.

A Seabird 911 plus conductivity, temperature and depth (CTD) profiler system together with a light scattering sensor (LSS) and an Eh detector were also attached to the titanium rosette. The hydrothermal plume above the vent fields was identified by a positive LSS signal, a negative Eh signal, along with temperature anomalies, and was sampled at water column depths of between 3200-3500 m and 1900-2200 m above TAG (Station 35/38) and Rainbow (Station 16/39), respectively. Particle-rich plumes were also detected by a positive LSS anomaly to the north of TAG (Station 36), and at stations to the north (Station 18) and east of Rainbow (Station 12). Locations of the sampling stations together with sensor profiles through the plumes are summarised in Figure 3.1.

3.3.2 Incubation experiment

To investigate how hydrothermally sourced Fe and δ^{56}Fe may evolve during plume dispersal (*Mellett et al., in prep.*), onboard incubations of seawater samples from the hydrothermal plume were carried out in 20 L polycarbonate carboys that had been acid cleaned. First, the carboy was rinsed and filled with either unfiltered or filtered (0.2 µm) seawater. Then, the carboys were wrapped in black constructor bags and taken into a temperature controlled room maintained at ~13°C.

Seawater was sampled from the carboy at intervals of between several hours to up to one week, by first inverting the carboy at least 3 times to re-suspend any particles, and then collecting a sub-sample of water into a 2.5 L polycarbonate bottle. The seawater sub-sample was then filtered first through a 3 µm and then through a 0.4 µm polycarbonate track etched (PCTE) filter that was housed in a two-stage custom-built filtration rig. Samples were collected in 125 or 250 mL LDPE bottles and acidified to pH <2 with UpA-grade HCl (Romil) for later analysis.

The incubation experiment at Rainbow (Station 39) utilised seawater collected from 2241 m water depth, where large Eh and LSS anomalies were measured. Seawater samples for the TAG (Station 35) incubation experiment were also from the hydrothermal plume; samples from water depths of 3344 m and 3277 m were combined for the unfiltered treatment, and samples from water depths of 3346 m and 3263 m were combined for the filtered treatment.

3.3.3 Fe and Cr isotope analysis

All acids used for chemical processing were thermally distilled. Milli-Q (MQ) water was used for diluting and for cleaning. LDPE bottles and Perfluoroalkoxy (PFA) vials were thoroughly cleaned for trace metal purposes. Samples were handled under laminar flow hoods, set within Class 100 clean laboratories at the University of Southampton and National Oceanography Centre.

Dissolved Fe concentrations were measured at sea using flow injection analysis with chemiluminescence detection (FIA-CL; *Obata et al., 1993*). Dissolved Cr concentrations were initially measured using a $Mg(OH)_2$ co-precipitation method (*Moos and Boyle et al., 2019; Rickli et al., 2019*). The initial determinations of dFe and dCr were used to optimise isotope spiking.

The Fe isotope compositions of seawater samples were determined using a ^{57}Fe-^{58}Fe double spike technique, adapted from *Lacan et al. (2010)*. Samples of between 0.5 and 2 L volume were pre-concentrated using NTA Superflow resin, and were then purified by anion exchange chromatography using AG-MP1 resin (Biorad). The Cr isotope compositions were determined using a ^{50}Cr-^{54}Cr double spike method adapted from *Bonnand et al. (2013)*. Cr in seawater samples of 1 L to 2 L volume was co-precipitated with Fe(II) hydroxide. Then Cr was separated from the Fe by anion exchange chromatography (Biorad AG1-X8), and further purified by processing through a cation exchange (Biorad AG 50W-X12) column. The purified Fe or Cr samples were evaporated to dryness and re-dissolved in 0.3 M (Fe) or 0.45 M (Cr) HNO_3 for analysis of their isotope ratios. Full details of the analytical procedures are given in Appendix B.

The isotopic compositions of Fe and Cr were determined by multicollector inductively coupled plasma mass spectrometry (MC-ICP-MS; Thermo Fisher Neptune Plus) at the University of Southampton. The final Fe or Cr isotope values of the samples are reported in delta notation relative to international isotope standards and expressed as:

$$\delta^{56}Fe\ (‰) = [(^{56}Fe/^{54}Fe)_{sample}/(^{56}Fe/^{54}Fe)_{IRMM\text{-}14} - 1] \times 1000 \quad (3\text{-}1)$$

$$\delta^{53}Cr\ (‰) = [(^{53}Cr/^{52}Cr)_{sample}/(^{53}Cr/^{52}Cr)_{NBS979} - 1] \times 1000 \quad (3\text{-}2)$$

The precision and accuracy of the above methods were assessed through the analysis of: (1) Trace metal free seawater doped with a hematite (HEM) Fe isotope standard, (2) Black Sea Fe intercomparison 'anoxic' sample, and (3) OSIL Atlantic salinity standard seawater. Results of these analyses are in agreement with values reported in the literature for these materials (Table 3.1).

Table 3-1 Fe and Cr isotope compositions for method validation samples. NA = not available; here the 2SD is the uncertainty on more than one MC-ICP-MS analyses of the same sample.

Sample	**$\delta^{56}Fe$ (‰)**	**2SD**	**n**	**Recommended value**	**Reference**
Iron free seawater doped with hematite (HEM) Fe isotope standard				0.25 ± 0.06‰	*Klar et al., 2017*
HEM (1)	0.22	0.09	3		
HEM (2)	0.23	0.10	2		
HEM (3)	0.23	NA	1		
Black Sea Fe isotope intercomparison sample (anoxic, 150 m depth)				−0.79 ± 0.03‰	*Rolison et al., 2018*
BS-IC-anoxic (1)	−0.82	0.04	2		
Sample	**$\delta^{53}Cr$ (‰)**	**2SD**		**Recommended value**	**Reference**
OSIL Atlantic salinity standard seawater (batch of December 2017)				0.96 ± 0.06‰	*Scheiderich et al., 2015*
OSIL (1)	0.93	0.02	2		
OSIL (2)	0.95	0.01	2		
OSIL (3)	1.00	NA	1		
OSIL (4)	0.98	NA	1		

3.3.4 Ancillary analyses

Seawater samples were also collected for the analysis of total dissolvable metal (TDMe) concentrations. Samples were acidified with UpA-grade HCl (Romil) to 0.024 M. Back in the clean laboratory at the University of Southampton, the samples were extracted and pre-concentrated on an amino carboxylic acid type chelating resin (CM-PEHA; *Kagaya et al., 2009*). The concentrations of total dissolvable Fe (TDFe) were then determined with ICP-MS (Thermo Scientific Element).

Measurements of dissolved Fe(II) concentrations were made on board the ship by FIA-CL immediately after collection of the samples. The Fe(II) samples were filtered either inline or prior to analysis with a 0.2 µm PES syringe filter, and buffered inline to pH ~5.5 prior to pre-concentration on a column filled with 8-hydroxyquinoline (8-HQ) chelating resin (*Bowie et al., 2005*).

Dissolved mangnese (Mn) concentrations were determined on board by flow injection analysis with inline pre-concentration on resin-immobilized 8-HQ and colorimetric detection (*Resing and Mottl, 1992*). A drift standard as well as SAFe reference samples were analysed at the same time as the samples.

The measured TDFe and dFe(II) concentrations were used to support Rayleigh fractionation modeling (Section 3.5.1). The Mn concentrations were used to calculate the dilution factors for vent waters within the hydrothermal and particle-rich plumes.

3.3.5 Dilution factor calculations

Mn shows near-conservative behaviour during mixing of vent fluids and seawater, and therefore serves as a tracer of hydrothermal plume dispersal on the spatial scales of the sampling (*James and Elderfield, 1996*). The vent fluid (VF) dilution factor can be determined from the proportion of vent fluid serived Mn and seawater derived Mn in a water sample, i.e. dilution factor = $([Mn]_{VF} - [Mn]_{SW}) / ([Mn]_{sample} - [Mn]_{SW})$, where $[Mn]_{sample}$ is the measured sample Mn concentration, $[Mn]_{SW}$ is the Mn concentration of background seawater (0.15 nM;

Hatta et al., 2015) and $[Mn]_{VF}$ is the Mn content of the end-member vent fluid. At TAG, $[Mn]_{VF}$ = ~710 µM and at Rainbow $[Mn]_{VF}$ = ~2250 µM (*Chiba et al., 2001; Charlou et al., 2002*).

The plume dilution factor is used as a measure of the dilution of the least dilute plume sample as the plume becomes neutrally buoyant and spreads out laterally along an isopycnal. It is calculated as $([Mn]_{plume} - [Mn]_{SW}) / ([Mn]_{sample} - [Mn]_{SW})$, where $[Mn]_{plume}$ represents the highest Mn concentration of the least dilute hydrothermal plume samples (41 nM and 297 nM at TAG and Rainbow respectively).

3.4 Results

Water column profiles of dissolved Fe (dFe) concentrations and dissolved Fe isotope composition (δ^{56}dFe) at the TAG and the Rainbow stations are shown in Figure 3.2. Within the TAG hydrothermal plume (3200-3500 m), dFe concentrations were as high as 68.0 nM while δ^{56}dFe values were as low as −1.83‰. The Rainbow hydrothermal plume (1900-2200 m) was characterised by elevated dFe concentrations of up to 59.6 nM and very low δ^{56}dFe values, as low as −6.95‰. The Fe isotope compositions of the TAG and Rainbow end-member vent fluids are reported to be −0.15‰ and −0.14‰, respectively (*Severmann et al., 2004*), indicating that Fe sourced from the vent fluid is isotopically fractionated as the vent fluids mix with ambient seawater.

As the hydrothermal plume disperses and becomes more dilute, dFe concentrations decrease to < 6 nM), whereas δ^{56}dFe evolves to higher values (−0.44‰ to 0.17‰ and −0.11‰ to 0.23‰, respectively, in the particle-rich plumes at stations close to TAG and Rainbow). For the same degree of dilution, samples from the Rainbow particle plume (Stations 18 and 12) tend to have slightly higher dFe and δ^{56}dFe values compared to samples from the TAG particle plume (Station 36).

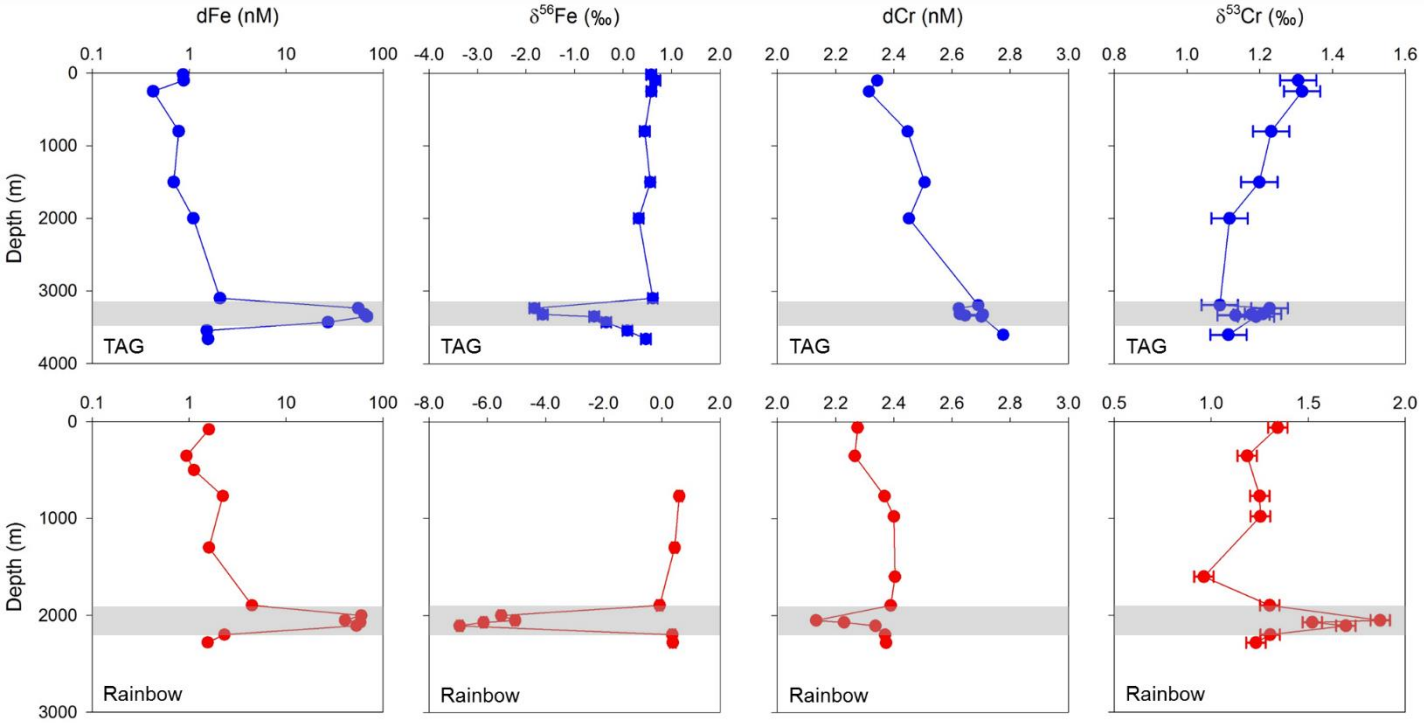

Figure 3-2 Depth profiles of dissolved Fe and Cr concentrations, and δ^{56}Fe and δ^{53}Cr values, at the TAG station (**top panels**) and the Rainbow station (**bottom panels**). The hydrothermal plume depths (3200-3500 m and 1900-2200 m, respectively, at TAG and Rainbow) are highlighted by grey horizontal bands. Error bars for Fe and Cr concentrations are smaller than the size of data point markers. Error bars for δ^{56}Fe and δ^{53}Cr represent external reproducibility (± 0.10‰ and ± 0.05‰, respectively) based on the long-term precision of the iron and chromium isotope standards (ETH and NBS979). All data are given in Table B2, B3 (Appendix B).

Results from the onboard incubation experiment (Table 3.2) show that dFe concentrations progressively decrease over time (i.e. as the plume continues to disperse). By contrast, the δ^{56}dFe value of the subsamples from the filtered treatment remained relatively constant over the course of the experiment (−1.43‰ to −1.35‰ for the TAG incubation, and −7.45‰ to −7.14‰ for Rainbow). However, the δ^{56}dFe values of the unfiltered seawater became isotopically heavier over time (up to 3.57‰ and up to 1.17‰ for TAG and Rainbow, respectively).

Table 3-2 Results of the Fe incubation experiments. Seawater samples were taken from near-field hydrothermal plumes at TAG and Rainbow, and were stored in carboys for ~0.1 to 5 days before they were subsampled and filtered. Filtered treatment means that the original sample was filtered, while unfiltered treatment means it was not filtered, so hydrothermal plume particles were present in the carboy during the incubation. NA = not available; here 2SD is the uncertainty on two or three MC-ICP-MS measurements of the same sample.

Sample description	Time point (day)	δ^{56}dFe (‰)	2SD (‰)	dFe (nM)
TAG (Station 35)				
Filtered treatment	0.15	-1.43	0.03	75.2
Filtered treatment	1	-1.34	0.09	84.2
Filtered treatment	5	-1.35	0.05	21.0
Unfiltered treatment	0.15	0.58	0.03	149.6
Unfiltered treatment	1	0.09	0.02	162.3
Unfiltered treatment	5	3.57	0.01	73.5
Rainbow (Station 39)				
Filtered treatment	0.1	-7.34	0.03	280.4
Filtered treatment	0.5	-7.45	0.02	206.0
Filtered treatment	5	-7.14	NA	47.0
Unfiltered treatment	0.1	0.76	0.04	345.6
Unfiltered treatment	0.5	-0.16	0.03	202.9
Unfiltered treatment	5	1.17	NA	175.0

In contrast to Fe, dissolved Cr (dCr) was slightly depleted in the hydrothermal plumes compared to ambient seawater; the lowest concentration at TAG was 2.62 nM, compared to a background value of 2.73 nM, and the lowest concentration at Rainbow was 2.13 nM, compared to a background value of 2.38 nM. Samples from the hydrothermal plume also had elevated δ^{53}Cr values compared to ambient seawater, up to 1.23‰ (background = 1.10‰) and 1.87‰ (background = 1.27‰), respectively, in the TAG and Rainbow hydrothermal plumes. The 'mirror image' of Fe and Cr isotope profiles (Figure 3.2) strongly suggests the coupled cycling of Fe and Cr in the hydrothermal plume.

3.5 Discussion

3.5.1 Fe isotope behavior in the near-field hydrothermal plume

Fe(II) in hydrothermal fluids can be expected to precipitate as Fe-sulfide (FeS and FeS_2) within a few seconds of being expelled at the seafloor (*Rudnicki and Elderfield, 1993*). Kinetic Fe-sulfide precipitation would leave the residual dissolved Fe enriched in heavier iron isotopes (estimated $\delta^{56}Fe_{FeS} - \delta^{56}dFe = -0.60‰$: *Butler et al., 2005; Bennett et al., 2009*). The effect of precipitation of the vent fluid Fe as sulfide can be examined using a Rayleigh fractionation model:

$$\delta^{56}\mathrm{Fe} = (\delta^{56}\mathrm{Fe_{VF}} + 1000) \cdot f^{\alpha-1} - 1000 \quad (3\text{-}3)$$

where $\delta^{56}Fe_{VF}$ is the Fe isotope composition of the end-member vent fluid, α is the fractionation factor between FeS and Fe(II) (~0.9994; given by $\alpha \approx e^{\delta^{56}\mathrm{Fe_{FeS}} - \delta^{56}\mathrm{Fe}}$), and f is the proportion of Fe remaining in the plume. Given that Fe-sulfides form large aggregates (>20 µm) and settle out of the plume fast (*Feely et al., 1994; Yücel et al., 2011; Carazzo et al. 2013; Lough et al., 2017*), the f value can be estimated by the ratio of the measured to the calculated total Fe concentration in the hydrothermal plume:

$$f = \frac{[\mathrm{TDFe}]\mathrm{meas}}{[\mathrm{Fe}]_{\mathrm{VF}} \,/\, [\text{VF dilution factor}]} \quad (3\text{-}4)$$

where $[TDFe]_{meas}$ is the concentration of total dissolved Fe in the sample. According to this calculation, the proportion of Fe lost via precipitation of Fe-sulfide during the early stages of mixing between the hydrothermal fluid and seawater was ~20% at TAG and ~7% at Rainbow (see Table 3.3). These derived values are consistent with the vent fluid Fe/H_2S stoichiometry: vent fluids from Rainbow have higher Fe/H_2S (~20) compared to TAG vent fluids (~1.5) (*Severmann et al., 2004*), so a greater proportion of Fe remains in solution. Thus, according to Eq. 3-3, the $\delta^{56}Fe$ value of hydrothermal Fe that remains in the dissolved phase and is transported upwards into the hydrothermal plume is calculated to be −0.01‰ and −0.10‰, respectively, at TAG and Rainbow.

However, the δ^{56}Fe values of dFe in the hydrothermal plumes at both sites were much lower than these values (as low as −1.83‰ at TAG and −6.95‰ at Rainbow). Precipitation of Fe-(oxhyhydr)oxides (FeOOH) fractionates Fe isotopes; preferential incorporation of heavy Fe isotopes into FeOOH ($\delta^{56}Fe_{FeOOH} - \delta^{56}$dFe ≈ 3.5‰ at a temperature of 3°C: *Welch et al., 2003; Wu et al., 2011*) leaves the Fe that remains in the dissolved fraction isotopically light. The theoretical oxidation half-life of Fe(II) is as short as 0.45 h in ambient seawater at the TAG vent site and 0.29 h at Rainbow (*Field and Sherrell, 2000*). Thus, with continuous mixing of vent fluids and oxygenated seawater, the effects of FeS precipitation are overwritten by Fe(II)-Fe(III) oxidation. The evolution of δ^{56}dFe in the hydrothermal plume can also be modelled in terms of Rayleigh fractionation, as a function of the proportion (*F*) of Fe(II) oxidised to Fe(III) along with the proportion (*X*) of Fe(III) precipitated as FeOOH (*Klar et al., 2017; Lough et al., 2017; Nasemann et al., 2018*):

$$\delta^{56}\mathrm{Fe(II)} = (\delta^{56}\mathrm{Fe(II)}_0 + 1000) \cdot F^{\alpha-1} - 1000 \quad (3\text{-}5)$$

$$\delta^{56}\mathrm{Fe(III)} = (\delta^{56}\mathrm{Fe(II)}_0 + 1000) \cdot \frac{1-F^{\alpha}}{1-F} - 1000 \quad (3\text{-}6)$$

$$\delta^{56}\mathrm{dFe} = \frac{F \cdot \delta^{56}\mathrm{Fe(II)} + X \cdot (1-F) \cdot \delta^{56}\mathrm{Fe(III)}}{F + X \cdot (1-F)} \quad (3\text{-}7)$$

where $\delta^{56}Fe(II)_0$ is the initial isotopic composition of dissolved Fe (−0.01‰ at TAG and −0.10‰ at Rainbow, to account for the effect of Fe-sulfide precipitation), δ^{56}Fe(II) is the isotopic composition of the remaining Fe(II), δ^{56}Fe(III) is the Fe isotopic composition of precipitated Fe(III), and α is the fractionation factor between aqueous Fe(II) and precipitated Fe(III) (~1.0035; given by $\alpha \approx e^{\delta^{56}\mathrm{Fe(III)} - \delta^{56}\mathrm{Fe(II)_{aq}}}$).

The results of this modelling exercise are illustrated in Figure 3.3. The observed low δ^{56}dFe values in the TAG and Rainbow hydrothermal plumes are consistent with a substantial degree of Fe(II) oxidation and FeOOH precipitation. This result is consistent with calculations based on measured concentrations of dFe(II), dFe and TDFe (Table 3.3). Assuming that Fe-(oxyhydr)oxides have relatively small particle sizes and tend to remain in the plume

(*Fitzsimmons et al., 2017; Hoffman et al., 2018; Lough et al., 2019*), then *F* and *X* values can also be estimated as follows:

$$F = \frac{[\mathrm{dFe(II)}]}{[\mathrm{TDFe}]} \quad (3\text{-}8)$$

$$X = \frac{[\mathrm{dFe}]-[\mathrm{dFe(II)}]}{[\mathrm{TDFe}]-[\mathrm{dFe(II)}]} \quad (3\text{-}9)$$

The proportion of Fe remaining as Fe(II) is calculated to be ~4-7% at TAG and ~0.1-0.4% at Rainbow, and the proportion of Fe(III) remaining in the dissolved fraction is ~25-53% and ~1-4% at the two sites respectively (Table 3.3). The utilisation of these values to parameterise the Rayleigh model therefore provides a reliable prediction of the hydrothermal δ^{56}dFe signal in the near-field plume.

Differences in δ^{56}Fe values between the two sites reflect differences in the proportion of dissolved Fe that precipitates as Fe-sulfide versus Fe-(oxhyhydr)oxide. The Rainbow vent fluids have far higher Fe/H_2S (~20) than the TAG vent fluids (~1.5), so more Fe is available for Fe-(oxyhydr)oxide formation as the vent fluids mix with seawater. In turn, owing to particle concentration effects (*Stordal et al., 1996*), the rate of aggregation of colloidal FeOOH ('colloidal pumping') increases in presence of a high particle loading (i.e. particulate Fe-(oxyhydr)oxides). As a result, near quantitative (>99%) oxidation and precipitation of Fe occurs in the Rainbow hydrothermal plume, resulting in the lowest δ^{56}Fe value for dFe in seawater reported to date (−6.95‰).

As discussed in Chapter 2, the δ^{56}dFe signal in the near-field plume that is subsequently delivered to the ocean interior is influenced by both the vent fluid chemistry and the chemistry of overlying seawater that mixes with the fluids. Examples for inter-comparison include the Vanuatu back-arc and the 15°S East Pacific Rise, where substantial sulfide exists relative to Fe in the vent fluids (*Nasemann et al., 2018; Charlou et al., 1996*) and oxidation rate is slow as the Pacific Ocean exhibits lower oxygen levels and lower pH compared to the Atlantic (*Field and Sherrell, 2000*). As a result of sluggish Fe(II)-Fe(III) oxidation and limited Fe-(oxyhydr)oxide precipitation, the δ^{56}Fe values of dFe in hydrothermal plumes had narrower ranges (−0.73‰

to −0.16‰ and −0.26‰ to 0.39‰ respectively: *Nasemann et al., 2018; Fitzsimmons et al., 2017*) compared to what have been observed at TAG and Rainbow in this study.

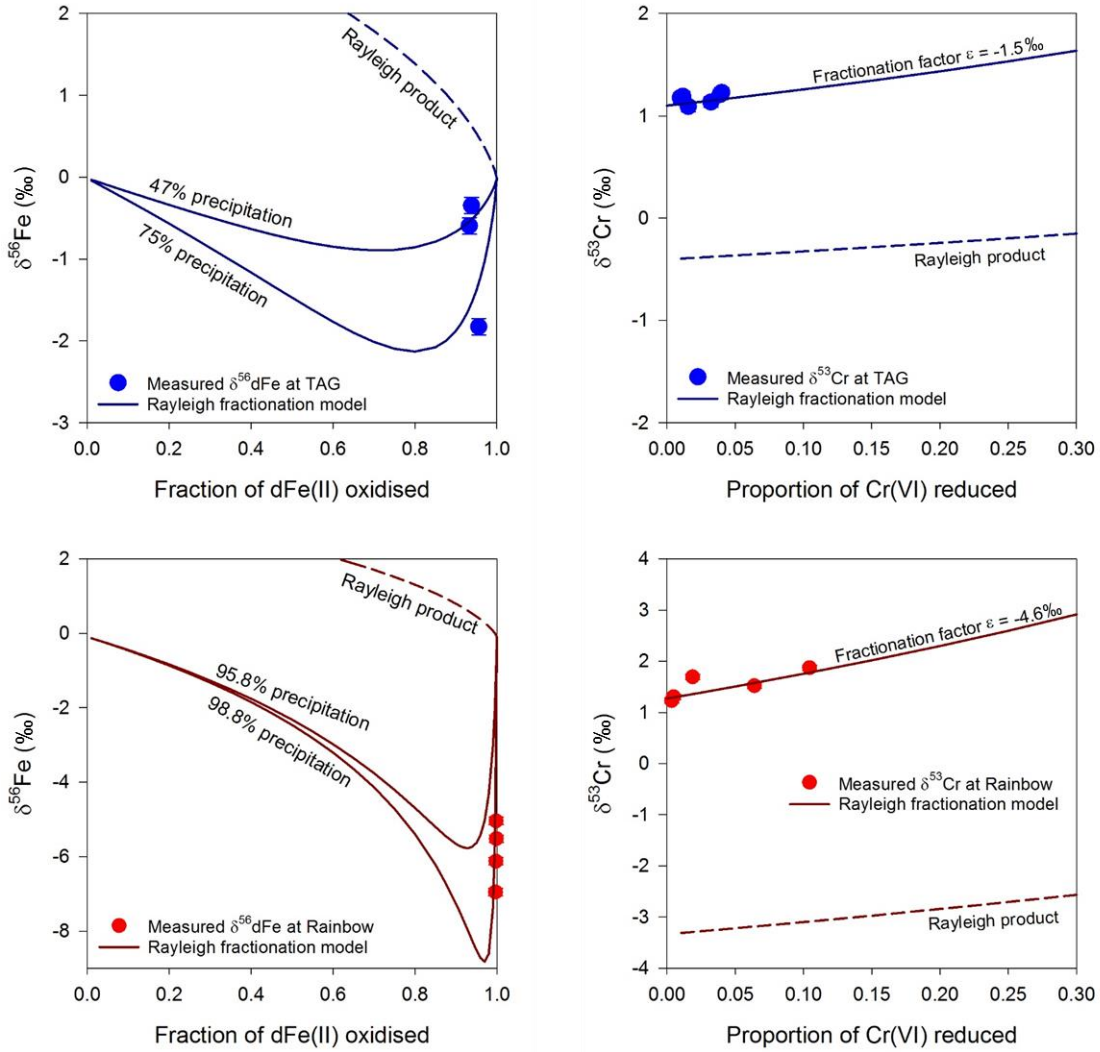

Figure 3-3 Rayleigh models of Fe and Cr isotope fractionation in the TAG and Rainbow hydrothermal plumes. **Left panels**: δ^{56}Fe relative to the fraction of dFe(II) oxidised to Fe(III). Solid lines show the evolution of δ^{56}Fe predicted by Rayleigh fractionation modelling of Fe(II)-Fe(III) oxidation. Fractionation factor between aqueous Fe(II) and precipitated Fe(III), α, is 1.0035. Initial dFe(II) isotope compositions are $\delta^{56}Fe(II)_0$ = −0.01‰ and −0.10‰ at the TAG and Rainbow vent fields respectively. **Right panels**: δ^{53}Cr relative to the proportion of Cr(VI) reduced to Cr(III) and removed. The solid line shows the evolution of δ^{53}Cr predicted by Rayleigh fractionation modelling of Cr(VI)-Cr(III) reduction. Initial dCr isotope compositions are $\delta^{53}Cr_{sw}$ = 1.10‰ and 1.27‰ at TAG and Rainbow, respectively. See Section 3.5.2 for detail.

Table 3-3 Parameters used to calculate estimated variables (*f*, *F* and *X*; Section 3.5.1) that are utilised to constrain the Rayleigh model for investigating the effects of precipitation of Fe-sulfides and Fe-(oxyhydr)oxides. Methods for determining the Fe and Mn concentrations are described in Section 3.3.4, calculations of the hydrothermal plume and vent fluid dilution factors are described in Section 3.3.5.

Measured parameters						Calculated parameters					
						Dilution factor					
Depth (m)	δ^{56}Fe (‰)	dFe (nM)	dFeII (nM)	dMn (nM)	TDFe (nM)	Plume	Vent fluid	TDFe (nM) [a]	*f* value Eq. 3-4	*F* value Eq. 3-8	*X* value Eq. 3-9
TAG (Station 35)											
3236	-1.83	55.2	8.7	41.0	196	1.0	17324	298		4.4%	24.9%
3350	-0.59	68.1	8.1	20.6	121	2.0	34409	150		6.7%	53.2%
3429	-0.35	27.0	4.7	6.1	77	6.9	117224	44		6.2%	31.0%
Average					131			164	80%		
Rainbow (Station 16)											
2001	-5.52	59.6	2.0	152.0	1360	2.0	14800	1622		0.1%	4.2%
2051	-5.04	40.5	3.4	184.6	1625	1.6	12187	1969		0.2%	2.3%
2072	-6.12	58.2	4.4	178.3	1660	1.7	12617	1902		0.3%	3.2%
2108	-6.95	53.1	12.8	296.8	3432	1.0	7582	3165		0.4%	1.2%
Average					2019			2165	93%		

[a] End-member vent fluid Fe concentration $[Fe]_{VF}$ = 5170 µM at TAG and 24000 µM at Rainbow (*Chiba et al., 2001; Charlou et al., 2002; Findlay et al., 2015*).

3.5.2 Cr isotope behavior in the near-field hydrothermal plume

The Cr isotope composition of hydrothermal vent fluids at basalt-hosted vent fields is currently unknown but is expected to be similar to that of igneous rocks ($\delta^{53}Cr = -0.12 \pm 0.10‰$: *Schoenberg et al., 2008*), assuming that Cr is extracted from the rock without significant isotope fractionation. At ultramafic-influenced vent sites, interaction with serpentinised rocks that can have relatively high $\delta^{53}Cr$ values (up to 1.22‰: *Farkaš et al., 2013*), may produce hydrothermal fluids that are enriched in heavy Cr isotopes relative to igneous crust. However, the concentration of Cr in hydrothermal vent fluids is predicted to be relatively low (< 2000 nM) compared to other trace metals because of the limited solubility of reduced species of Cr in hydrothermal fluids (*Huang et al., 2019*) and, in support of this, the estimated Cr concentration of end-member hydrothermal fluids from the North Fiji Basin was predicted to be ~1200 nM based on extrapolation of analyses of low temperature diffuse fluids (*Sander and Koschinsky, 2000*).

Analyses of hydrothermal plume particles suggested that Cr in hydrothermal fluids coprecipitates with iron almost immediately on expulsion at the seafloor (*German et al., 1991*). The measured molar Cr/Fe ratio of freshly precipitated particles has been determined to be in the range ~2×10^{-4} to ~5×10^{-4} (*German et al., 1991; Trocine and Trefry, 1988; Feely et al., 1996*), which is ~2 orders of magnitude higher than the expected Cr/Fe ratio of vent fluids, suggesting that the greater part of the particulate Cr is derived from ambient seawater (*Rudnicki and Elderfield, 1993*). As hydrothermal particles collected from the TAG neutrally buoyant plume showed a linear correlation between particulate Fe and Cr concentrations, *German et al. (1991)* hypothesised that uptake of Cr from ambient seawater only occurs during the early stages of mixing between vent fluids and seawater, when the rate of precipitation of Fe-(oxyhydr)oxides is highest. Uptake of Cr from seawater onto hydrothermal plume particles may also be revealed by analysis of the chemical composition of metalliferous sediments from the southern East Pacific Rise (*Bauer et al., 2019*). These authors have shown that the authigenic phase of the sediments has a relatively low $\delta^{53}Cr$ value (as low as −1.2‰) that would be consistent with partial reduction of Cr(VI) in ambient seawater and incorporation of the isotopically light Cr(III) that forms into metalliferous particles (*Bauer et al., 2019*).

For the first time, my data reveal that the Fe and Cr isotope profiles through the hydrothermal plume at both Rainbow and TAG are the mirror image of one another (Figure 3.2). This provides compelling evidence for coupled Fe(II) oxidation and Cr(VI) reduction in the hydrothermal plume. In the presence of Fe(II) or Fe(II)-bearing minerals, Cr(VI) is therefore effectively reduced to Cr(III), which preferentially incorporates light Cr isotopes (*Ellis et al., 2002; Frei et al., 2009*). The Cr(III) is

scavenged by Fe-(oxyhydr)oxide particles, leaving the Cr(VI) that remains in the dissolved fraction isotopically heavy. Cr(III) could be re-oxidised in a catalytic reaction with MnO_2, however, this process is likely negligible given the very slow rates of Mn(II) oxidation (*Morgan, 2005*) and Cr oxidation (*Eary and Rai, 1987*).

The evolution of δ^{53}dCr in the hydrothermal plume due to reduction of Cr(VI) and removal of the Cr(III) that forms can be described in terms of a closed-system Rayleigh process:

$$\delta^{53}\mathrm{dCr} = (\delta^{53}\mathrm{Cr_{sw}} + 1000) \cdot p^{\alpha-1} - 1000 \quad (3\text{-}10)$$

where SW is background seawater, α is the fractionation factor between Cr(III) and Cr(VI), and p is the proportion of Cr remaining in the dissolved fraction given by:

$$p = \frac{\mathrm{dCr}}{[\mathrm{Cr}]_{\mathrm{SW}}} \quad (3\text{-}11)$$

Background seawater is assumed to be represented by the average values of seawater samples collected from just above and below the hydrothermal plume (Table B3): $\delta^{53}Cr_{sw}$ = 1.10‰ at TAG and 1.27‰ at Rainbow, and $[Cr]_{SW}$ = 2.73 nM and 2.38 nM at TAG and Rainbow, respectively.

Figure 3.3 shows that the estimated fractionation factor between Cr(III) and Cr(VI) is ~ −1.5‰ for TAG and −4.6‰ for Rainbow. Experimentally determined fractionation factors for reduction of Cr(VI) by ferrous Fe are in the range of −3.60‰ to −4.20‰ (*Døssing et al., 2011; Kitchen et al., 2012*), whilst Fe(II)-bearing minerals, such as FeS and green rust, are thought to have more muted values (−1.50‰ to −2.65‰: *Døssing et al., 2011; Basu and Johnson, 2012*). Similarly, the fractionation factor between Cr(III) in the authigenic phase of metalliferous sediments and Cr in seawater for the southern East Pacific Rise has been estimated to be between −0.80‰ and −2.65‰ (*Bauer et al., 2019*). Thus, my estimated fractionation factors are in agreement with both the experimental and the field data. The lower fractionation factor determined for TAG may indicate that Fe-sulfide particles exert a greater control on Cr reduction; the very high Fe/H_2S ratio in Rainbow hydrothermal fluids means that a greater proportion of Fe precipitates as (oxyhydr)oxides at this site.

The previously proposed 'global correlation' between the Cr concentration and δ^{53}Cr value of seawater samples is consistent with closed-system Rayleigh-type fractionation of Cr isotopes in the open ocean characterised by a single fractionation factor (~ −0.80‰, *Scheiderich et al., 2015*), but the underlying processes that regulate this relationship are not well constrained (*Rickli et al., 2019*). My full water column Cr data at the TAG station yield an overall fractionation factor of −0.87‰, which is consistent with the 'global correlation', but it is clear from Figure 3.4 that the hydrothermal plume samples at Rainbow have anomalously high δ^{53}Cr values compared to the 'global correlation'

line. Similar anomalously high δ^{53}Cr values (δ^{53}Cr up to 3.85‰ and 4.15‰) have been observed in seawater samples collected from the Chukchi shelf (*Moos, 2018*). These have been attributed to reduction of seawater Cr by Fe(II) diffusing from the reducing shelf sediments. Thus, the relatively small fractionation factor of Cr inferred from the global seawater dataset is not consistent with Cr reduction by Fe(II).

Reduction of Cr(VI) in the hydrothermal plume is not quantitative even if the Fe(II) supply is efficient, as my data indicate that the proportion of seawater Cr that was removed from the dissolved fraction was no higher than 4% at TAG and 10% at Rainbow. According to the Rayleigh model, the δ^{53}Cr value of particulate Cr(III) in the hydrothermal plume would be predicted to be isotopically light relative to seawater Cr(VI), with δ^{53}Cr values of ~0.20‰ at TAG and −2.57‰ to −2.75‰ at Rainbow (Figure 3.3). The δ^{53}Cr offset between Cr(III) and Cr(VI) means that the δ^{53}Cr values of Cr deposited in metalliferous sediments would not faithfully reflect the Cr isotope composition of seawater, and should not be directly used to track the seawater δ^{53}Cr evolution in the geological past.

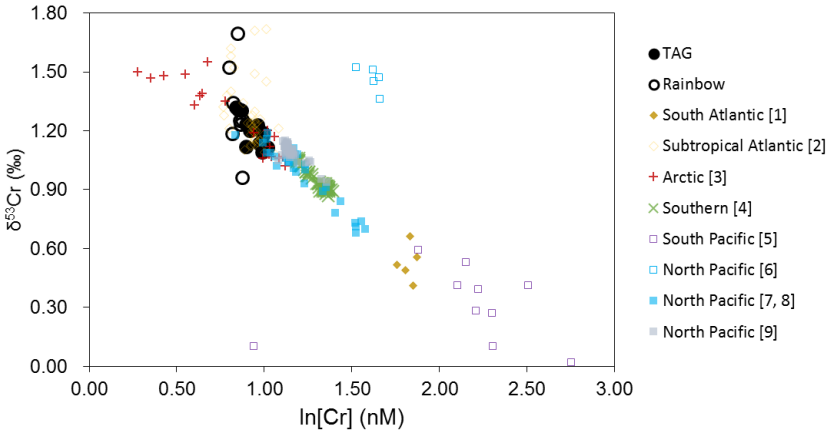

Figure 3-4 Cross plot of δ^{53}Cr values versus logarithmic Cr concentration, for new data from this study together with seawater data from the literature ([1] *Bonnand et al., 2013;* [2] *Goring-Harford et al., 2018;* [3] *Scheiderich et al., 2015;* [4] *Rickli et al., 2019;* [5] *Bruggmann et al., 2019;* [6] *X Wang et al., 2019;* [7] *Moos and Boyle 2019;* [8] *Moos et al., 2020;* [9] *Janssen et al., 2020*).

3.5.3 Evolution of the hydrothermal δ^{56}Fe signal in the distal plume

As the hydrothermal plumes are dispersed and further diluted, dFe concentrations decrease and δ^{56}dFe evolves to higher values (Figure 3.5). The δ^{56}Fe of dFe in the particle plumes cannot, however, be fully explained by conservative mixing between the least dilute plume samples (dFe_{plume} = 55.2 nM and 53.1 nM, $\delta^{56}dFe_{plume}$ = –1.83‰ and –6.95‰ at TAG and Rainbow, respectively) and

background seawater (dFe_{SW} = 0.48 nM, $\delta^{56}dFe_{SW}$ = 0.69‰; *Conway and John, 2014*) (solid curves on Figure 3.5):

$$dFe = dFe_{plume}/[\text{Plume dilution factor}] + dFe_{sw} \quad (3\text{-}12)$$

$$\delta^{56}dFe = \frac{dFe_{plume} \times \delta^{56}dFe_{plume}/[\text{Plume dilution factor}] + dFe_{sw} \times \delta^{56}dFe_{sw}}{dFe_{plume}/[\text{Plume dilution factor}] + dFe_{sw}} \quad (3\text{-}13)$$

Insight as to the processes that control the evolution of the hydrothermal δ^{56}Fe signal during dispersal can be revealed by the Fe incubation experiments that were carried out on the hydrothermal plume samples (*Mellett et al., in prep.*).

The δ^{56}dFe values of the first subsamples from the unfiltered treatment (collected ~3 h after retrieving the Niskin bottles) were 0.58‰ for TAG and 0.76‰ for Rainbow, significantly higher than measured from the filtered treatment (Figure 3.5 and Table 3.2). The dFe concentrations were also higher. This implies that Fe must have been added to the dissolved Fe pool, most likely through dissolution of particulate Fe-(oxyhydr)oxides that are predicted to be isotopically heavy. Analyses of hydrothermal particles by *Revels et al. (2015)* and *Severmann et al. (2004)* showed that δ^{56}Fe values of particulate Fe were ~0.20‰ in the TAG plume and in the range of 0.24-1.29‰ (average ~0.90‰) in the Rainbow buoyant plume, consistent with partial oxidation of Fe(II) and precipitation of the Fe(III) that formed. Abiotic dissolution of FeOOH particles is reported to be small (< 0.1‰; *Skulan et al., 2002*). Thus the results of the incubation experiment utilizing the unfiltered samples suggest that continuous exchange of Fe between the particulate and dissolved fractions plays an important role in determining the evolution of hydrothermal δ^{56}Fe in the distal plume.

The δ^{56}Fe values of dissolved Fe from the filtered treatment, on average −1.37‰ for the TAG incubation and −7.31‰ for Rainbow, are consistent with the seawater profile measurements. The δ^{56}dFe values remained relatively constant over a time period of 5 days, even though dFe concentrations decreased from 75 nM to 21 nM and from 280 nM to 47 nM in the TAG and Rainbow experiments respectively (Table 3.2). The isotopically light δ^{56}Fe could be explained by partial oxidation of Fe(II) and removal of some part of the Fe(III) that forms; however, this process can be expected to modify δ^{56}Fe. Rather, the data suggest that dFe in the dispersing plume is in a stabilised form that is resistant to oxidation. Stabilisation of dFe is likely mediated by organic ligands (e.g. *Toner et al., 2009*) that are sourced from the vent fields themselves or from ambient seawater. In this case, removal of Fe from the dissolved fraction through time would be consistent with sluggish coagulation of ligand-bound Fe and/or colloidal FeOOH; precipitation of Fe during estuarine mixing, which is an analogous process, has been shown to not fractionate Fe isotopes to any great extent (*Escoube et al., 2009; Zhang et al., 2015*).

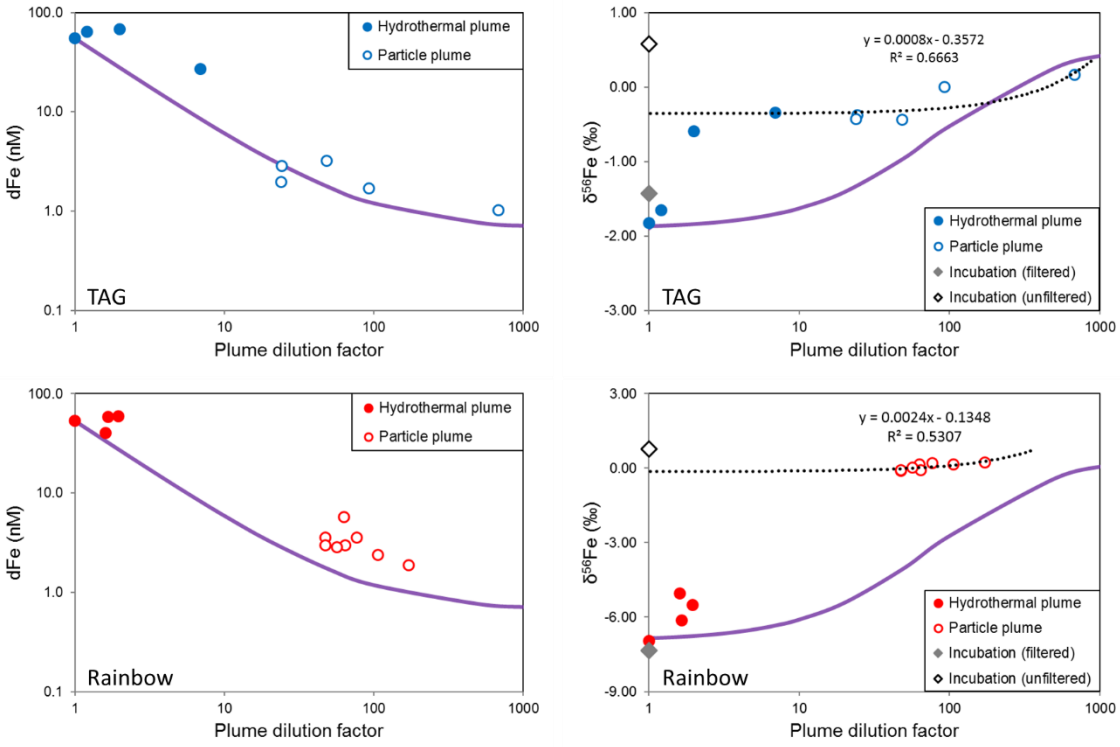

Figure 3-5 Evolution of dFe and δ^{56}dFe during hydrothermal plume dispersal. The filled circles represent samples from the hydrothermal plume (at Stations 35 and 16) and open circles represent the particle-rich plumes (at Stations 36, 18 and 12). The diamond symbols represent samples at the initial time point from the Fe incubation experiments. Plume dilution factor is calculated based on the Mn concentration (Section 3.3.5), Mn concentrations of the least dilute hydrothermal plume samples are 41 nM (TAG) and 297 nM (Rainbow). Purple curves show conservative mixing (Section 3.5.3) between the least dilute hydrothermal plume sample (dFe_{plume} = 55.2 nM and 53.1 nM, $\delta^{56}dFe_{plume}$ = –1.83‰ and –6.95‰ at TAG and Rainbow, respectively) and background seawater (CLSW, dFe_{SW} = 0.48 nM, $\delta^{56}dFe_{SW}$ = 0.69‰). The dotted lines show the linear regression for samples from the particle plume.

The δ^{56}dFe of the particle rich plume samples was as low as −0.44‰ to −0.38‰ at 3300-3400 m water depth at North of TAG (Station 36), and −0.11‰ to −0.08‰ at 2100 m depth at North and East of Rainbow (Stations 18 and 12). The higher δ^{56}dFe value in the Rainbow distal plume is most likely a result of dissolution of Fe-(oxyhydr)oxides, as discussed above. The dissolved Fe fraction consists principally of colloidal Fe in these samples (*Lough et al., in prep.*), up to 77% at TAG (Station 36) and up to 87% at Rainbow (Station 18). Assuming that colloidal Fe is composed of Fe-(oxyhydr)oxides that have δ^{56}Fe values of 0.20‰ to 0.90‰ (*Revels et al., 2015; Severmann et al., 2004*), then mass balance calculations indicate that the δ^{56}Fe signal of soluble Fe would be ~ −2.32‰ and at TAG and ~ −6.90‰ at Rainbow (Table 3.4), close to the lowest values (respectively, −1.91‰ and −6.95‰) measured in the near-field plumes. These results support the idea that in the distal hydrothermal plume, the isotopically light hydrothermal δ^{56}Fe signal is stabilised in the soluble Fe

fraction, while a fraction of the particulate Fe-(oxyhydr)oxides is added to the colloidal Fe pool as plume disperses away from the vent site.

Table 3-4 Results of the isotope mass balance calculation for the distal particle-rich plume sample (see Section 3.5.3 for details). Fe concentrations (dFe and sFe) are derived from FIA-CL measurements (data courtesy of *Lough et al., in prep*), and the cFe concentration is given by the difference between the dFe and sFe concentrations.

CTD no.	ROS no.	Depth (m)	δ^{56}dFe	cFe (nM)	sFe (nM)	δ^{56}Fe of cFe Hypothesized	δ^{56}Fe of sFe Calculated
TAG Close North (Station 36)							
80	7	3299	−0.38‰	1.71	0.51	0.20‰	−2.32‰
Rainbow Close North (Station 18)							
40	6	2099	−0.08‰	5.15	0.74	0.90‰	−6.90‰

3.5.4 Quantifying the hydrothermal contribution to the Fe inventory in the North Atlantic

Previous studies have shown that atmospheric dust, benthic sedimentary inputs and hydrothermal vent fluids can all be important sources of dFe in the North Atlantic Ocean (*Conway and John, 2014*). Input of Fe from dust deposition is evidenced from the TAG dFe profiles (Figure 3.6a) by elevated concentrations of dissolved Fe in the surface mixed layer (0-120 m); this dFe is characterised by a relatively high δ^{56}dFe value (0.22-0.67‰). The δ^{56}Fe value of aerosols, sourced from the Sahara desert that have been sampled over the North Atlantic, was 0.09-0.12‰ (*Conway et al., 2019*), close to the crustal value. However, dissolution of the aerosol dust in seawater mediated by Fe-binding ligands, such as siderophores, appears to result in an isotopically heavier dissolved Fe pool (*Basu et al, 2019; Dideriksen et al., 2008*). Here data from the TAG and close to TAG stations are consistent with dust dissolution, as δ^{56}Fe values of dFe increase (0.22‰ to 0.67‰; Figure 3.6a) with increasing dFe concentrations (0.66 to 0.88 nM); these δ^{56}dFe values are consistent with those measured in the surface mixed layer sampled as part of the GEOTRACES North Atlantic GA03 transect (0.3‰ to 0.7‰; *Conway and John, 2014*). The sample at 100 m depth at the TAG station (within the surface mixed layer) has dFe as high as 0.88 nM and δ^{56}dFe up to 0.67‰, which is assumed to represent the dust end-member in this study.

Seawater samples taken from above the seafloor and below the hydrothermal plume at the TAG and the Rainbow vent sites have lower dFe concentrations (1.52-2.31 nM) and higher δ^{56}dFe (0.47‰ and 0.36-0.38‰ respectively) compared to those in the plume, more consistent with the dFe concentration and δ^{56}dFe value of background seawater (CLSW dFe ~0.48 nM, δ^{56}dFe ~0.69‰; *Conway and John, 2014*). Based on water column measurements, *Conway and John (2014)*

determined that benthic sedimentary sources of dFe in the North Atlantic had δ^{56}Fe = 0 to 0.22‰; such values indicate input of Fe from dissolution of oxygenated sediments (*Beard et al., 2003; Homoky et al, 2013*), or resuspension of porewater colloids (*Homoky et al., 2009*). At stations that were close to but not directly above vent fields, seawater samples taken from as close to the seafloor as possible had δ^{56}dFe values of ~0‰ (Figure 3.6b). This would be consistent with either input of Fe from oxic sediments, or dissolution of particles falling out of the hydrothermal plume. The lack of any obvious signature of benthic sedimentary Fe inputs at plume sites suggests that any input is masked inputs of isotopically light Fe from hydrothermal fluids.

As discussed above, hydrothermal Fe isotope signal is modified in the hydrothermal plume, so the δ^{56}dFe signature of hydrothermal Fe to the ocean interior will not be the same as the δ^{56}Fe signature of the hydrothermal fluid. Thus, the δ^{56}dFe value of 'stabilised' hydrothermal Fe delivered to the interior ocean is estimated by extrapolating the δ^{56}dFe value of seawater from within the distal particle plumes at the stations close to TAG and Rainbow, back to the above-axis plume as shown in Figure 3.5. In this way, the δ^{56}Fe value of hydrothermal Fe is estimated to be −0.36‰ for TAG, and −0.13‰ for Rainbow. These estimated δ^{56}dFe values are very similar to those measured in the core of the particle plume (−0.44‰ to −0.38‰ for TAG and −0.11‰ to −0.08‰ for Rainbow), and reflect potential stabilisation of hydrothermal Fe in the soluble pool along with exchange of Fe between particulate and colloidal fractions (Section 3.5.3).

The effects of biogeochemical cycling on Fe isotope distributions can be assessed via the relationship between δ^{56}dFe and apparent oxygen utilisation (AOU) from below the surface mixed layer to intermediate water depths (Figure 3.6c). AOU reflects remineralisation of sinking organic material within the water column. At the stations close to Rainbow and to the east of Rainbow, dFe concentrations and δ^{56}dFe values increase with increasing AOU, meaning that remineralisation of Fe releases relatively heavy isotopes back into the dissolved fraction, consistent with other studies in the North Atlantic Ocean (*Conway and John, 2014; Klar et al., 2018*). By contrast, studies in the south-west Pacific and the Southern Ocean have reported that light Fe isotopes are preferentially taken up by phytoplankton in surface waters (*Ellwood et al. 2015, 2020*), with release of this isotopically light Fe at intermediate depths via remineralisation (*Abadie et al. 2017*). The differences in the effects of biogeochemical processes on Fe isotopes potentially reflects differences in phytoplankton communities or different iron acquisition strategies between the dust-rich Atlantic and the iron-poor Southern Ocean (e.g. *Strzepek et al., 2011; Rubin et al., 2011*), although further investigations are required to confirm this.

The Fe inputs to the North Atlantic Ocean can be modelled using a multi-component mixing model (*Conway and John, 2014*). However, as the sedimentary Fe input to the upper water column is likely

minimal at these sampling sites, and biogeochemical cycling of Fe can be compensated by depth-averaging δ^{56}dFe, a more simple two-component isotope mixing model considering the dust versus hydrothermal inputs can be used:

$$\delta^{56}\mathrm{dFe} = f_{\mathrm{dust}} \times \delta^{56}\mathrm{Fe}_{\mathrm{dust}} + f_{\mathrm{hydrothermal}} \times \delta^{56}\mathrm{Fe}_{\mathrm{hydrothermal}} \quad (3\text{-}14)$$

The δ^{56}dFe values are integrated over the depths below the surface mixed layer and above the hydrothermal plume (120-3000 m for the TAG stations, and 100-1800 m for Rainbow). Model results (Table 3.5) indicate that dust is the dominant source of Fe, which is consistent with a previous study in the North Atlantic (*Conway and John, 2014*). However, it is shown that hydrothermal activity could contribute ~18-35% of the dFe in the upper water column around the TAG stations (up to 250 km away from the vent site), and ~19-58% around Rainbow (up to 200 km away from the vent site). The higher vent fluid Fe content, and the relatively shallow depth and rough topography (*Severmann et al., 2004*) at Rainbow compared to TAG means that the hydrothermal vent fluids exert a larger impact on the oceanic Fe inventory. This is consistent with modelling studies that have shown that enhanced internal tides drive diapycnal mixing over the Mid-Atlantic Ridge, especially close to the Azores (*Tuerena et al., 2019*). In addition to these physical controls, the persistence of hydrothermal Fe can also be supported by exchange between the dissolved and particulate fractions, most likely through dissolution of the Fe-(oxyhydr)oxide particles that remain in the distal plume (Section 3.5.3). This mechanism is similar to the previously hypothesised reversible dissolved-particulate exchange that accounts for the long-distance transport of hydrothermal Fe in the southern East Pacific Rise plume (*Fitzsimmons et al., 2017*).

Table 3-5 Quantification of the importance of hydrothermal source to the dissolved Fe inventory using two-component isotope mixing model (Section 3.5.4). Integrated water depths are 120-3000 m for the TAG stations and 100-1800 m for the Rainbow stations.

Stations	**TAG**	**North of TAG**	**West of TAG**	**250 km West of TAG**
	Dust end-member δ^{56}Fe = 0.67‰; hydrothermal end-member δ^{56}Fe = −0.36‰			
Column integrated δ^{56}Fe (‰)	0.48	0.45	0.31	0.42
% hydrothermal contribution	18	21	35	24
Stations	**Rainbow**	**North of Rainbow**	**East of Rainbow**	**200 km East of Rainbow**
	Dust end-member δ^{56}Fe = 0.67‰; hydrothermal end-member δ^{56}Fe = −0.13‰			
Column integrated δ^{56}Fe (‰)	0.52	0.39	0.35	0.21
% hydrothermal contribution	19	35	40	58

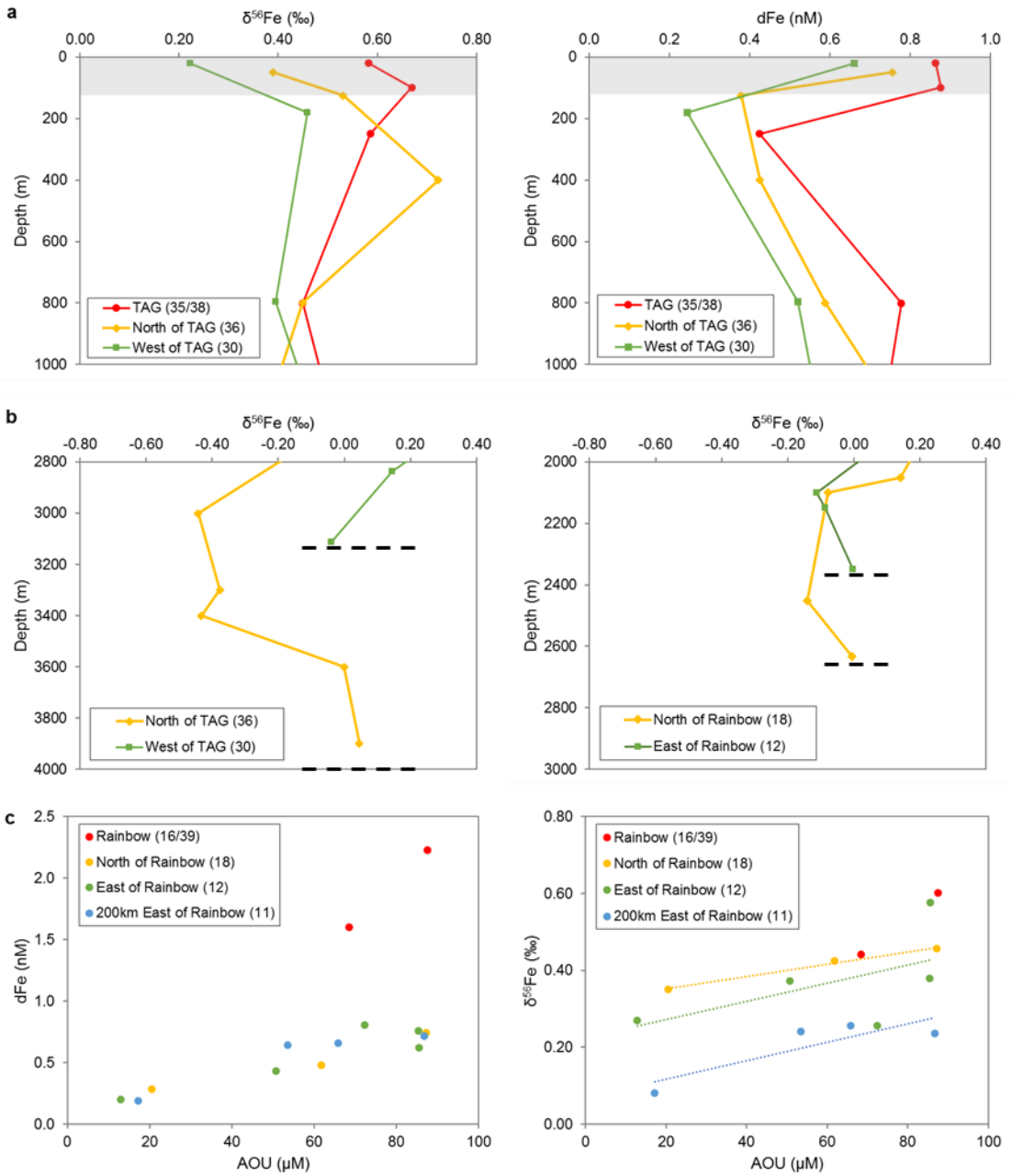

Figure 3-6 (a) dFe concentration and δ^{56}dFe value in the upper 1000 m of the water column for stations around TAG where isotopically heavy δ^{56}Fe in the surface mixed layer (0-120 m, highlighted) due to dust deposition was observed. **(b)** δ^{56}dFe value in the deep layer from stations close to TAG and Rainbow, showing the potential influence of sedimentary Fe input and/or particle plume dispersal; horizontal dashed lines indicate depths of seafloor. **(c)** dFe concentration and δ^{56}dFe value relative to apparent oxygen utilisation (AOU) from stations around Rainbow; dotted lines are the linear regression of δ^{56}dFe and AOU at each station. Numbers in brackets represent station numbers.

3.5.5 Constraining the effect of hydrothermal activity on the oceanic Cr budget

Figure 3.2 provides clear evidence that Cr is removed from seawater in the hydrothermal plume, implying that hydrothermal activity is likely a sink, rather than a source, of Cr in the ocean. The Cr isotope data suggest that removal of Cr occurs via reduction of Cr(VI), with Fe(II) as the electron donor, with scavenging of Cr(III) onto the surface of the Fe(III)-(oxyhydr)oxides that form. Cr(VI) reduction via Fe(II) is rapid, with a half-life of minutes to hours (*Sedlak and Chan, 1997*), much shorter than the estimated half-life of Fe-oxyhydr(oxide) particles in the plume (~41 days at TAG; *Rudnicki and Elderfield, 1993*).

The size of the hydrothermal Cr sink can be estimated from the Cr deficit in the plume in two ways. Firstly, assuming given that removal of Cr is linked to the formation of Fe(IIII) (oxyhydr)oxides, then the hydrothermal Cr sink is related to the particulate Fe (pFe) content of the hydrothermal plume, estimated as follows:

$$pFe = ([Fe]_{VF} / [\text{VF dilution factor}]) - [dFe]_{meas} - [Fe]_{sulfide} \quad (3\text{-}15)$$

where [Fe]sulfide is the quantity of Fe that precipitated as Fe-sulfide (~20% at TAG and ~7% at Rainbow; Section 3.5.1). The particulate Cr (pCr) content can be estimated from the dissolved Cr deficit relative to ambient seawater (Cr deficit = 0.01 – 0.25 nM, Section 3.5.2). In this way, the mean molar Cr/Fe ratios of the plume particles are estimated to be ~3.3×10^{-4} and ~8×10^{-5} for TAG and Rainbow, respectively. The estimated Cr/Fe ratio for the TAG particles is of the same magnitude as that reported for other studies at TAG (3.6-4.8 × 10^{-4}, *Trocine and Trefry 1988; German et al., 1991*), and also with particles sampled from the southern East Pacific Rise (9 × 10^{-4}, *Feely et al., 1996*).

Based on the vent fluid Fe content, and considering that a fraction of this Fe (~20% at TAG and ~7% at Rainbow; Section 3.5.1) is precipitated as Fe-sulfide during the early stages of mixing, the maximum amount of Fe available for Fe-(oxyhydr)oxide formation in the hydrothermal plume is estimated to be ~4 mmol/kg and ~22 mmol/kg at TAG and Rainbow, respectively. Using the particulate Cr/Fe ratios calculated above, and given that the water flux through the global high-temperature hydrothermal system is ~2.62×10^{13} kg/yr (*Elderfield and Schultz, 1996; Reinhard et al., 2013*), the global removal flux of seawater Cr in the hydrothermal plume is calculated to be ~3.4 × 10^{7} to 4.6 × 10^{7} mol/yr (Table 3.6).

Secondly, the hydrothermal removal flux of Cr can be estimated from the Cr deficit in the plume (~0.01 to 0.25 nM) and the estimated volume of the oceans that passes through the hydrothermal plume each year (~4.85×10^{17} L/yr, based on measured fluxes of ^{3}He from Endeavour ridge: *Kadko,*

1993; Rosenberg, 1988). This method yields a removal flux of ~0.5 - 12 × 10^7 mol/yr, which is comparable to the flux calculation above.

Table 3-6 Quantification of the global high-temperature hydrothermal removal flux of Cr based on data from TAG and Rainbow vent fields respectively, and comparison with river input flux of Cr (Section 3.5.5).

Method 1		High-temperature hydrothermal system			Comparison with river input	
Vent field	pCr/pFe estimated	Available FeOOH (mmol/kg)	Hydrothermal water flux (kg/yr) [a]	Cr removal flux (mol/yr)	River flux (mol/yr)	% of river flux
TAG	3.3 × 10^{-4}	4	2.62 × 10^{13}	3.4 × 10^7	5.6 × 10^8	6
Rainbow	8 × 10^{-5}	22		4.6 × 10^7		8
Method 2		High-temperature hydrothermal system			Comparison with river input	
Vent field	Cr deficit (nM)		Water flux through plume (L/yr) [b]	Cr removal flux (mol/yr)	River flux (mol/yr)	% of river flux
TAG	0.02 - 0.11		4.85 × 10^{17}	1-5.3 × 10^7	5.6 × 10^8	2-9
Rainbow	0.01 - 0.25			0.5-12 × 10^7		1-20

[a] Taken from *Elderfield and Schultz (1996)*
[b] Taken from *Kadko (1993); Rosenberg (1988)*

The estimated hydrothermal removal flux for Cr calculated here is consistent with earlier work at TAG (4.8 × 10^7 mol/yr; *Rudnicki and Elderfield, 1993)*, but significantly higher than that estimated by *Reinhard et al. (2013)* (0.01 × 10^7 mol/yr). The latter study simply asserted that Cr was stripped from seawater circulating in the high temperature part of the hydrothermal reaction cell, and neglected to consider removal of Cr from seawater in the hydrothermal plume. This chapter provides strong evidence for Cr(VI) reduction in the hydrothermal plume linked to Fe(II) oxidation and the subsequent scavenging of Cr into Fe(III) (oxyhydr)oxide particles that renders the hydrothermal plume from high-temperature hydrothermal systems a sink of seawater Cr (Figure 3.7). Compared to the riverine input of Cr, the principal source of Cr to the oceans (~5.6 × 10^8 mol/yr: *Bonnand et al., 2013*), the hydrothermal removal flux of Cr is relatively small (1-20% of the riverine flux) but non-negligible.

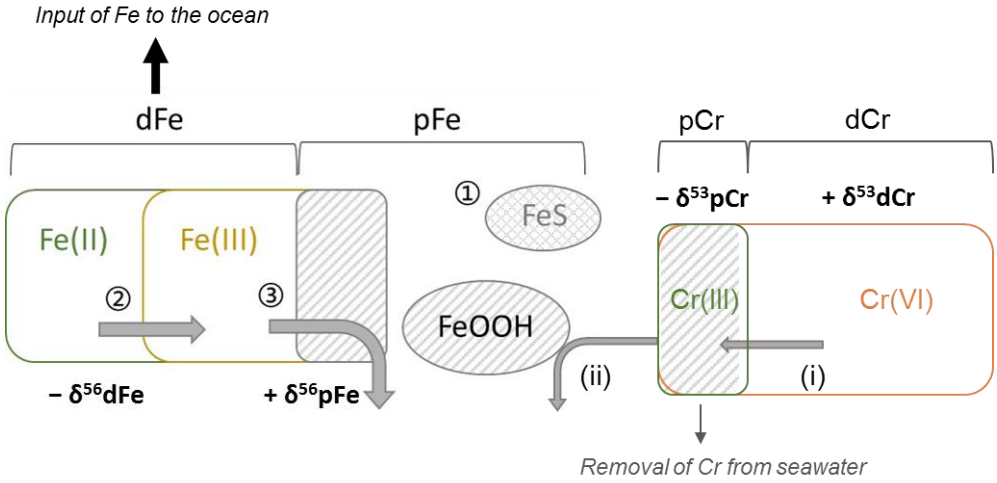

Figure 3-7 Schematic showing the coupled cycling of Fe and Cr in the hydrothermal plume. ① Precipitation of Fe-sulfide; ② Oxidation of Fe(II) to Fe(III); ③ Precipitation of Fe(III) as Fe-(oxyhydr)oxide. (i) Reduction of Cr(VI) to Cr(III); (ii) Scavenging of Cr(III) onto Fe-(oxyhydr)oxide particles.

3.6 Conclusions

This study investigated how chemical processes in the hydrothermal plume regulate the hydrothermal input of Fe and Cr by utilising a novel stable isotope approach. For the first time, it is shown that Fe and Cr isotope profiles through the hydrothermal plume are the 'mirror image' of one another, providing compelling evidence for coupled Fe(II) oxidation and Cr(VI) reduction in the hydrothermal plume. Oxidation of Fe(II) and precipitation of Fe-(oxyhydr)oxides accounts for the low δ^{56}Fe values of dissolved Fe, as low as −1.91‰ at TAG and −6.95‰ at Rainbow. Differences in δ^{56}Fe values between the two sites likely reflect differences in the proportion of dissolved Fe that precipitates as Fe-sulfide versus Fe-(oxyhydr)oxide. Cr reduction is suggested by elevated δ^{53}Cr values in the TAG and Rainbow hydrothermal plumes compared to background seawater, by up to +0.13‰ and +0.60‰ respectively. Anomalously high δ^{53}Cr values measured at the Rainbow site yield a Cr isotope fractionation factor ($\delta^{53}Cr_{Cr(III)} - \delta^{53}Cr_{Cr(VI)}$) of −4.6‰, significantly greater than that calculated for the 'global correlation' between Cr concentration and δ^{53}Cr in seawater.

The δ^{56}Fe of dissolved Fe evolves to heavier values (−0.44 to 0.23‰) in distal part of the hydrothermal plume, likely controlled by exchange of Fe between the dissolved and particulate fraction as well as mixing with background seawater. The δ^{56}Fe signature of dFe can be used to distinguish Fe inputs from dust and hydrothermal activity; these data suggest that hydrothermal venting potentially contributes ~18-58% of dissolved Fe to the oceanic inventory, at distances of up to 250 km away from the vent sites. In contrast, reduction of Cr and scavenging by Fe-(oxyhydr)oxide particles in the hydrothermal plume means that high-temperature hydrothermal

systems are a sink for seawater Cr, potentially removing up to 20% of the riverine flux. Thus processes in hydrothermal plumes have the potential to significantly modify the Fe and Cr isotopic signatures of hydrothermal fluids.

Chapter 4 Biogeochemical cycling of chromium and chromium isotopes in the sub-tropical North Atlantic Ocean

4.1 Introduction

Chromium (Cr) is a transition metal, present in typical concentrations of 0.9 to 6.5 nM in seawater (*Campbell and Yeats, 1981; Cranston, 1983; Jeandel and Minster, 1984; Achterberg and van den Berg, 1997; Sirinawin et al., 2000; Connelly et al., 2006; Bonnard et al., 2013; Scheiderich et al., 2015*) and has a relatively long residence time of ~3000 to 40000 years (*Campbell and Yeats, 1984; Reinhard et al., 2013; McClain and Maher, 2016*). In some parts of the oceans, concentrations of dissolved Cr are modestly depleted in the surface layer, and Cr has been classified as intermediate between a 'conservative' and 'recycled' element (*Jeandel and Minster, 1987; Sirinawin et al., 2000*). In oxic seawater, Cr(VI) is predicted to be the thermodynamically stable form of Cr (*Elderfield, 1970*), whereas under oxygen deficient conditions, Cr(III) may be the dominant Cr species (*Murray et al, 1983; Rue et al., 1997*). However, it has recently been shown that oxygen is not the sole control on Cr speciation (*Goring-Harford et al., 2018; Wang et al., 2019; Janssen et al., 2020*). High levels of biological productivity, as well as the presence of Fe(II) and organic matter in surface waters, can also facilitate Cr reduction (*Connelly et al., 2006; Døssing et al., 2011; Kitchen et al., 2012*). Cr(VI) is highly soluble as the chromate (CrO_4^{2-}) ion in oxic seawater, whilst Cr(III) is particle-reactive and readily adsorbed onto solid surfaces (*Rai et al., 1987; Ellis et al., 2002*).

Rivers are the main source of dissolved Cr to the ocean (*Bonnand et al., 2013; Reinhard et al., 2013*). Chromium is mainly in the form of Cr(III) in rocks, but weathering reactions driven by Mn-oxides oxidise Cr(III) as it is released from silicate rocks (*Frei et al., 2009*), so principally Cr(VI) is delivered to the oceans via rivers *(Cranston and Murray, 1980)*. Atmospheric deposition is a major source of many trace metals to the ocean and may result in elevated concentrations of Cr in surface seawater in some parts of the oceans (*Achterberg and van den Berg, 1997*). As yet, to my knowledge, there are no published reports of the Cr content of high temperature hydrothermal vent fluids, but low temperature (diffuse) hydrothermal fluids from the North Fiji Basin are slightly enriched in total Cr (~48 nM) compared to background seawater (*Sander and Koschinsky, 2000*). However, analyses of hydrothermal plume particles indicates that they have higher Cr/Fe ratios than predicted by mixing of vent fluids and seawater, suggesting that hydrothermal activity may be a net sink of Cr as it is scavenged from seawater onto Fe-(oxyhydr)oxides (*Trocine and Trefry, 1988; German et al., 1991;*

Rudnicki and Elderfield, 1993; Feely et al., 1996; Bauer et al., 2019). Cr is removed from the oceanic inventory through reduction of Cr(VI), scavenging onto settling particles and burial as Cr(III) in reducing and/or anoxic sediments (*Reinhard et al., 2014; Gueguen et al., 2016*). Therefore, marine sediments are considered as the major sink for seawater Cr. The estimated fluxes of Cr inputs to, and outputs from, the ocean reported in the literature are summarised in Table 4.1.

Table 4-1 Range of concentrations and fluxes of Cr inputs and outputs to/from the ocean.

Reservoir	Cr (nM)	Cr (μmol/g)	Flux Cr (mol/yr)	Source
Inputs				
Rivers	15-150		$5.6\text{-}17 \times 10^8$	*Bonnand et al. (2013); McClain and Maher (2016)*
Low-temperature hydrothermal vents	~48		3.4×10^6	*Sander and Koschinsky (2000); Reinhard et al. (2013)*
Outputs				
High-temperature hydrothermal vents		–	$3.4\text{-}4.6 \times 10^7$	*Chapter 3*
Oxic sediment sink		~2	5.8×10^7	*Chester and Hughes (1969); Reinhard et al. (2013)*
Sub-oxic and anoxic sediment sink		~2	5.2×10^8	*Gueguen et al. (2016); Reinhard et al. (2013)*

Stable chromium isotope ratios are expressed in delta notation relative to NBS979 standard, as

$$\delta^{53}Cr = [(^{53}Cr/^{52}Cr)_{sample}/(^{53}Cr/^{52}Cr)_{NBS979} - 1] \times 1000) \quad (4\text{-}1)$$

Silicate rocks have very similar $\delta^{53}Cr$ values, around −0.12 ± 0.10‰ (*Schoenberg et al., 2008*). Groundwaters with low levels of oxygen are relatively enriched in heavy Cr isotopes ($\delta^{53}Cr$ = 0.3 to 5.8‰: *Ellis et al., 2002; Izbicki et al., 2008*), which is mainly governed by shifts in Cr redox state. Theoretical studies and laboratory experiments have shown that reduction of Cr(VI) leads to large mass-dependent fractionation, with enrichment of light Cr isotopes in the Cr(III) that forms (*Ellis et al., 2002; Døssing et al., 2011; Kitchen et al., 2012; Basu and Johnson, 2012*). The direction of fractionation holds regardless of the reductant (Fe(II), Fe(II)-bearing minerals, organic matter), while the kinetic fractionation factors are variable ($\delta^{53}Cr(III) - \delta^{53}Cr(VI)$ = −1.5 to −4.2‰). Reduction of Cr(VI) to Cr(III) may not be quantitative even under anoxic conditions in seawater and there appears to be an offset between the $\delta^{53}Cr$ values of Cr(III) and Cr(VI) (*Wang et al., 2019; Janssen et al., 2020*). However, to date, there are few studies of the Cr isotopic composition of single Cr species; this would be a productive area of future research.

The $\delta^{53}Cr$ signature of seawater from open ocean settings measured to date is in the range between 0.1 and 1.7‰ (*Bonnand et al., 2013; Goring-Harford et al. 2018; Scheiderich et al., 2015; Rickli et al., 2019; Bruggmann et al., 2019; Wang et al., 2019; Moos and Boyle, 2019; Moos et al., 2020; Janssen et al., 2020*), but the average value (1.04 ± 0.26‰, n = 217) is higher than that of the average river input (0.49 ± 0.45‰, n = 49: *Frei et al., 2014; Paulukat et al., 2015; D'Arcy; 2016; Wu et al., 2017; Andronikov et al., 2019*). This suggests that the Cr isotopic signature of seawater is modified by (i) input of Cr from other sources, such as sediments, (ii) fractionation of Cr as it is removed from seawater (for example, by reduction of Cr(VI) on the surface of particles that scavenge the Cr(III) that forms), and/or biogeochemical cycling. *Scheiderich et al. (2015)* showed that the $\delta^{53}Cr$ composition of waters in the Arctic Ocean was highly heterogeneous (0.99 to 1.55‰), and hypothesised that this can be attributed to Cr reduction and scavenging in surface waters and oxygen minimum zones, with subsequent release of Cr from sinking particles in deeper waters. These processes were used to explain the reverse correlation between $\delta^{53}Cr$ value and logarithmic Cr concentration in the global ocean, from which they derived an isotope fractionation factor between Cr(III) and Cr(VI) of ~ –0.8‰ (*Scheiderich et al., 2015*). More recent studies of the Cr isotopic composition of seawater from the North Pacific and the Southern Ocean (*Moos and Boyle, 2019; Rickli et al., 2019; Janssen et al., 2020; Moos et al., 2020*) also support this 'global correlation'. However, as yet, the underlying mechanisms that produce this apparent correlation are poorly constrained.

This chapter reports total dissolved Cr concentrations and total dissolved Cr isotope compositions ($\delta^{53}Cr$) for full-depth water column profiles for three stations from a GEOTRACES transect along the 22°N sub-tropical Atlantic Ocean (Figure 4.1a). This fills an important knowledge gap, because few full-depth water column profiles of Cr isotopes are available for the open ocean, together with ancillary data (nutrient and oxygen concentrations, concentrations of other trace metals, salinity, temperature, etc) that aid the interpretation of Cr behaviour. These data provide insight into the potential sources of Cr to the North Atlantic Ocean as well as the effects of internal cycling processes.

4.2 Materials and methods

4.2.1 Sample collection and oceanographic setting

Samples for this study were collected from Stations 1, 4, and 6 (Figure 4.1a) during RRS *James Cook* cruise JC150 (UK GEOTRACES $GA_{pr}04$ process cruise) between 26th of June and 12th of August 2017. The water depths for the three stations were 5408 m, 3505 m and 5810 m respectively.

Seawater was collected using pre-cleaned 10 L Ocean Test Equipment (OTE) water sampling bottles that were mounted on a titanium rosette system and deployed from a Kevlar wire. On recovery, the OTE bottles were transferred into a trace metal clean container for sub-sampling. Seawater was filtered through a Sartobran 300 (Sartorius) filter capsule (0.2 µm) or a polyethersulfone filter (PES, Supor, Pall Gelman, 0.2 µm) under gentle pressure, and was collected into acid-cleaned low density polyethylene (LDPE) bottles. Filtered seawater samples were acidified with UpA-grade hydrochloric acid (HCl, Romil) to 0.024 M, and were stored for at least a year before the Cr isotope analysis, allowing complete conversion of Cr species to Cr (III) (*Semeniuk et al., 2016*).

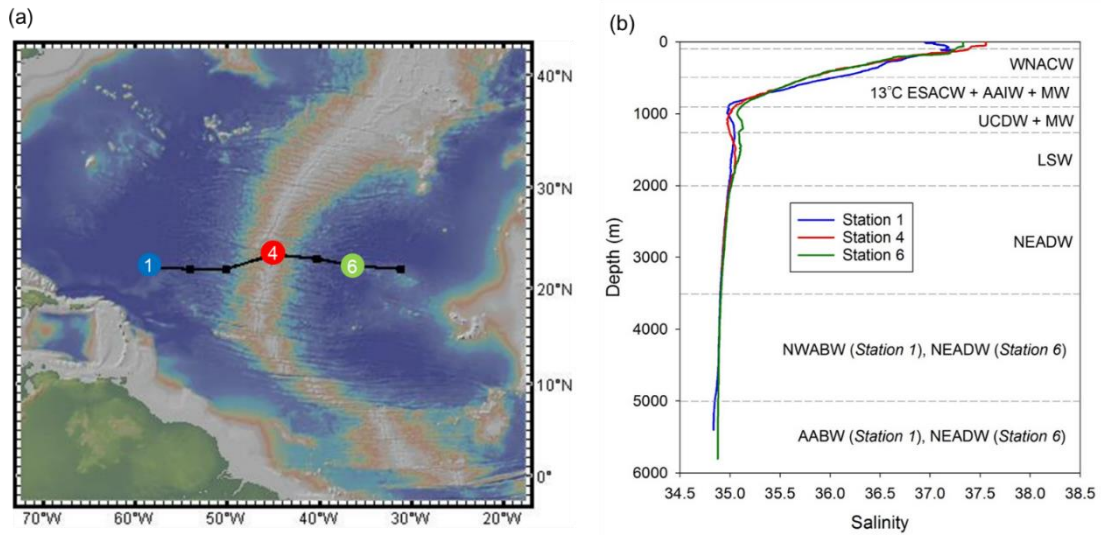

Figure 4-1 (a) Locations of sampling stations (1, 4 and 6) in the sub-tropical North Atlantic Ocean. Map courtesy of http://www.geomapapp.org **(b)** Salinity profiles for the three sampling stations. Water masses are delimited with horizontal dashed lines. WNACW = West North Atlantic Central Water, ESACW = East South Atlantic Central Water, AAIW = Antarctic Intermediate Water, MW = Mediterranean Water, UCDW = Upper Circumpolar Deep Water, LSW = Labrador Sea Water, NEADW = North East Atlantic Deep Water, NWABW = North West Atlantic Bottom Water, ABW = Antarctic Bottom Water. Water mass analysis taken from *Artigue et al. (2019)*.

Analyses of the water masses along the transect based on combined hydrographic and nutrient data are reported in *Artigue et al. (2020)* and summarised in Figure 4.1b. Briefly, the subsurface waters (between ~100 and 900 m depth) mainly consisted of West North Atlantic Central Water (WNACW) and 13°C-East South Atlantic Central Water (ESACW). At approximately 700 m water depth, Antarctic Intermediate Water (AAIW) and Mediterranean Water (MW) dominated, respectively, to the west and to the east of the Mid-Atlantic Ridge (MAR). Upper Circumpolar Deep Water (UCDW) was observed at 900-1250 m, below which Labrador Sea Water (LSW) was centered at ~1500 m. North East Atlantic Deep Water (NEADW), which includes a contribution from Iceland-Scotland Overflow Water (ISOW), was found below LSW and was centered at ~2500 m. At Station

1, to the west of the MAR, North West Atlantic Bottom Water (NWABW) was present between 3500 and 5000 m water depth, and depper waters (>5000 m) consisted of Antarctic Bottom Water (ABW). The deep waters at Station 6 were dominated by NEADW.

4.2.2 Cr isotope analysis

All acids used for chemical processing were thermally distilled. Milli-Q (MQ) water was used for diluting and for cleaning. LDPE bottles and Perfluoroalkoxy (PFA) vials were thoroughly cleaned for trace metal purposes. Samples were handled under laminar flow hoods, set within Class 100 clean laboratories at the National Oceanography Centre Southampton.

Dissolved Cr concentrations were initially determined using a newly developed $Mg(OH)_2$ co-precipitation method (*Moos and Boyle et al., 2019; Rickli et al., 2019*). Approximately 50 mL sub-sample was transferred into an acid-cleaned centrifuge tube, weighed, and amended with 10 ng ^{53}Cr single spike. Ammonia solution (SpA-grade, Romil) was then added to the sample until $Mg(OH)_2$ formed. For 50 mL acidified sub-sample (pH ~1.7), ~500 µL concentrated ammonia was required; it is advisable to keep the size of $Mg(OH)_2$ pellet as small as possible to minimize the potential for matrix effects. After centrifugation and removal of the supernatant, the Cr precipitate was re-dissolved in 5 mL of 0.45 M HNO_3. The Cr concentration of the seawater sample was derived by isotope dilution, based on the $^{52}Cr/^{53}Cr$ ratio of the sample/spike mixture measured by inductively coupled plasma mass spectrometry (ICP-MS; Thermo Scientific Element).

The Cr isotope compositions of seawater samples were determined using a method adapted from *Bonnand et al. (2013)*. Samples of 1-2 L volume were amended with a ^{50}Cr-^{54}Cr double spike to achieve optimal target isotope ratios (*Goring-Harford et al., 2018*) and were left to equilibrium for ~24 hrs. The sample pH was then adjusted to pH 8-9 to facilitate precipitation of Cr. A freshly prepared suspended precipitate of Fe(II) hydroxide, made by addition of ammonia to a fresh ammonium Fe(II) sulfate solution, was added to the samples (10 mL L^{-1} seawater), allowing oxidation of the Fe(II) hydroxide and reduction of any remaining Cr(VI). The Fe(III) hydroxide scavenges the Cr(III), resulting in quantitative precipitation of dissolved Cr (*Connelly et al., 2006*).

The precipitate was separated from the solution via vacuum filtration through pre-cleaned PTFE membrane filters (1 µm, Millipore Omnipore), and was subsequently leached from the filters using 6 M HCl before being dried down and taken up in 6 mL of 7 M HCl. The Cr was first separated from the Fe by anion exchange (~2 mL of Bio Rad AG1-X8 resin loaded in a Bio Rad Poly-Prep column). The resin was extensively cleaned with concentrated HNO_3, 0.5 M HCl and concentrated HCl, and was pre-conditioned with 7M HCl. The sample was loaded in 6 mL of 7M HCl on to the resin. The

eluent was collected, dried down and then reconstituted in 6 mL of 0.5 M HCl. The column was cleaned with 0.5 M HCl to remove Fe and stored in 0.5 M HCl.

Any residual salts were removed by cation exchange (2.9 mL of BioRad AG 50W-X12 resin loaded in a 30 mL PFA Savillex column). The resin was cleaned with 10 mL of 8 M HNO_3, 30 mL of 6 M HCL and 30 mL of MQ water, and was pre-conditioned with 12 mL of 0.5 M HCl. The sample was loaded in 6 mL of 0.5 M HCl and the Cr was immediately eluted and collected in a 15 mL Savillex vial. Additional 4 mL of 0.5 M HCl was added to the column and collected. The resin was cleaned with 6M HCl to remove the remaining cations and stored in 0.5 M HCl. The Cr fraction was evaporated to dryness and was treated with 50µL concentrated H_2O_2 and HNO_3, respectively, to oxidise any remaining organic material, before being dried down once again and re-dissolved in 0.45 M HNO_3.

The isotopic composition of Cr was determined by multicollector inductively coupled plasma mass spectrometry (MC-ICP-MS; Thermo Fisher Neptune Plus) at the University of Southampton, using the methods described in *Goring-Harford et al. (2018)*. Purified samples with 50-100 ppb Cr were introduced using an Aridus 3 desolvator and signals from ^{50}Cr, ^{52}Cr, ^{53}Cr, ^{54}Cr and ^{49}Ti, ^{51}V, ^{56}Fe were quantified. Medium resolution setting was used and mass resolution >5000 was achieved. Each analytical sequence for Cr consisted of repeating analyses of the NBS979 standard every three samples. Each sample analysis consisted of 100 individual measurements. Polyatomic interferences were avoided by making measurements on peak shoulders. The typical ion beam size was 0.15-0.24 V ppb^{-1} for ^{52}Cr. The mean signal intensity of a blank solution that was analysed before and after each sample/standard was subtracted.

The raw Cr data were corrected for instrumental mass bias as well as the total procedural blank contribution. The Cr isotope value was obtained using an iterative deconvolution procedure (*Albarède and Beard, 2004*) and is reported in delta notation relative to the NBS979 isotope standard. The Cr blank mainly came from the Fe precipitate and constituted <10% of the total Cr analysed; the $\delta^{53}Cr$ of the ammonium Fe(II) sulphate solution was determined to be –0.16‰, within the error of that measured previously (–0.34 ± 0.32‰; *Goring-Harford et al., 2018*). To account for the instrumental drift that arises over multiple analytical sessions, NBS979 standard and sample measurements were normalised by subtracting the daily average offset of NBS979 standards from the initial isotopic signature, according to *Goring-Harford et al. (2018)*.

The Cr concentration of each sample was determined simultaneously with the isotope ratios using isotope dilution equations, based on the known sample volume and the quantity of added spike. The results were within 10% (with three exceptions) of the concentrations derived from the $Mg(OH)_2$ co-precipitation method.

Analyses of the NBS979 chromium isotope standard gave 0.00 ± 0.05‰ (2SD, n=49). The precision and accuracy of the methods were further assessed through the analysis of the OSIL Atlantic seawater salinity standard, yielding $\delta^{53}Cr$ = 0.93 to 1.00‰ which is consistent with the value reported in the literature (0.96 ± 0.06‰; *Scheiderich et al., 2015*).

4.2.3 Analysis of dissolved Fe concentration and other ancillary analyses

Filtered samples of seawater for analysis of dissolved Fe (dFe) were acidified on board and analysed using flow injection analysis with chemiluminescence detection (FIA-CL) inside a Class 1000 clean laboratory either onboard or at the University of Southampton, as discussed in *Kunde et al., (2019)*. Briefly, 0.013M ultrapure hydrogen peroxide (H_2O_2, Sigma Aldrich) was added to samples 1 hr prior to analysis, and the sample was buffered in-line to pH 3.5 to 4.0 using 0.15 M ammonium acetate (SpA-grade, Romil). Fe (III) was pre-concentrated on the cation exchange resin Toyopearl-AF-Chelate 650 M (Tosohaas). The accuracy of the method was assessed by repeat quantification of dFe in a reference sample (SAFe; *Johnson et al., 2007*). Filtered seawater samples for analysis of soluble Fe (sFe) were additionally filtered in-line through 0.02 µm syringe filters (Anotop, Whatman) before they were acidified. Concentrations of sFe were determined using the same method as dFe; concentrations of colloidal Fe (cFe) were derived from the difference between dFe and sFe.

A Seabird 911 plus conductivity, temperature and depth (CTD) profiler system together with additional sensors was attached to the titanium frame during the seawater sampling. Sensors were cross-calibrated with discrete seawater analyses on board. Salinity was calibrated using an Autosal 8400B salinometer (Guildline). Chlorophyll-*a* (Chl-*a*) was measured by a fluorescence sensor that was calibrated with a fluorimeter (Turner Designs Trilogy). Dissolved oxygen (O_2) was measured by a Seabird SBE43 sensor, calibrated with a photometric automated Winkler titration system. Turbidity was monitored using the WETLabs BBRTD light scattering sensor.

4.3 Results

Profiles for Chl-*a*, O_2 concentration and turbidity at Stations 1, 4 and 6 are shown in Figure 4.2. Overall, there was no significant inter-site variation in these biogeochemical properties. At each station, Chl-*a* peaked at approximately 140 m water depth, with concentrations up to 0.4 µg/L, reflecting enhanced levels of biological activity in the euphotic zone. Oxygen concentrations reached <140 µmol/kg at depths between ~700 and ~900 m. Deeper waters were well oxygenated with O_2 concentrations of >230 µmol/kg below ~2000 m water depth. Levels of turbidity were highest immediately below the surface, which can be attributed to settling particles, and gradually decreased with depth. Relatively high levels of turbidity were also found close to seafloor, which

can be attributed to resuspension of seabed sediments. At Station 4 there is a local increase in turbidity between 3300 and 3500 m water depth that delineates the particle-rich hydrothermal plume above the Snake Pit hydrothermal vent field on the MAR.

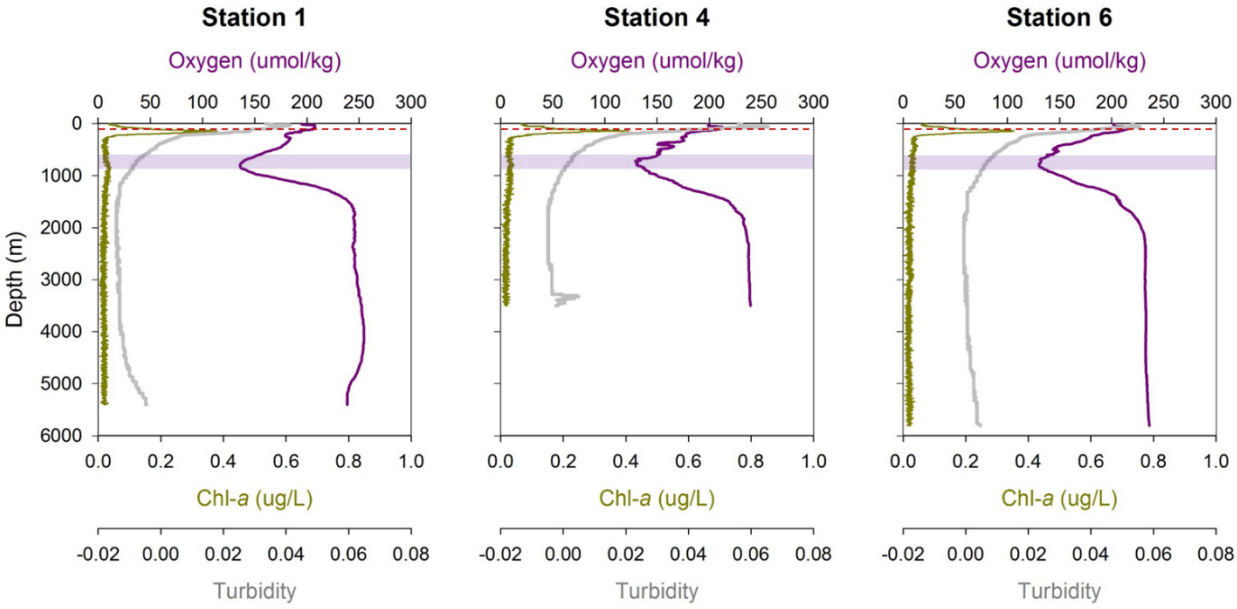

Figure 4-2 Biogeochemical properties (dissolved oxygen, Chl-*a* concentration and turbidity) at Stations 1, 4, and 6. Deep Chl-*a* maximum is marked by the red horizontal dashed lines, and oxygen minimum zone is highlighted by the purple bands.

Full water column depth profiles for dissolved Fe, Cr and δ^{53}Cr at the three stations are shown in Figure 4.3a (data given in Table C1). Concentrations of dissolved Cr ranged between 1.84 and 2.63 nM; the vertical distribution of Cr resembled that of dissolved Fe, notably in the euphotic and mesopelagic zones. Measured δ^{53}Cr values varied from 1.06 to 1.42‰ and the δ^{53}Cr profiles appear to mirror the shape of the Cr concentration profiles. Lowest Cr concentrations (1.84 to 2.04 nM) and highest δ^{53}Cr values (1.36 to 1.42‰) coincided with lowest dFe concentrations (down to ~0.4 nM) between approximately 100 to 400 m water depth. Overall, subsurface waters (between the base of the surface mixed layer and 900 m water depth) were slightly depleted in Cr and slightly enriched in heavy Cr isotopes (average Cr = 2.15 nM, δ^{53}Cr = 1.35‰), relative to deeper waters (average Cr = 2.39 nM, δ^{53}Cr = 1.21‰).

Seawater Cr concentration and δ^{53}Cr values measured in this study are generally consistent with those reported in the eastern sub-tropical Atlantic (Cr = 2.1 to 2.9 nM, δ^{53}Cr = 1.08 to 1.72‰; *Goring-Harford et al., 2018*). Their work focused on shelf and shelf-slope waters that had slightly

lower Cr concentrations (on average 2.26 nM) and higher δ^{53}Cr values (on average 1.41‰) than open ocean waters at the same water depth (between 0 and 160 m) (*Goring-Harford et al., 2018*). However, similarly to this study, sub-surface waters at a single open-ocean site were slightly depleted in Cr and slightly enriched in heavy Cr isotopes (average Cr = 2.60 nM, δ^{53}Cr = 1.18‰) compared to deeper waters (average Cr = 2.70 nM, δ^{53}Cr = 1.13‰) (*Goring-Harford et al., 2018*).

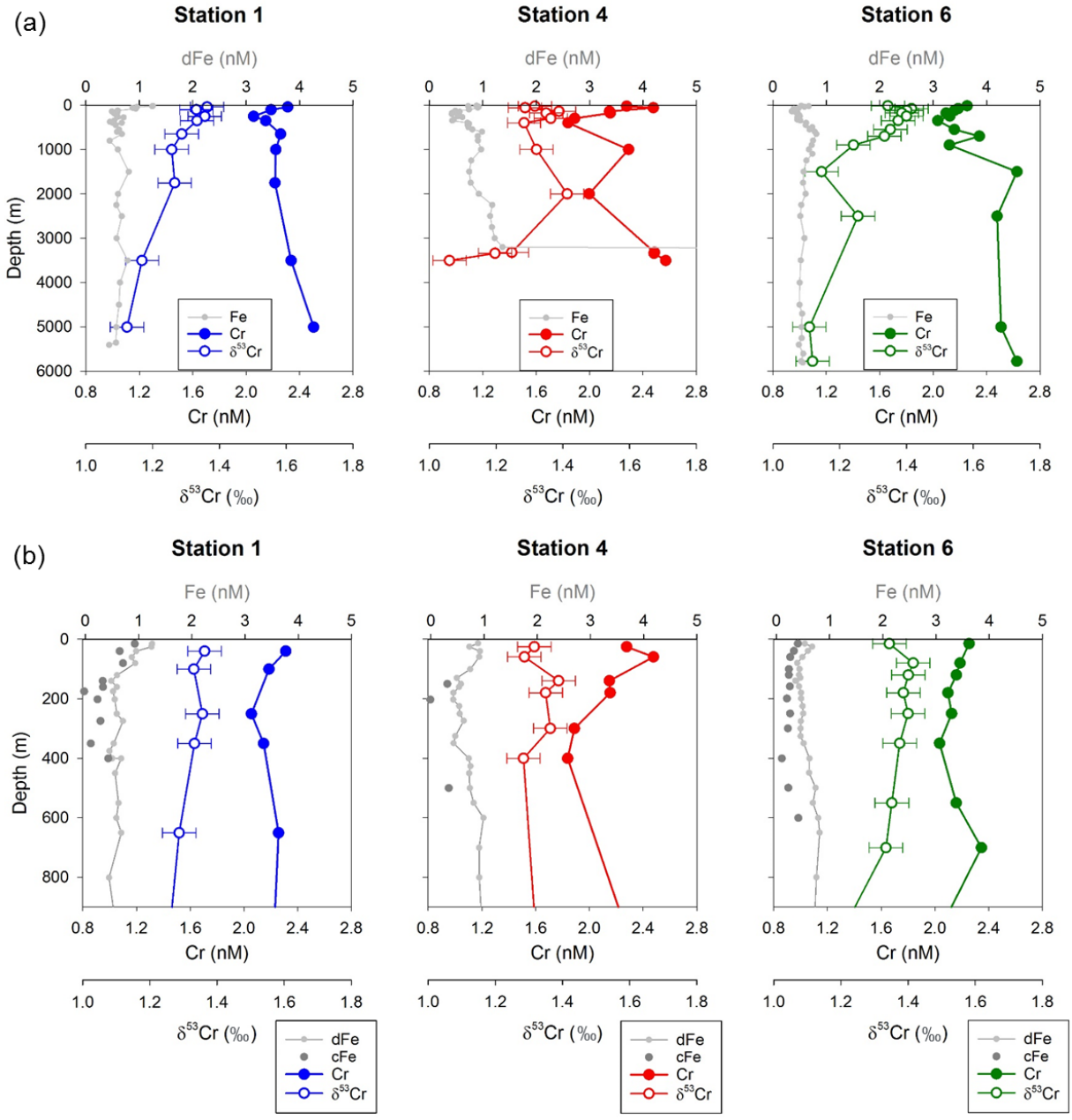

Figure 4-3 (a) Full water column depth profiles of Cr concentration, δ^{53}Cr values, and dissolved Fe concentrations at Stations 1, 4, and 6. **(b)** Profiles of Cr concentrations, δ^{53}Cr values, and dissolved and colloidal Fe concentrations for the upper 900 m water depths at Stations 1, 4 and 6. Error bars for Cr and Fe concentrations are smaller than the size of symbols. Error bars for δ^{53}Cr represent external reproducibility (± 0.05‰) based on the long-term precision of the chromium isotope standard (NBS979). All Cr data are given in Table C1. Fe data are from *Kunde et al. (2019)*.

4.4 Discussion

4.4.1 Potential sources of Cr to the North Atlantic

It is generally assumed that rivers are the main source of dissolved Cr to the oceans (*Bonnand et al., 2013; Reinhard et al., 2013*), whereas contributions of Cr from atmospheric dust deposition, benthic sedimentary inputs and hydrothermal vents vary from site to site but are usually small (*Achterberg and van den Berg, 1997; Goring-Harford et al., 2018; Sander and Koschinsky, 2000*).

Dust supply from North African deserts directly affects the subtropical North Atlantic ocean (*Jickells et al., 2015*). Input of Fe from dust deposition was evidenced across the transect by elevated concentrations of dissolved Fe in the surface mixed layer (SML), which extends to 20 m, 50 m and 60 m water depth respectively, for Stations 1, 4 and 6 (*Kunde et al., 2019*). A longitudinal decrease of surface dFe concentrations from west to east was observed, primarily attributed to variations in wind-derived dust fluxes (*Kunde et al., 2019*). Only two samples were collected for Cr analysis from within the SML (at Stations 4 and 6); these had Cr concentrations of 2.25-2.28 nM (Figure 4.3a), similar to the Cr concentration (2.33 ± 0.15 nM) for samples collected from sub-surface waters at these stations. The δ^{53}Cr values of dissolved Cr from the SML were between 1.32 to 1.34‰. The δ^{53}Cr value of atmospheric dust is expected to be similar to that of crustal rocks (−0.12 ± 0.10‰; *Schoenberg et al., 2008*), although dissolution promoted by strong ligands may preferentially release heavier Cr isotopes (δ^{53}Cr up to 1.23‰; *Saad et al., 2017*). The total Cr loading of North African aerosols is on average 4.6 ng m^{-3} based on results from the GEOTRACES GA03 study (*Shelley et al., 2015*). Given the average dry deposition velocity is 0.4 cm s^{-1} in the remote open ocean (*Duce et al., 1991*), then the dry deposition flux of Cr is calculated to be 5.8×10^4 ng m^{-2} y^{-1} in the subtropical North Atlantic. Assuming 10% of this Cr is soluble (*Chester and Murphy, 1990*) and dissolution occurs in the upper 50 m of the water column, dust derived Cr would be equivalent to an increase of ~0.002 nM per year to the SML. This is, however, negligible compared to the measured Cr concentrations in the SML. Considered together, there is no evidence for significant input of dissolved Cr from atmospheric dust deposition to the surface ocean in this region.

At Stations 1 and 6, Cr concentrations slightly increase from intermediate to deep waters. Samples collected from below 5000 m have the highest Cr concentrations (2.50-2.63 nM) and lowest δ^{53}Cr values (1.11-1.12‰) of the water column. If this is a result of input of metals from benthic sediments, then elevated dissolved Fe concentrations close to seafloor would be simultaneously observed. However, in the abyssal zone, dFe concentrations remain relatively constant (Station 6)

or are even slightly lower than intermediate waters (Station 1) (see Figure 4.3a). Scavenging of Fe onto resuspended sedimentary particles likely occurred at Station 1 (*Kunde et al., 2019*), but there is no evidence for this for Cr in the deep water. Overall, input of Cr from benthic sediments appears to be negligible in this study area.

The neutrally buoyant hydrothermal plume above the Snake Pit vent field was identified by a turbidity anomaly (Figure 4.2), and was sampled at water depths of between 3300-3500 m at Station 4. Dissolved Fe concentrations reached 27 nM within the plume, much higher than background seawater (~0.67 nM; *Kunde et al., 2019*), suggesting a substantial contribution of dFe from the Snake Pit vent fluids that have an end-member Fe concentration of ~3.5 mM (*Findlay et al., 2015*). Seawater samples from within the hydrothermal plume exhibit Cr concentrations of 2.48 to 2.57 nM and δ^{53}Cr values of 1.06 to 1.25‰ (Figure 4.3a). These Cr concentrations are slightly higher (by 0.14-0.23 nM) than a single sample collected from a similar water depth (3500 m) at Station 1. Hence, consistent with the idea that the Cr content of hydrothermal vent fluids is relatively low (< 2000 nM; *Sander and Koschinsky, 2000*) compared to other metals, the Snake Pit vent field does not seem to be an important source of Cr to the deep ocean. However, in contrast to my more detailed study of Cr behavior in hydrothermal plumes at TAG and Rainbow (Chapter 3), there was no evidence for removal of seawater Cr from within the hydrothermal plume at Snake Pit, at least for the two samples studied here.

4.4.2 Removal of Cr in subsurface waters

Lowest Cr concentrations coincide with lowest dissolved and colloidal Fe concentrations at between 100 and 400 m water depth (Figure 4.3b), suggesting the coupled cycling of Cr and Fe in subsurface waters. Depletion of dFe is associated with removal of cFe from the subsurface waters, and is not a direct result of biological uptake (*Kunde et al., 2019*). This is because: (1) experimental studies have suggested that soluble Fe is biologically preferred over cFe (*Chen and Wang, 2001*); (2) lowest cFe concentrations occur below the deep Chl-a maximum that reflects enhanced biological activity (Figure 4.3b); and (3) an enrichment of particulate Fe, which would capture the cellular Fe pool, was not observed (*Kunde et al., 2019*). Instead, aggregation of cFe (likely in the form of Fe(III)) into filterable particles and/or scavenging of cFe onto settling particles is considered to account for the subsurface deficit of dFe (*Kunde et al.,2019*) and, presumably, removal of Cr.

Concentrations of Cr in the subsurface waters are ~9 - 20% lower than in the surfaced mixed layer (2.25-2.28 nM) at the 3 stations sampled in this study, in contrast to the more subtle depletion (< 2%) of dissolved Cr in shallow waters compared to deeper waters (Winter Water) observed in the Southern Ocean (*Rickli et al., 2019*). The (sub)tropical North Atlantic receives almost half of the

global deposition flux of dust to the oceans (*Jickells et al., 2015*), and modelling studies suggest that this is one of the few regions that display elevated concentrations of suspended lithogenic particles at the ocean surface (*Ye and Völker, 2017*). In the presence of a relatively high particle load, the rate of colloidal aggregation is predicted to increase due to so-called 'particle concentration effects' (*Stordal et al., 1996*). As a result, authigenic Fe particles that are formed from aggregation of colloidal Fe may scavenge/adsorb a fraction of seawater Cr, probably in the form of Cr(III). In addition, dust-derived particles may sink through the deep Chl-a maximum (*Ohnemus and Lam, 2015*) and continue to exert a scavenging potential in subsurface and intermediate waters.

Highest $\delta^{53}Cr$ values were found at similar depth to the lowest Cr (and Fe) concentrations in subsurface waters (Figure 4.3b), which is consistent with preferential removal of isotopically light Cr. This Cr is probably in the form of Cr(III), which may have been produced in situ via biologically and photochemically mediated reduction of Cr(VI) in the euphotic zone (*Achterberg and van den Berg, 1997; Connelly et al., 2006; Li et al., 2009; Janssen et al., 2020*). Previously laboratory (*Ellis et al., 2002; Døssing et al., 2011; Kitchen et al., 2012*) and field (*Wang et al., 2019; Janssen et al., 2020*) studies have shown that Cr(III) is isotopically light relative to Cr(VI), which is a result of redox-dependent fractionation of Cr. Cr(III) species can be effectively scavenged by Fe(III) (oxyhydr)oxides (*Frei et al., 2013*), clay minerals and sand (*Richard and Bourg, 1991*) as well as biogenic particles (*Semeniuk et al., 2016*), whereas Cr(VI) does not readily adsorb onto Fe-oxides (*Gueguen et al., 2016*) or SiO_2-Al_2O_3 minerals (*Frank et al., 2009*) in oxic seawater and therefore tends to remain in the water column.

A positive correlation between $\delta^{53}Cr$ and turbidity ($r^2 = 0.50$; Figure 4.4a) is found for the subsurface seawater samples (excluding the SML), which supports the idea that relatively isotopically light Cr(III) is removed onto particles. This is in agreement with observations of increased $\delta^{53}Cr$ values with higher particle concentration in shelf waters (*Goring-Harford et al., 2018*). The negative correlation between $\delta^{53}Cr$ and dFe concentration (Figure 4.4b) further indicates that removal of isotopically light Cr coincides with removal of dFe and thus, via aggregation and/or scavenging processes. By contrast, there is no strong correlation between $\delta^{53}Cr$ and Chl-*a* concentration for the seawater samples analysed in this study (Figure 4.4a), suggesting that biological activity does not have a direct control on total dissolved Cr isotope variations. However, this does not mean that biologically mediated Cr redox reactions do not occur; rather, changes in $\delta^{53}Cr$ of total Cr cannot be observed if the Cr(III) that is produced via reduction of Cr(VI) is not removed from the dissolved Cr pool.

There is no correlation between $\delta^{53}Cr$ and O_2 concentrations for samples from all 3 stations (Figure 4.4a), indicating that O_2 level has no control on $\delta^{53}Cr$ of total Cr in waters that are only slightly O_2 deficient (O_2 concentrations >130 µmol/kg). Recent studies on oxygen deficient waters in the sub-

tropical Atlantic and the eastern tropical North Pacific have drawn the same conclusion (*Goring-Harford et al., 2018; X. Wang et al., 2019; Moos et al., 2020*). It appears that reduction of Cr(VI) only occurs in waters with extremely low levels of oxygen (*Nasemann et al., 2020*). In addition, retention of some of the isotopically light Cr(III) within the water column would partially offset the residual heavy Cr(VI) in analyses of total dissolved Cr (*Moos et al., 2020*).

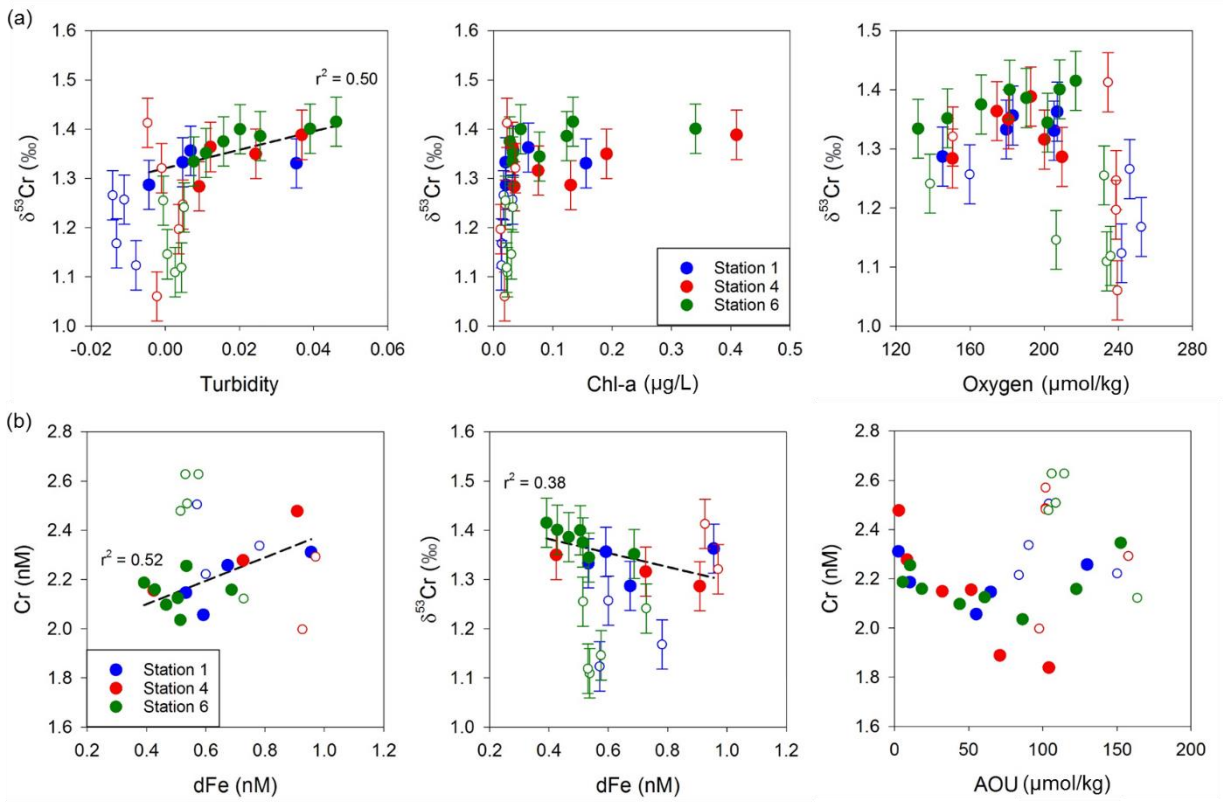

Figure 4-4 (a) $\delta^{53}Cr$ as a function of turbidity, Chl-*a* concentration, and dissolved oxygen, respectively. **(b)** Cr as a function of dFe concentration (left), $\delta^{53}Cr$ as a function of dFe concentration (middle), Cr as a function of apparent oxygen utilization (right). Filled circles represent data from the upper water column (above 900 m water depth; excluding data from surface mixed layer for turbidity) and open circles represent data from deeper waters (below 900 m depth). Fe data are from *Kunde et al. (2019)*.

4.4.3 Regeneration of Cr in deeper waters

While concentrations of total dissolved Cr are highest in deep waters, concentrations of Cr and Fe were only correlated in the upper 900 m of the water column (Figure 4.4b). Despite the concurrent removal of Cr and Fe in subsurface waters, the cycling of Cr and Fe is apparently decoupled in deeper waters. Mesopelagic dFe correlates with apparent oxygen utilisation (AOU) that reflects remineralisation of sinking organic material within the water column (*Kunde et al., 2019*). However,

there is no such relationship between Cr and AOU, either in subsurface or in deeper waters (Figure 4.4b), suggesting that, in contrast to dFe, primary production and respiration have no significant control on Cr concentrations.

As discussed above, removal of Cr in subsurface waters likely proceeds via scavenging of Cr(III) by colloid aggregates that consist of authigenic (oxyhydr)oxides and/or dust particles. Regeneration of Cr in deeper waters could proceed via re-oxidation of Cr(III) to the less particle reactive Cr(VI) by reduction (and dissolution) of manganese oxides (MnO_2) (*Eary and Rai, 1987; Semeniuk et al., 2016*) that would release relatively isotopically light $\delta^{53}Cr$ into the dissolved Cr pool (*Farkaš et al., 2018*). The half-life for Cr oxidation by MnO_2 in aqueous environments is predicted to be rather slow, ~95 days (*Eary and Rai, 1987*), but is nevertheless comparable to the residence time (months to years) of fine lithogenic mineral particles (~1 to 5 µm) in the upper 2000 m of the North Atlantic Ocean water column (*Ohnemus et al., 2018*).

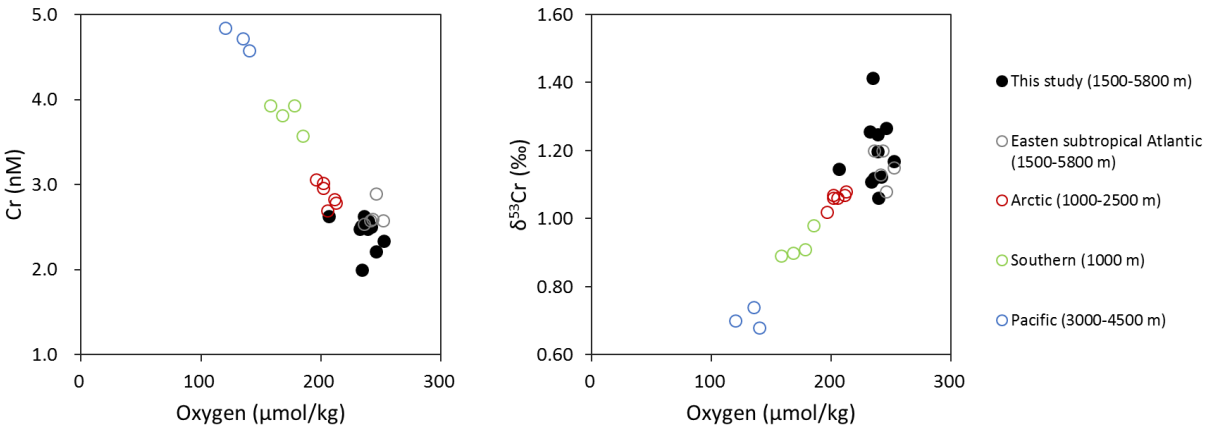

Figure 4-5 Cr and $\delta^{53}Cr$ compared to dissolved oxygen concentrations in deep ocean waters (> 1000 m depth; excluding samples from the oxygen minimum zones). Cr and oxygen data are from: this study (sub-tropical North Atlantic); *Goring-Harford et al. (2018)* (eastern subtropical Atlantic); *Scheiderich et al. (2015)* (Arctic); *Rickli et al. (2019)* (Southern Ocean); *Moos and Boyle (2019)* (North Pacific).

The overall higher Cr and lower $\delta^{53}Cr$ values in deeper waters relative to subsurface waters at the three stations in the sub-tropical North Atlantic are consistent with the potential regeneration of isotopically light Cr(III). Similarly, *Moos and Boyle (2019)* reported a nutrient-type profile for Cr in the North Pacific (SAFe station). Pacific deep waters have a higher Cr content and lower $\delta^{53}Cr$ value (Cr = 4.71 nM and $\delta^{53}Cr$ = 0.71‰ at water depths 3000-4500 m; *Moos and Boyle, 2019*) compared to Atlantic deep waters measured in this study (average Cr = 2.39 nM, $\delta^{53}Cr$ = 1.21‰). A compiliation of literature data (*Scheiderich et al., 2015; Rickli et al., 2019; Moos and Boyle, 2019*)

also supports the idea that deep water Cr concentrations increase along the thermohaline conveyor belt, whereas the $\delta^{53}Cr$ value of total dissolved Cr decreases (Figure 4.5). Thus, isotopically light Cr accumulates in deep waters presumably via release from sinking particles as the deep water masses age as they flow from the Atlantic Ocean to the Southern Ocean and finally to the Pacific Ocean.

4.4.4 Global correlation between seawater Cr and $\delta^{53}Cr$

Data from this study illustrate an inverse correlation between $\delta^{53}Cr$ and logarithmic Cr concentration ($r^2 = 0.53$, n = 33; Figure 4.6a) and the slope of the linear regression is −0.79 ± 0.13‰. This is consistent with the previously proposed global $\delta^{53}Cr$-ln[Cr] relationship for the open ocean, which was considered to reflect a closed-system Rayleigh-type fractionation of Cr isotopes (*Scheiderich et al., 2015;* Figure 4.6):

$$\delta^{53}Cr_{Cr(VI)} = \delta^{53}Cr_0 + \varepsilon \times \ln(f) \quad (4\text{-}2)$$

where $\delta^{53}Cr_0$ represents the initial Cr isotope composition, f represents the fraction of Cr remaining in seawater, and ε is the isotope fractionation factor between Cr(III) and Cr(VI). The Cr isotope fractionation factor derived from the slope of the line on a plot of $\delta^{53}Cr$ versus ln[Cr] for all open ocean seawater samples reported in the literature to date is ε = −0.63 ± 0.03‰ ($r^2 = 0.67$, n = 250: *Bonnand et al., 2013; Goring-Harford et al. 2018; Scheiderich et al., 2015; Rickli et al., 2019; Bruggmann et al., 2019; Wang et al., 2019; Moos and Boyle, 2019; Moos et al., 2020; Janssen et al., 2020; this study*).

The relatively small Cr isotope fractionation as inferred from the global seawater dataset is not entirely consistent with laboratory determined fractionation factors for Cr reduction by Fe(II) and/or organic matter (ε = −1.5 to −4.2 ‰: *Døssing et al., 2011; Kitchen et al., 2012; Basu and Johnson, 2012),* or biotic Cr reduction (ε = −1.6 to −4.3 ‰: *Zhang et al., 2018, 2019*). Possible explanations for this discrepancy could be: (1) Cr is reduced in the euphotic zone due to biological and/or photochemical processes (*Janssen et al., 2020*), but the theoretically larger Cr isotope fractionation may be diminished if a portion of isotopically light Cr(III) remains in the water column (*Moos et al., 2020*); (2) the fractionation factor may be influenced by the rate of Cr reduction and removal (*Jamieson-Hanes et al., 2014*); and (3) scavenging/adsorption of Cr onto particles may cause a small (but as yet unconstrained) isotope fractionation (*Semeniuk et al., 2016; Ellis et al., 2004*).

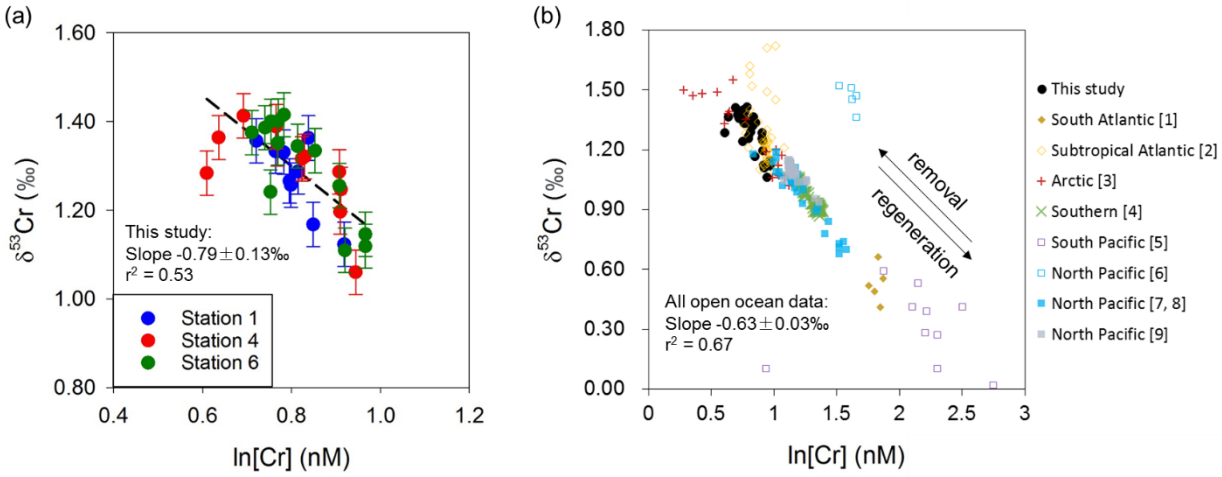

Figure 4-6 (a) Relationship between δ^{53}Cr and ln[Cr] for new data from this study. **(b)** Relationship between δ^{53}Cr and ln[Cr] for the global open ocean seawater. Literature data are from: [1] *Bonnand et al. (2013)* (South Atlantic); [2] *Goring-Harford et al. (2018)* (eastern subtropical Atlantic); [3] *Scheiderich et al. (2015)* (Arctic); [4] *Rickli et al. (2019)* (Southern Ocean); [5] *Bruggmann et al. (2019)* (South Pacific); [6] *X. Wang et al. (2019)* (eastern tropical North Pacific); [7] *Moos & Boyle (2019)* (North Pacific); [8] *Moos et al. (2020)* (eastern tropical North Pacific); [9] *Janssen et al. (2020)* (North Pacific).

This study suggests that the systematic δ^{53}Cr-Cr relationship holds regardless of locality (Figure 4.6b) and is a result of internal cycling processes of Cr. As discussed in Section 4.4.3, removal and regeneration of isotopically light Cr(III) can account for the distributions of Cr and Cr isotopes not only in the sub-tripcal North Atlantic, but also at the global scale. Relatively old water masses (e.g. Pacific deep water) accumulate Cr with a lower δ^{53}Cr value as a result of progressive regeneration of Cr that is removed from the upper water column. There is relatively little scatter in the global δ^{53}Cr-Cr relationship (Figure 4.6), meaning that any isotope fractionation that occurs during Cr regeneration must be small, presumably due to near quantitative oxidation of Cr(III) (*Farkaš et al., 2018*).

4.5 Conclusions

This study investigated full water column depth profiles of dissolved Cr and δ^{53}Cr at three stations in the sub-tropical North Atlantic, in order to better understand the processes that regulate the behaviour of Cr and Cr isotopes in the modern ocean. Subsurface waters (above 900 m depth) are depleted in Cr, and enriched in heavy Cr isotopes, relative to deeper waters. High δ^{53}Cr values (up to 1.4‰) in subsurface waters are not directly controlled by levels of oxygen or biological uptake, but are consistent with preferential removal of light Cr isotopes, probably Cr(III), onto authigenic Fe particles. Regeneration of Cr in deeper waters, possibly via re-oxidation of Cr(III) back to Cr(VI), leads to subtly increased levels of Cr at individual sites, but is more obvious at the global scale. The

net Cr isotope fractionation factor derived for Cr isotope data from the sub-tropical North Atlantic is $\varepsilon \approx -0.79‰$, consistent with the global δ^{53}Cr-ln[Cr] relationship. Overall, removal and regeneration of relatively isotopically light Cr account for the global distributions of Cr and Cr isotopes and the systematic δ^{53}Cr-ln[Cr] relationship.

Chapter 5 Conclusions and outlook

Trace metals are important micronutrients that regulate primary productivity in some parts of the ocean. As the oceans warm, trace metal distributions may change, but the effects of this on primary productivity are hard to predict because of ongoing debate on the supply of trace metals. It is now clear that, in some parts of the ocean, inputs of hydrothermal iron (Fe) may be more significant than previously thought. However, the chemical processes in hydrothermal plumes that regulate the dispersal of ridge-derived Fe are poorly constrained, making it difficult to assess the far field impacts of hydrothermal sources on the deep ocean metal inventory and on primary productivity in surface waters.

Due to the redox-sensitivity of chromium (Cr) isotopes and the potential of marine sediments to record past variations in the Cr isotopic composition of seawater (and hence a record of seawater oxygenation), it is vital to understand the modern-day distribution of Cr and its isotopes in seawater. However, similarly to iron, the processes that regulate the behaviour of Cr isotopes in the modern ocean are not well understood, and the effects of biological activity, benthic processes and hydrothermal inputs on Cr distributions, in addition to levels of dissolved oxygen, need to be quantified.

Stable Fe and Cr isotopes are emerging tools for assessing the provenance of metal inputs to the ocean, and for exploring the effects of biogeochemical cycling and redox processes. These themes have been explored in this thesis, and this chapter summarises my key findings. This is followed by recommendations for future research that would utilise Fe and Cr isotopes to better understand the biogeochemical cycling of Fe and Cr in the oceans.

5.1 Key findings

5.1.1 Iron isotope behaviour in hydrothermal systems

The Fe isotopic compositions (δ^{56}Fe) of dissolved and total dissolvable Fe have been determined in vent fluids and the near-field hydrothermal plumes at the Beebe and the Von Damm vent fields, which are located along the ultraslow Mid-Cayman spreading centre in the Caribbean Sea (**Chapter 2**). Results show that the δ^{56}Fe of dissolved Fe in the near-field plumes was lower (as low as −4.08‰) than the hydrothermal vent fluids (−0.28‰). This indicates that the δ^{56}Fe of dFe is principally controlled by oxidation of Fe(II) and precipitation of Fe-(oxyhydr)oxides that preferentially incorporate heavy Fe isotopes. In support of this, the δ^{56}Fe value of labile particulate Fe was always higher than the δ^{56}Fe of dissolved Fe. Nevertheless, at Beebe, the δ^{56}Fe of total dissolvable Fe

evolves to higher values as particles fall out of the plume, indicating preferential loss of Fe-sulfides that are enriched in light Fe isotopes, presumably due to coagulation of Fe-sulfide nanoparticles. The δ^{56}Fe signature of hydrothermal Fe delivered to the ocean interior is controlled by both the vent fluid Fe/H_2S stoichiometry and the Fe(II) oxidation rate.

5.1.2 Coupled cycling of iron and chromium in hydrothermal plumes

Chemical processes in the hydrothermal plume that regulate the hydrothermal inputs of Fe and Cr to the North Atlantic Ocean were investigated in **Chapter 3**. For the first time, it is shown that Fe and Cr isotope profiles through the hydrothermal plume are the 'mirror image' of one another, providing compelling evidence for coupled Fe(II) oxidation and Cr(VI) reduction in the hydrothermal plume. Oxidation of Fe(II) and precipitation of Fe-(oxyhydr)oxides accounts for the low δ^{56}Fe values of dissolved Fe (as low as −1.91‰ at TAG and −6.95‰ at Rainbow); differences in δ^{56}dFe values between the two sites likely reflect differences in the proportion of dissolved Fe that precipitates as Fe-sulfide vs. Fe-(oxyhydr)oxide as the hydrothermal fluids mix with seawater. The δ^{56}Fe of dissolved Fe evolves to heavier values (−0.44 to 0.23‰) in the distal part of the hydrothermal plume, likely controlled by exchange of Fe between the dissolved and particulate fraction as suggested by Fe incubation experiments. The δ^{56}Fe signature of dFe can be used to distinguish Fe inputs from dust and hydrothermal activity, and my data indicate that hydrothermal venting potentially contributes ~18-58% of dissolved Fe to the oceanic inventory in the North Atlantic, at distances of up to 250 km away from the vent sites.

Cr reduction is suggested by elevated δ^{53}Cr values in the TAG and Rainbow hydrothermal plumes (as high as 1.21‰ and 1.87‰ respectively) compared to background seawater. At Rainbow, the difference between the δ^{53}Cr of Cr(III) and Cr(VI) is estimated to be ~ −4.6‰, significantly greater than that calculated for the 'global correlation' between Cr concentration and δ^{53}Cr in seawater. Reduction of Cr and scavenging by Fe-(oxyhydr)oxide particles in the hydrothermal plume means that high-temperature hydrothermal systems are a sink for seawater Cr, potentially removing up to 20% of the riverine flux. Overall, processes in hydrothermal plumes have the potential to significantly modify the Fe and Cr isotopic signatures of hydrothermal fluids.

5.1.3 Chromium biogeochemical cycling in the sub-tropical North Atlantic Ocean

Full water column depth profiles of dissolved Cr and δ^{53}Cr were obtained for three stations across the sub-tropical North Atlantic Ocean (**Chapter 4**). Subsurface waters (above 900 m depth) were depleted in Cr, and enriched in heavy Cr isotopes, relative to deeper waters. High δ^{53}Cr values (up to 1.4‰) in subsurface waters are consistent with preferential removal of light Cr isotopes,

probably Cr(III), onto authigenic Fe particles, but are not directly controlled by levels of oxygen or biological uptake. Regeneration of Cr in deeper waters, possibly via re-oxidation of Cr(III) back to Cr(VI), leads to subtly increased levels of Cr at individual sites, but this is more obvious at the global scale. The net Cr isotope fractionation factor derived for Cr isotope data from the sub-tropical North Atlantic is $\varepsilon \approx -0.79‰$, consistent with the global δ^{53}Cr-ln[Cr] relationship. Removal and regeneration of relatively isotopically light Cr can account for the globally heterogeneous distributions of Cr and Cr isotopes.

5.2 Recommendations for further research

While the Fe isotopic signature of seawater has proved useful for distinguishing between inputs of Fe from atmospheric deposition and seafloor sediments, the Fe isotope signature of hydrothermal sources is complicated by precipitation of Fe-sulfides and Fe-(oxyhydr)oxides that occur as vent fluids mix with seawater. The δ^{56}Fe signature of hydrothermal Fe delivered to the ocean interior is controlled by both the vent fluid Fe/H_2S stoichiometry and the Fe(II) oxidation rate; however, the relative importance of these two parameters cannot, as yet, be constrained. There have only been a handful of studies available that allow hydrothermal plume δ^{56}Fe signatures to be compared with vent fluid chemistry and the chemistry of the overlying seawater (*Conway and John, 2014; Klar et al., 2017; Lough et al., 2017; Fitzsimmons et al., 2017; Nasemann et al., 2018; Rouxel et al., 2018*). Extending the analysis of Fe isotope compositions of plume material (dissolved and particulate phases) to other hydrothermal systems, such as Lucky Strike and Lost City vent fields on the Mid-Atlantic Ridge would be useful to fully constrain the importance of hydrothermal Fe sources in the deep, and potentially even the surface, ocean.

Modelling studies have shown improved ability to reproduce Fe distributions when hydrothermal Fe sources are included, and have predicted that uptake of hydrothermal Fe increases productivity in the Southern Ocean, fueling 20-30% more carbon export in some regions (*Tagliabue et al., 2010*). However, these models assumed that hydrothermal Fe fluxes are proportional to seafloor spreading rates, without considering the behavior of Fe in the hydrothermal plume, or variations in Fe fluxes from different vent sites. Extending the models to incorporate these parameters, as well as increasing observations of Fe concentrations and Fe isotope distributions, not only in hydrothermal systems but also in the upper ocean water column, is critical for providing reliable predictions of future variations in the distribution of Fe and other micronutrients and consequently the climate change.

Variations in δ^{53}Cr of dissolved Cr should principally be driven by redox-dependent processes, because Cr(VI) can be effectively reduced to Cr(III) in the presence of Fe(II) and/or organic matter,

and this process is accompanied by a significant Cr isotope fractionation. However, even parts of the ocean that have very low levels of oxygen do not exhibit significant variations in δ^{53}dCr (*Goring-Harford et al., 2018; Wang et al., 2019; Moos et al., 2020; Nasemann et al., 2020*). Presumably this is because changes in δ^{53}Cr of dissolved Cr cannot be observed if the Cr(III) that is produced via reduction of Cr(VI) is not removed from the dissolved Cr pool. To date, there are few studies of the Cr isotopic composition of single Cr species (*Wang et al., 2019; Davidson et al., 2019*). Future studies of Cr speciation, the Cr isotope compositions of co-existing Cr(III) and Cr(VI) species and hence species-dependent Cr isotope fractionation across a range of oceanic settings (oxic, suboxic, and anoxic) would shed new light on the biogeochemical processes controlling the behavior of Cr isotopes in the modern ocean and ultimately the potential of the sedimentary δ^{53}Cr record for evaluating the evolution of atmospheric and ocean oxygenation.

The 'mirror image' of Fe and Cr isotope profiles observed in the Rainbow and TAG hydrothermal plumes provides compelling evidence for the coupled Fe oxidation and Cr reduction processes in deep ocean hydrothermal plumes. The coupled cycling of Fe and Cr may also occur in other marine environments. For instance, Fe(II) released from anoxic shelf sediments can act as an electron donor for the reduction of seawater Cr(VI); this process would yield a relatively large Cr isotope fractionation factor which is inconsistent with that inferred from the global seawater dataset (*Moos, 2018*). Further investigations on the paired behaviors of Fe, Cr and their isotopes at the sediment-seawater interface, in riverine and estuarine systems, as well as in hydrothermal systems would be valuable; investigations into the biogeochemical factors that regulate Fe and Cr dynamics, including influence of organic ligands, Mn-oxides, and H_2S, are also promising areas of future research. These would provide new insights as to the oceanic cycling of Fe and Cr, as well as the input and output fluxes of Fe and Cr to/from the oceans.

Appendix A Supporting information for Chapter 2

A.1 Compositions of all vent fluid samples collected on cruise JC82

Vent site	Temp ℃	pH	H_2S mM	Mg mM	Mn µM	Fe µM	Source
Beebe vent field							
Beebe 125	401	3.1	0.3	2.7	584	6168 *	*Lough (2016)*
Beebe 125	401	6.1	4.7	46.2	57	621	*Lough (2016)*
Beebe 125	401	6.0	1.8	42.1	93	845	*Lough (2016)*
Beebe 125	401	3.1	4.2	2.1	589	6450	*Lough (2016)*
Beebe 125	401	3.9	1.3	34.6	201	2034	*Lough (2016)*
Beebe 125	401	3.1	3.2	5.7	527	3284 *	*Lough (2016)*
Beebe 125	401	3.0	3.2	3.1	537	5466 *	*Lough (2016)*
Deepest Vents	393	2.9	5.1	5.5	553	5744 *	*Lough (2016)*
Deepest Vents	393	3.0	6.9	10.0	500	8421	*Lough (2016)*
Deepest Vents	393	3.4	3.7	22.1	377	NA	*Lough (2016)*
Beebe Woods	350	3.7	4.4	16.9	403	28516	*Lough (2016)*
Beebe Woods	350	3.5	2.6	27.4	280	29750	*Lough (2016)*
Beebe Woods	350	4.8	4.4	40.1	133	53113	*Lough (2016)*
Beebe Woods	350	4.3	1.9	36.0	185	24060	*Lough (2016)*
seawater		*8.2*	*0*	*52*	*0.001*	*0.001*	
Beebe end-member (Vent 1, 3, 5 average)			*12*	*0*	*550*	*6.6*	*McDermott et al. (2018)*
Beebe Woods end-member			*11.9*	*0*	*556*	*12.5*	*McDermott et al. (2018)*
Von Damm vent field							
Main Spire	215	6.0	1.0	15.1	8	18 *	*Lough (2016)*
Main Spire	215	6.2	0.9	32.1	5	7	*Lough (2016)*
Main Spire	215	6.3	0.9	29.1	5	6	*Lough (2016)*
Hotter than Hole	133	6.2	0.3	28.0	10	141	*Lough (2016)*
Hotter than Hole	133	6.1	0.5	26.9	12	292 *	*Lough (2016)*
Hotter than Hole	133	6.2	1.0	30.3	15	334 *	*Lough (2016)*
X15 marker	111	6.4	0.8	30.0	12	750 *	*Lough (2016)*
Chimlet 2	107	6.2	0.7	23.3	11	148	*Lough (2016)*
Chimlet 2	107	7.0	NA	41.6	10	145 *	*Lough (2016)*
seawater		*8.2*	*0*	*52*	*0.001*	*0.001*	
East Summit end-member			*3.2*	*0*	*10*	*20*	*McDermott (2015)*

Data are from *Lough (2016)* for calculating hydrothermal end-member concentrations; and from *McDermott (2015)* for comparison. NA = not available, seawater value is a generic value for background seawater not a measured sample. These vent fluid data have previously been published in *Lough et al. (2019a)* and *Hodgkinson et al. (2015)*. Fe concentration data marked with * represent data measured from this study.

A.2 The $\delta^{56}Fe$ values versus Mg concentration in Beebe and Von Damm vent fluids

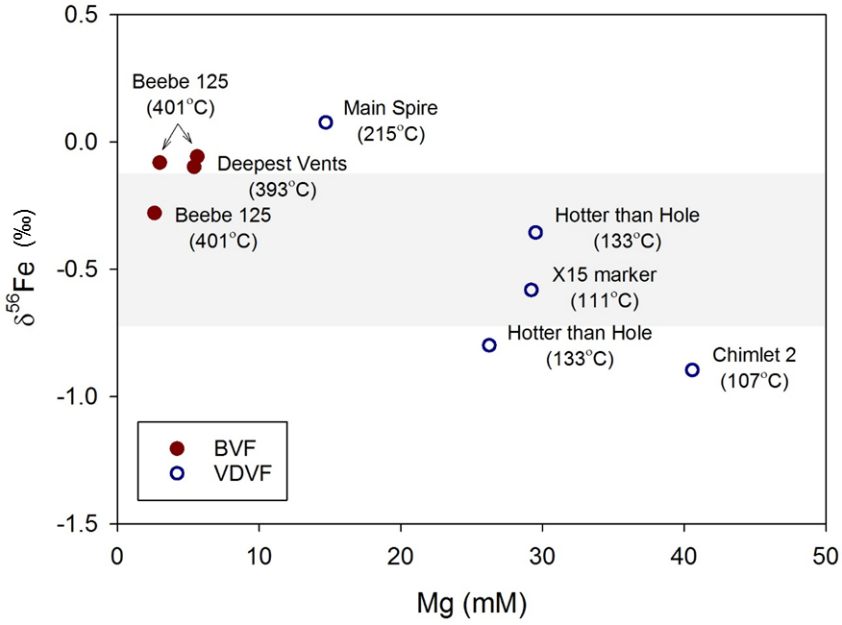

The grey band represents the range of end-member vent fluid $\delta^{56}Fe$ (−0.67 to −0.13‰) from literatures (Table A4).

A.3 Fe isotope compositions of dissolved and total dissolvable Fe in hydrothermal plumes at the Beebe and the Von Damm vent fields

Sample	Depth	δ^{56}dFe (‰) measured					δ^{56}TDFe (‰) measured					dFe (nM)	TDFe (nM)	δ^{56}LPFe (‰)	pFe (nM)	dMn (nM)	BP dilution factor	VF dilition factor	
	(m)	*(1)*	2SE	*(2)*	2SE	Average	*(1)*	2SE	*(2)*	2SE	Average	measured	measured	calculated	calculated	measured		Average	SD
Beebe vent field																			
CTD4 N5	4719	0.24	0.04	NA	NA	**0.24**	0.16	0.04	NA	NA	**0.16**	**23**	**50**	0.09	26	10	19.1	58838	1786
CTD4 N4	4790	0.31	0.02	0.28	0.04	**0.29**	NA	NA	NA	NA	NA	**16**	NA	NA	NA	9	21.2	65449	1986
CTD4 N3	4855	-0.25	0.03	-0.26	0.04	**-0.25**	-0.01	0.04	0.06	0.02	**0.02**	**24**	**108**	0.1	84	13	14.6	45155	1370
CTD10 N1	4957	-2.46	0.02	-2.49	0.05	**-2.47**	0.00	0.05	-0.06	0.05	**-0.03**	**79**	**475**	0.46	396	83	2.3	7027	213
CTD10 N2	4956	-4.07	0.03	-4.10	0.04	**-4.08**	-0.03	0.05	-0.11	0.03	**-0.07**	**86**	**754**	0.45	667	114	1.7	5114	155
CTD10 N4	4952	-3.25	0.04	-3.21	0.04	**-3.23**	0.44	0.03	0.40	0.02	**0.42**	**44**	**596**	0.71	552	189	1.0	3084	94
CTD10 N5	4952	-1.43	0.03	-1.42	0.03	**-1.43**	0.22	0.04	0.11	0.06	**0.17**	**36**	**504**	0.29	469	109	1.7	5349	162
Von Damm vent field																			
ISIS201 N5	2277	-0.71	0.03	NA	NA	**-0.71**	-0.04	0.04	-0.07	0.04	**-0.05**	**21**	**580**	-0.03	559	91	2.9	198	109
ISIS200 N6	2294	-2.48	0.03	-2.51	0.03	**-2.49**	-0.16	0.05	NA	NA	**-0.16**	**43**	**198**	0.48	155	50	5.3	361	198
ISIS200 N5	2294	0.16	0.03	0.18	0.03	**0.17**	0.12	0.03	0.14	0.03	**0.13**	**35**	**292**	0.12	257	5	54.3	3673	2020
ISIS200 N4	2285	-0.70	0.02	NA	NA	**-0.60**	-0.16	0.06	-0.27	0.06	**-0.22**	**63**	**313**	-0.13	251	266	1.000	68	37
ISIS200 N2	2299	0.06	0.03	0.13	0.04	**0.10**	-0.10	0.05	NA	NA	**-0.10**	**24**	**60**	-0.23	36	19	14.1	952	524
ISIS199 N3	2281	0.20	0.03	0.24	0.03	**0.22**	-0.03	0.04	NA	NA	**-0.03**	**40**	**69**	-0.38	29	2	139.9	9474	5210

NA = not available; abbreviations: dFe = dissolved manganese, dFe = dissolved iron, TDFe = total dissolvable iron, LPFe = labile particulate iron, BP = buoyant plume, VF = vent fluid. Numbers *(1), (2)* represent two replicate MC-ICP-MS measurements on the same sample solution. 2SE is the internal error of each MC-ICP-MS measurement and reflects the analytical uncertainty (typically between 0.02‰ and 0.06‰). The external reproducibility (2SD) for δ^{56}Fe is ± 0.09‰ based on the long-term precision of the iron isotope standard (ETH) and is presented in the figures.

A.4 Literature data for Fe isotope compositions in end-member vent fluids from contrasting types of hydrothermal systems

Study area	Vent site	Substrate	Sample ID	Mg	Fe		δ^{56}Fe (‰)	Notes	Mn		H_2S		Source
9-10° N East Pacific Rise	K vent	basalt	ALV-4053	0	197	µM	**-0.25**	inc dregs	221	µM	~5	mM	*Rouxel et al. (2008)*
9-10° N East Pacific Rise	Bio9''	basalt	ALV-4057	0	3584	µM	**-0.41**	inc dregs	540	µM	~4	mM	*Rouxel et al. (2008)*
9-10° N East Pacific Rise	Tica vent	basalt	ALV-4059	0	1577	µM	**-0.36**	inc dregs	421	µM	~2.5	mM	*Rouxel et al. (2008)*
9-10° N East Pacific Rise	Biovent	basalt	ALV-4061	0	289	µM	**-0.67**	inc dregs	192	µM	~2.5	mM	*Rouxel et al. (2008)*
9-10° N East Pacific Rise	P vent	basalt	ALV-4393	0	3404	µM	**-0.41**	inc dregs	61.7	µM	~2	mM	*Rouxel et al. (2016)*
9-10° N East Pacific Rise	A vent	basalt	2360-1C	0	1560	µmol/kg	**-0.25**	all ex dregs; recalc rel to IRMM	237	µmol/kg	33.7	mmol/kg	*Beard et al. (2003); Von Damm (2000)*
21.5° S East Pacific Rise	Brandon (vapour)	basalt	3290-13	3.67 mmol/kg	8680	µmol/kg	**-0.17**	all ex dregs; recalc rel to IRMM	790	µmol/kg	7.52	mmol/kg	*Beard et al. (2003); Von Damm et al. (2003)*
21.5° S East Pacific Rise	Brandon (Brine)	basalt	3306-12C	7.08 mmol/kg	12300	µmol/kg	**-0.22**	all ex dregs; recalc rel to IRMM	1300	µmol/kg	6.86	mmol/kg	*Beard et al. (2003); Von Damm et al. (2003)*
Juan de Fuca Ridge	Main Endeavour (Bastille)	basalt	NA	0 for concs, 3.3 mmol/kg for isotopes	1.5	mmol/kg	**-0.25**	excl dregs; recalc rel to IRMM	550	µmol/kg	20	mmol/kg	*Sharma et al. (2001)*
Juan de Fuca Ridge	Main Endeavour (S&M)	basalt	NA	0 for concs, 0.75 mmol/kg for isotopes	2.8	mmol/kg	**-0.32**	excl dregs; recalc rel to IRMM	550	µmol/kg	11	mmol/kg	*Sharma et al. (2001)*
Juan de Fuca Ridge	Main Endeavour (Grotto)	basalt	NA	0 for concs, 0.57 mmol/kg for isotopes	1.2	mmol/kg	**-0.13**	excl dregs; recalc rel to IRMM	289	µmol/kg	8	mmol/kg	*Sharma et al. (2001)*
Juan de Fuca Ridge	Axial Volcano (Inferno)	basalt	NA	0 for concs, 1.65 mmol/kg for isotopes	0.42	mmol/kg	**-0.60**	excl dregs; recalc rel to IRMM	1150	µmol/kg	9	mmol/kg	*Sharma et al. (2001)*
Vanuatu back-arc	Nifonea-1	basaltic-trachyandesitic	27-14B	0 for concs, 12.3 mM for isotopes	1200	µM	**-0.66**	inc dregs	551	µM	8.74	mM	*Nasemann et al. (2018)*
Vanuatu back-arc	Nifonea-4	basaltic-trachyandesitic	77-06	0 for concs, 14.9 mM for isotopes	7380	µM	**-0.50**	inc dregs	2100	µM	6.6	mM	*Nasemann et al. (2018)*
Vanuatu back-arc	Nifonea-5	basaltic-tracyandesitic	77-10	0 for concs, 3.8 mM for isotopes	677	µM	**-0.53**	inc dregs	100	µM	6.7	mM	*Nasemann et al. (2018)*
Mid-Atlantic Ridge	Rainbow	ultramafic	442-4	0 for conc; 6.03 mmol/kg for isotopes	9.5	mmol/kg	**-0.13**	excl dregs	865	umol/kg	1	mM	*Severmann et al. (2004)*
Mid-Atlantic Ridge	Rainbow	ultramafic	442-6	0 for conc; 8.61 mmol/kg for isotopes	9.5	mmol/kg	**-0.15**	excl dregs	865	umol/kg	1	mM	*Severmann et al. (2004)*
Mid-Atlantic Ridge	TAG	basalt	431	NA	5	mM	**-0.15**	excl dregs	730	µM	>6	mM	*Severmann et al. (2004); Chiba et al. (2001)*
Mid-Atlantic Ridge	Lucky Strike	basalt	3114-11	1.62 mmol/kg	916	µmol/kg	**-0.37**	all ex dregs; recalc rel to IRMM	400	umol/kg	4	mmol/kg	*Beard et al. (2003)*

Mid-Atlantic Ridge	Logatchev (Irina vent)	ultramafic	3133-10	4.82 mmol/kg	2500	µM	**-0.12**	all ex dregs; recalc rel to IRMM	330	umol/kg	0.8	mM	*Beard et al. (2003); Charlou et al. (2002)*
5°S Mid-Atlantic Ridge	Turtle Pits (Two Boats)	basalt	12-ROV-5	0 for concs, 2.8 mM for isotopes	3984	µM	**-0.21**	inc dregs	487	µM	4.2	mM	*Bennett et al. (2009)*
5°S Mid-Atlantic Ridge	Comfortless Cove (Sisters Peak)	basalt	20-ROV-6	0 for concs, 7.4 mM for isotopes	3380	µM	**-0.45**	inc dregs	704	µM	8.31	mM	*Bennett et al. (2009)*
East Scotia Ridge	E2 (DH)	basalt	NA	1.64 mM	988	µM	**-0.28**	inc dregs	2020	µM	6.7	mM	*Klar et al. (2017)*
East Scotia Ridge	E9N (B&W)	basalt	NA	0.59 mM	548	µM	**-0.30**	inc dregs	202	µM	9.5	mM	*Klar et al. (2017)*

NA = not available.

A.5 Literature data for Fe isotope compositions in hydrothermal plumes from contrasting types of hydrothermal systems

Study area	Vent site or location	Sample ID or station ID	Depth (m)	δ^{56}dFe (‰)	dFe (nM)	dMn (nM)	BP dilution factor	Source	Vent fluid Fe/H_2S	Fe(II) half-life (h)	Source
East Scotia Ridge	E2	3-01	2586	**-0.88**	36.1	348	1.5	*Klar et al. (2017)*	0.1	1.5	*James et al. (2014)*
East Scotia Ridge	E2	3-06	2574	**-1.19**	83.5	525	1.0	*Klar et al. (2017)*	0.1	1.5	*James et al. (2014)*
East Scotia Ridge	E2	3-07	2372	**-0.75**	20.2	112	4.7	*Klar et al. (2017)*	0.1	1.5	*James et al. (2014)*
East Scotia Ridge	E2	3-11	2277	**-0.69**	30.9	147	3.6	*Klar et al. (2017)*	0.1	1.5	*James et al. (2014)*
East Scotia Ridge	E2	5-01	2567	**-1.10**	31.6	354	1.5	*Klar et al. (2017)*	0.1	1.5	*James et al. (2014)*
East Scotia Ridge	E2	7-02	2272	**-0.43**	12.1	56	9.3	*Klar et al. (2017)*	0.1	1.5	*James et al. (2014)*
East Scotia Ridge	E2	7-11	2272	**-0.66**	14.3	98	5.4	*Klar et al. (2017)*	0.1	1.5	*James et al. (2014)*
East Scotia Ridge	E2	7-13	2272	**-0.56**	18.0	58	9.0	*Klar et al. (2017)*	0.1	1.5	*James et al. (2014)*
East Scotia Ridge	E2	7-17	2272	**-0.29**	13.1	73	7.2	*Klar et al. (2017)*	0.1	1.5	*James et al. (2014)*
East Scotia Ridge	E9N	424-04	2382	**-0.23**	14.0	27	1.3	*Klar et al. (2017)*	0.1	1.5	*James et al. (2014)*
East Scotia Ridge	E9N	424-07	2385	**-0.76**	23.0	35	1.0	*Klar et al. (2017)*	0.1	1.5	*James et al. (2014)*
East Scotia Ridge	E9N	424-10	2144	**-0.29**	7.3	6	5.6	*Klar et al. (2017)*	0.1	1.5	*James et al. (2014)*
East Scotia Ridge	E9N	424-14	2146	**-0.21**	10.9	11	3.3	*Klar et al. (2017)*	0.1	1.5	*James et al. (2014)*
East Scotia Ridge	E2	43-1	2609	**-0.65**	66	624	18.2	*Lough et al. (2017)*	0.1	1.5	*James et al. (2014)*
East Scotia Ridge	E2	43-2	2609	**1.89**	79	917	12.4	*Lough et al. (2017)*	0.1	1.5	*James et al. (2014)*
East Scotia Ridge	E2	43-4	2608	**-1.98**	68	1046	10.9	*Lough et al. (2017)*	0.1	1.5	*James et al. (2014)*
East Scotia Ridge	E2	43-5	2590	**-1.40**	450	2204	5.2	*Lough et al. (2017)*	0.1	1.5	*James et al. (2014)*
East Scotia Ridge	E2	43-5	2590	**-1.58**	449	2204	5.2	*Lough et al. (2017)*	0.1	1.5	*James et al. (2014)*
East Scotia Ridge	E2	45-10	2604	**-0.72**	49	626	18.2	*Lough et al. (2017)*	0.1	1.5	*James et al. (2014)*
East Scotia Ridge	E2	45-2	2605	**-0.50**	1174	4352	2.6	*Lough et al. (2017)*	0.1	1.5	*James et al. (2014)*
East Scotia Ridge	E2	45-3	2605	**-0.74**	1179	4472	2.5	*Lough et al. (2017)*	0.1	1.5	*James et al. (2014)*
East Scotia Ridge	E2	45-5	2605	**-0.58**	1087	3824	3.0	*Lough et al. (2017)*	0.1	1.5	*James et al. (2014)*

East Scotia Ridge	E2	45-6	2605	**-1.06**	369	1698	6.7	*Lough et al. (2017)*	0.1	1.5	*James et al. (2014)*
East Scotia Ridge	E2	45-7	2605	**-0.69**	365	1804	6.3	*Lough et al. (2017)*	0.1	1.5	*James et al. (2014)*
East Scotia Ridge	E2	45-8	2605	**-0.76**	996	3807	3.0	*Lough et al. (2017)*	0.1	1.5	*James et al. (2014)*
East Scotia Ridge	E2	45-9	2605	**-1.73**	175	1312	8.7	*Lough et al. (2017)*	0.1	1.5	*James et al. (2014)*
East Scotia Ridge	E2	ROV-1	2595	**-0.41**	9336	11375	1.0	*Lough et al. (2017)*	0.1	1.5	*James et al. (2014)*
East Scotia Ridge	E2	ROV-2	2595	**-0.13**	7297	9293	1.2	*Lough et al. (2017)*	0.1	1.5	*James et al. (2014)*
East Scotia Ridge	E2	ROV-3	2588	**-2.39**	416	1440	7.9	*Lough et al. (2017)*	0.1	1.5	*James et al. (2014)*
East Scotia Ridge	E2	ROV-5	2585	**-1.35**	181	1118	10.2	*Lough et al. (2017)*	0.1	1.5	*James et al. (2014)*
Vanuatu back-arc	Nifonea	30-1500	1500	**-0.19**	8.6	NA	NA	*Nasemann et al. (2018)*	0.5	1.1	*Nasemann et al. (2018)*
Vanuatu back-arc	Nifonea	30-1550	1550	**-0.73**	9.4	NA	NA	*Nasemann et al. (2018)*	0.5	1.1	*Nasemann et al. (2018)*
Vanuatu back-arc	Nifonea	30-1600	1600	**-0.32**	6.8	NA	NA	*Nasemann et al. (2018)*	0.5	1.1	*Nasemann et al. (2018)*
Vanuatu back-arc	Nifonea	30-1650	1650	**-0.16**	9.8	NA	NA	*Nasemann et al. (2018)*	0.5	1.1	*Nasemann et al. (2018)*
Vanuatu back-arc	Nifonea	30-1700	1700	**-0.28**	10.2	NA	NA	*Nasemann et al. (2018)*	0.5	1.1	*Nasemann et al. (2018)*
Vanuatu back-arc	Nifonea	79-1500	1500	**-0.18**	3.9	NA	NA	*Nasemann et al. (2018)*	0.5	1.1	*Nasemann et al. (2018)*
Vanuatu back-arc	Nifonea	79-1550	1550	**-0.31**	3.4	NA	NA	*Nasemann et al. (2018)*	0.5	1.1	*Nasemann et al. (2018)*
Vanuatu back-arc	Nifonea	79-1575	1575	**-0.52**	16.6	NA	NA	*Nasemann et al. (2018)*	0.5	1.1	*Nasemann et al. (2018)*
Vanuatu back-arc	Nifonea	79-1600	1600	**-0.32**	9.0	NA	NA	*Nasemann et al. (2018)*	0.5	1.1	*Nasemann et al. (2018)*
Vanuatu back-arc	Nifonea	79-1625	1625	**-0.42**	10.2	NA	NA	*Nasemann et al. (2018)*	0.5	1.1	*Nasemann et al. (2018)*
Loihi Seamount	Pele's Pit	J2-316-N1	bottom seawater	**-1.24**	230	31	NA	*Rouxel et al. (2018)*	27	12	*Glazer & Rouxel. (2009)*
Loihi Seamount	Pele's Pit	J2-315-N1	bottom seawater	**-0.83**	13	4	NA	*Rouxel et al. (2018)*	27	12	*Glazer & Rouxel. (2009)*
Loihi Seamount	Pele's Pit	J2-316-N2	bottom seawater	**-0.50**	70	63	NA	*Rouxel et al. (2018)*	27	12	*Glazer & Rouxel. (2009)*
Mid-Atlantic Ridge	TAG	Station 16	2999	**-0.13**	2.9	1.1	19.1	*Conway & John (2014)*	1.5	0.5	*Field & Sherrell (2000)*
Mid-Atlantic Ridge	TAG	Station 16	3252	**-1.01**	68.4	16.5	1.2	*Conway & John (2014)*	1.5	0.5	*Field & Sherrell (2000)*
Mid-Atlantic Ridge	TAG	Station 16	3275	**-0.92**	47.7	11.4	1.7	*Conway & John (2014)*	1.5	0.5	*Field & Sherrell (2000)*
Mid-Atlantic Ridge	TAG	Station 16	3330	**-1.13**	37.1	16.9	1.2	*Conway & John (2014)*	1.5	0.5	*Field & Sherrell (2000)*
Mid-Atlantic Ridge	TAG	Station 16	3342	**-1.35**	55.7	19.6	1.0	*Conway & John (2014)*	1.5	0.5	*Field & Sherrell (2000)*

Mid-Atlantic Ridge	TAG	Station 16	3420	**-0.94**	51.1	15.7	1.2	*Conway & John (2014)*	1.5	0.5	*Field & Sherrell (2000)*
Mid-Atlantic Ridge	TAG	Station 16	3587	**0.02**	3.8	0.5	44.1	*Conway & John (2014)*	1.5	0.5	*Field & Sherrell (2000)*
East Pacific Rise	15° S	Station 18	2201	**0.38**	0.6	0.3	64.7	*Fitzsimmons et al. (2017)*	0.4	1.8	*Field & Sherrell (2000); Charlou et al. (1996)*
East Pacific Rise	15° S	Station 18	2251	**0.23**	1.0	0.8	21.7	*Fitzsimmons et al. (2017)*	0.4	1.8	*Field & Sherrell (2000); Charlou et al. (1996)*
East Pacific Rise	15° S	Station 18	2301	**0.08**	1.6	1.4	11.0	*Fitzsimmons et al. (2017)*	0.4	1.8	*Field & Sherrell (2000); Charlou et al. (1996)*
East Pacific Rise	15° S	Station 18	2351	**-0.05**	1.8	2.0	7.5	*Fitzsimmons et al. (2017)*	0.4	1.8	*Field & Sherrell (2000); Charlou et al. (1996)*
East Pacific Rise	15° S	Station 18	2376	**-0.05**	1.1	1.0	15.8	*Fitzsimmons et al. (2017)*	0.4	1.8	*Field & Sherrell (2000); Charlou et al. (1996)*
East Pacific Rise	15° S	Station 18	2426	**-0.26**	5.9	11.8	1.2	*Fitzsimmons et al. (2017)*	0.4	1.8	*Field & Sherrell (2000); Charlou et al. (1996)*
East Pacific Rise	15° S	Station 18	2475	**-0.15**	7.0	10.7	1.4	*Fitzsimmons et al. (2017)*	0.4	1.8	*Field & Sherrell (2000); Charlou et al. (1996)*
East Pacific Rise	15° S	Station 18	2526	**-0.14**	8.1	14.6	1.0	*Fitzsimmons et al. (2017)*	0.4	1.8	*Field & Sherrell (2000); Charlou et al. (1996)*
East Pacific Rise	15° S	Station 18	2610	**-0.19**	8.3	7.7	1.9	*Fitzsimmons et al. (2017)*	0.4	1.8	*Field & Sherrell (2000); Charlou et al. (1996)*
East Pacific Rise	15° S	Station 18	2626	**-0.26**	3.4	3.1	4.8	*Fitzsimmons et al. (2017)*	0.4	1.8	*Field & Sherrell (2000); Charlou et al. (1996)*
East Pacific Rise	15° S	Station 20	2201	**0.15**	1.1	0.5	39.6	*Fitzsimmons et al. (2017)*	0.4	1.8	*Field & Sherrell (2000); Charlou et al. (1996)*
East Pacific Rise	15° S	Station 20	2251	**0.06**	1.7	1.6	9.8	*Fitzsimmons et al. (2017)*	0.4	1.8	*Field & Sherrell (2000); Charlou et al. (1996)*
East Pacific Rise	15° S	Station 20	2301	**0.14**	1.9	2.1	7.1	*Fitzsimmons et al. (2017)*	0.4	1.8	*Field & Sherrell (2000); Charlou et al. (1996)*
East Pacific Rise	15° S	Station 20	2351	**0.16**	2.2	2.9	5.1	*Fitzsimmons et al. (2017)*	0.4	1.8	*Field & Sherrell (2000); Charlou et al. (1996)*
East Pacific Rise	15° S	Station 20	2400	**-0.05**	2.5	3.9	3.8	*Fitzsimmons et al. (2017)*	0.4	1.8	*Field & Sherrell (2000); Charlou et al. (1996)*
East Pacific Rise	15° S	Station 20	2552	**0.05**	2.2	3.5	4.2	*Fitzsimmons et al. (2017)*	0.4	1.8	*Field & Sherrell (2000); Charlou et al. (1996)*
East Pacific Rise	15° S	Station 20	2600	**0.18**	2.1	2.8	5.3	*Fitzsimmons et al. (2017)*	0.4	1.8	*Field & Sherrell (2000); Charlou et al. (1996)*
East Pacific Rise	15° S	Station 20	2700	**0.03**	1.9	2.2	7.0	*Fitzsimmons et al. (2017)*	0.4	1.8	*Field & Sherrell (2000); Charlou et al. (1996)*
East Pacific Rise	15° S	Station 20	2800	**0.06**	1.7	1.5	10.3	*Fitzsimmons et al. (2017)*	0.4	1.8	*Field & Sherrell (2000); Charlou et al. (1996)*
East Pacific Rise	15° S	Station 21	2302	**0.39**	1.6	1.0	15.4	*Fitzsimmons et al. (2017)*	0.4	1.8	*Field & Sherrell (2000); Charlou et al. (1996)*
East Pacific Rise	15° S	Station 21	2401	**0.28**	1.6	0.8	19.6	*Fitzsimmons et al. (2017)*	0.4	1.8	*Field & Sherrell (2000); Charlou et al. (1996)*

East Pacific Rise	15° S	Station 21	2501	**0.32**	1.7	0.8	22.3	*Fitzsimmons et al. (2017)*	0.4	1.8	*Field & Sherrell (2000); Charlou et al. (1996)*
East Pacific Rise	15° S	Station 21	2551	**0.35**	1.7	0.8	22.3	*Fitzsimmons et al. (2017)*	0.4	1.8	*Field & Sherrell (2000); Charlou et al. (1996)*
East Pacific Rise	15° S	Station 21	2700	**0.36**	1.5	0.6	28.0	*Fitzsimmons et al. (2017)*	0.4	1.8	*Field & Sherrell (2000); Charlou et al. (1996)*

NA = not available; units for dFe and dMn concentrations have all been converted to nM.

Appendix B Supporting information for Chapter 3

B.1 Supplementary information for analytical methods

Analysis of dissolved Fe concentration and isotopes

Dissolved Fe concentrations were initially determined at sea using flow injection analysis with chemiluminescence detection (FIA-CL; *Obata et al., 1993*). The sample analyses took place in a laminar flow bench using clean handling techniques within the clean bubble in the main laboratory. These dFe concentrations are not reported in this study, but were used to inform optimum isotope spiking and to estimate the sample volume required for 50-100 ng of Fe in the isotopic analysis.

The Fe isotope compositions of seawater samples were determined using the method adapted from *Lacan et al. (2010)*. The sample pH was adjusted to between 1.7-1.8, and ^{57}Fe-^{58}Fe double spike was added in equi-molar concentration to the sample ~24 h before chemical processing. To fully oxidise Fe(II) to Fe(III) in the sample, 10 µM UpA-grade hydrogen peroxide (H_2O_2, Sigma Aldrich) was added, ~1 h prior to starting the pre-concentration procedure. Samples that have 0.5-2 L volume were pre-concentrated using NTA Superflow resin (~1 mL, in a PFA column). Between uses and before loading a sample, the resin was cleaned with 75 mL 1.5 M HCl and 80 mL MQ. The sample was passed over the resin by gravity flow and the resin was then rinsed with MQ water to remove residual salts. The Fe fraction was eluted with 10 mL of 1.5 M HCl, collected in a cleaned PFA vial (Savillex), and subsequently evaporated on a hotplate and reconstituted in 6 M HCl (with 0.001% H_2O_2).

Fe is further purified from the remaining salts by anion exchange. Approximately 200 µL of pre-cleaned AG-MP1 resin (BioRad) was loaded in handmade micro columns. Each column was cleaned by addition of 1 mL of 2 M HNO_3 and conditioned by addition of 0.2 mL of 6 M HCl (0.001% H_2O_2), before loading the sample in 6 M HCl (0.001% H_2O_2). Matrix elements were eluted with 1 mL of 6 M HCl (0.001% H_2O_2). Then the Fe fraction was eluted with 1 mL of 1 M

HCl into a clean Savillex vial, and was dried down gently and re-dissolved in 0.3 M HNO_3.

Analysis of dissolved Cr concentration and isotopes

Dissolved Cr concentrations were initially determined using newly developed $Mg(OH)_2$ co-precipitation method (*Moos and Boyle et al., 2019; Rickli et al., 2019*). Approximately 50 mL sub-sample was transferred into an acid-cleaned centrifuge tube, weighed, and amended with 10 ng ^{53}Cr single spike. Ammonia solution (SpA-grade, Romil) was then added to the sample until $Mg(OH)_2$ forms. For 50 mL acidified sub-sample (pH ~1.7), ~500 µL concentrated ammonia would be required; it is advisable to keep the size of $Mg(OH)_2$ pellet as small as possible. After centrifugation and removal of the supernatant, the Cr was collected as a precipitate and re-dissolved in 5 mL of 0.45 M HNO_3. Cr concentrations of the samples were derived by isotope dilution, based on the $^{52}Cr/^{53}Cr$ ratio of the sample/spike mixture measured by inductively coupled plasma mass spectrometry (ICP-MS; Thermo Scientific Element).

The Cr isotope compositions of seawater samples were determined using the method adapted from *Bonnand et al. (2013)*. Samples of 1-2 L volume were amended with ^{50}Cr-^{54}Cr double spike to achieve optimal target isotope ratios (*Goring-Harford et al., 2018*) and were left to equilibrium for ~24 h. The sample pH was then adjusted to pH 8-9 to facilitate precipitation of Cr. A freshly prepared suspended precipitate of Fe(II) hydroxide, made by addition of ammonia to a fresh ammonium Fe(II) sulfate solution, was added to the samples (10 mL L^{-1} seawater), allowing oxidation of the Fe(II) hydroxide and reduction of any remaining Cr(VI). The Fe(III) hydroxide scavenges the Cr(III), resulting in quantitative precipitation of dissolved Cr in the sample (*Connelly et al., 2006*).

The precipitate was separated from the solution via vacuum filtration through pre-cleaned PTFE membrane filters (1 µm, Millipore Omnipore), and was subsequently leached from the filters using 6 M HCl before being dried down and taken up in 6 mL of 7 M HCl. The Cr was first separated from the Fe by anion exchange (~2 mL of Bio Rad AG1-X8 resin loaded in a Bio Rad Poly-Prep column). The resin was extensively cleaned with concentrated HNO_3, 0.5 M HCl and concentrated HCl, and was pre-conditioned with 7M HCl. The sample was loaded in 6 mL of 7M HCl on to the resin. The eluent was collected, dried down and then reconstituted in 6 mL

of 0.5 M HCl. The column was cleaned with 0.5 M HCl to remove Fe and stored in 0.5 M HCl.

The residual salts of the eluent were further removed by cation exchange (2.9 mL of BioRad AG 50W-X12 resin loaded in a 30 mL PFA Savillex column). The resin was cleaned with 10 mL of 8 M HNO_3, 30 mL of 6 M HCL and 30 mL of MQ water, and was pre-conditioned with 12 mL of 0.5 M HCl. The sample was loaded in 6 mL of 0.5 M HCl and the Cr was immediately eluted and collected in a 15 mL Savillex vial. Additional 4 mL of 0.5 M HCl was added to the column and collected. The column was cleaned with 6M HCl to remove the remaining cations and stored in 0.5 M HCl. The Cr fraction was evaporated to dryness and was treated with 50µL concentrated H_2O_2 and HNO_3, respectively, to oxidise any remaining organic material, before being dried down once again and re-dissolved in 0.45 M HNO_3.

Isotopic analysis

The isotopic compositions of Fe and Cr were determined by multicollector inductively coupled plasma mass spectrometry (MC-ICP-MS; Thermo Fisher Neptune Plus) at the University of Southampton, using methods similar to those described in *Klar et al. (2018)* and *Goring-Harford et al. (2018)*. The final Fe and Cr isotope values are reported in delta notation relative to international isotope standards and expressed as:

$$\delta^{56}Fe\ (‰) = [(^{56}Fe/^{54}Fe)_{sample}/(^{56}Fe/^{54}Fe)_{IRMM\text{-}14} - 1] \times 1000 \quad (1)$$

$$\delta^{53}Cr\ (‰) = [(^{53}Cr/^{52}Cr)_{sample}/(^{53}Cr/^{52}Cr)_{NBS979} - 1] \times 1000 \quad (2)$$

Purified samples with 50-100 ppb Fe were introduced to the plasma using an Apex-Q desolvating system and signals from ^{54}Fe, ^{56}Fe, ^{57}Fe, ^{58}Fe and ^{53}Cr, ^{60}Ni were quantified. Analysis was carried out in high-resolution mode and the instrument was carefully tuned to give sufficient mass resolution (>8000), before running a sequence that consisted of analysis of the reference material (IRMM), the internal Fe standard (ETH), Sample 1, Sample 2, and so on. Each sample analysis for Fe consisted of 50 repeat measurements.

Purified samples with 50-100 ppb Cr were introduced using an Aridus 3 desolvator and signals from ^{50}Cr, ^{52}Cr, ^{53}Cr, ^{54}Cr and ^{49}Ti, ^{51}V, ^{56}Fe were quantified. Medium resolution setting was used and mass resolution >5000 was achieved. Each analytical sequence for Cr consisted of

repeating analyses of the NBS979 standard with every three samples. Each sample analysis consisted of 100 individual measurements.

Polyatomic interferences were avoided by making measurements on peak shoulders. The typical ion beam size was ~0.1 V ppb^{-1} for ^{56}Fe and 0.15-0.24 V ppb^{-1} for ^{52}Cr. The mean signal intensity of a blank solution that was analysed before and after each sample/standard was subtracted. The sample $\delta^{56}Fe$ or $\delta^{53}Cr$ values were obtained using an iterative deconvolving procedure (*Albarède and Beard, 2004*). The raw data were corrected for instrumental mass bias and, for Cr, the total procedural blank contribution. The Cr blank mainly came from the Fe precipitate and constituted <10% of the total Cr analysed (blank $\delta^{53}Cr$ = –0.16‰).

In addition, the Fe or Cr concentration of each sample was determined simultaneously with the isotope ratios using isotope dilution equations, based on the known sample volume and the quantity of added spike. The results are in consistency with those derived from FIA-CL (for Fe) or $Mg(OH)_2$ co-precipitation (for Cr) methods.

Analyses of the ETH iron isotope standard and the NBS979 chromium isotope standard gave $\delta^{56}Fe$ = 0.50 ± 0.10‰ (2SD, n=113) and $\delta^{53}Cr$ = 0.00 ± 0.05‰ (2SD, n=49) respectively, showing agreement with the consensus values (ETH $\delta^{56}Fe$ = 0.52 ± 0.07‰, *Klar et al., 2018*; NBS979 $\delta^{53}Cr$ = 0.00 ± 0.04‰, *Goring-Harford et al., 2018*). The precision and accuracy of the above methods were further assessed through the analysis of (1) Trace metal free seawater doped with hematite (HEM) Fe isotope standard, (2) Black Sea Fe intercomparison 'anoxic' sample, and (3) OSIL Atlantic salinity standard seawater. These results are summarised in the main text (Table 3-1).

B.2 Fe data for all samples measured in this study

CTD no.	ROS no.	Depth (m)	δ^{56}Fe (‰)					δ^{56}Fe (‰)		dFe (nM)
			(1)	2SE	*(2)*	2SE	Average	*	2SE	
TAG (Station 35/38)										
78	24	20	0.58	0.08	NA	NA	**0.58**	NA	NA	**0.86**
78	22	100	0.67	0.05	NA	NA	**0.67**	NA	NA	**0.88**
78	18	250	0.59	0.06	NA	NA	**0.59**	0.61	0.05	**0.42**
78	14	800	0.45	0.06	NA	NA	**0.45**	NA	NA	**0.78**
78	9	1500	0.56	0.04	NA	NA	**0.56**	NA	NA	**0.69**
78	7	1999	0.36	0.08	0.29	0.03	**0.33**	NA	NA	**1.10**
76	19	3100	0.59	0.08	0.64	0.05	**0.61**	0.47	0.04	**2.07**
76	17	3236	-1.77	0.04	-1.89	0.09	**-1.83**	-2.07	0.03	**55.21**
76	12	3322	-1.68	0.03	-1.64	0.04	**-1.66**	-1.76	0.03	**64.36**
76	8	3350	-0.59	0.03	-0.60	0.04	**-0.59**	NA	NA	**68.06**
76	7	3429	-0.34	0.05	-0.36	0.07	**-0.35**	NA	NA	**26.99**
76	3	3544	0.09	0.05	NA	NA	**0.09**	NA	NA	**1.52**
76	2	3660	0.47	0.05	NA	NA	**0.47**	NA	NA	**1.56**
TAG Close North (Station 36)										
80	23	50	0.39	0.04	NA	NA	**0.39**	0.38	0.11	**0.76**
80	21	125	0.53	0.03	NA	NA	**0.53**	0.70	0.07	**0.38**
80	18	401	0.72	0.09	NA	NA	**0.72**	NA	NA	**0.43**
80	16	800	0.43	0.11	0.47	0.07	**0.45**	NA	NA	**0.59**
80	14	1399	0.33	0.06	NA	NA	**0.33**	0.36	0.04	**0.89**
80	12	1999	0.48	0.06	NA	NA	**0.48**	NA	NA	**0.67**
80	11	2500	0.17	0.05	NA	NA	**0.17**	NA	NA	**1.02**
80	9	3001	-0.44	0.06	NA	NA	**-0.44**	NA	NA	**3.20**
80	7	3299	-0.35	0.04	-0.40	0.06	**-0.38**	NA	NA	**2.88**
80	6	3401	-0.40	0.06	-0.46	0.04	**-0.43**	NA	NA	**1.96**
80	4	3600	0.05	0.05	-0.05	0.07	**0.00**	NA	NA	**1.69**
80	2	3899	0.05	0.03	NA	NA	**0.05**	NA	NA	**1.49**
TAG Close West (Station 30)										
65	24	20	0.22	0.05	NA	NA	**0.22**	NA	NA	**0.66**
65	18	181	0.46	0.11	NA	NA	**0.46**	NA	NA	**0.24**
65	13	796	0.39	0.03	NA	NA	**0.39**	NA	NA	**0.52**
65	11	1516	0.54	0.05	NA	NA	**0.54**	NA	NA	**0.63**
65	9	2226	0.41	0.05	NA	NA	**0.41**	NA	NA	**0.78**
65	7	2429	0.12	0.04	NA	NA	**0.12**	NA	NA	**0.93**
65	6	2531	0.10	0.05	NA	NA	**0.10**	NA	NA	**0.82**
65	5	2634	0.33	0.05	NA	NA	**0.33**	NA	NA	**0.73**
65	4	2735	0.26	0.04	NA	NA	**0.26**	NA	NA	**1.22**
65	3	2838	0.14	0.04	NA	NA	**0.14**	NA	NA	**0.87**
65	1	3113	-0.04	0.04	NA	NA	**-0.04**	NA	NA	**1.25**
TAG 250 km West (Station 28)										

61	9	2100	0.36	0.07	0.53	0.07	**0.44**	NA	NA	**0.89**
61	7	3000	0.27	0.05	0.31	0.05	**0.29**	NA	NA	**0.95**
61	5	3799	0.28	0.05	0.42	0.09	**0.35**	NA	NA	**0.64**
61	4	3901	0.45	0.05	NA	NA	**0.45**	NA	NA	**0.57**
61	3	4000	0.16	0.08	0.35	0.07	**0.25**	NA	NA	**0.61**
61	1	4222	0.20	0.07	0.31	0.06	**0.25**	NA	NA	**0.86**
Rainbow (Station 16/39)										
43	17	768	0.60	0.06	NA	NA	**0.60**	NA	NA	**2.22**
36	13	1300	0.48	0.03	0.40	0.04	**0.44**	NA	NA	**1.60**
43	12	1896	-0.07	0.07	NA	NA	**-0.07**	NA	NA	**4.45**
36	6	2001	-5.65	0.05	-5.67	0.04	**-5.66**	-5.24	0.04	**59.62**
36	5	2051	-5.06	0.04	-5.02	0.06	**-5.04**	NA	NA	**40.51**
36	4	2072	-6.13	0.05	-6.12	0.09	**-6.12**	NA	NA	**58.20**
36	3	2108	-6.92	0.04	-6.97	0.05	**-6.94**	-6.95	0.05	**53.08**
36	2	2200	0.36	0.11	NA	NA	**0.36**	NA	NA	**2.31**
36	1	2280	0.38	0.06	NA	NA	**0.38**	NA	NA	**1.56**
Rainbow (Station 16/39)										
43	4	2252	-5.84	0.09	NA	NA	**-5.84**	NA	NA	**13.55**
43	2	2261	-4.77	0.09	NA	NA	**-4.77**	NA	NA	**11.00**
Rainbow Bonus South (Station 17 - not presented)										
38	13	1501	0.50	0.05	NA	NA	**0.50**	NA	NA	**1.45**
38	12	1900	0.32	0.04	NA	NA	**0.32**	0.43	0.04	**2.78**
38	9	2002	0.01	0.08	NA	NA	**0.01**	NA	NA	**2.15**
38	7	2101	0.28	0.05	NA	NA	**0.28**	0.37	0.03	**3.56**
Rainbow Close North (Station 18)										
40	24	18	0.62	0.12	NA	NA	**0.62**	0.75	0.12	**0.19**
40	21	80	0.69	0.07	NA	NA	**0.69**	0.71	0.08	**0.24**
40	18	164	0.35	0.08	NA	NA	**0.35**	NA	NA	**0.28**
40	16	499	0.42	0.09	NA	NA	**0.42**	0.34	0.07	**0.48**
40	14	719	0.46	0.06	NA	NA	**0.46**	NA	NA	**0.74**
40	11	1601	0.58	0.10	NA	NA	**0.58**	NA	NA	**1.17**
40	9	1799	0.14	0.09	NA	NA	**0.14**	NA	NA	**2.37**
40	8	1950	0.19	0.08	NA	NA	**0.19**	NA	NA	**3.57**
40	7	2050	0.14	0.07	NA	NA	**0.14**	NA	NA	**5.76**
40	6	2099	-0.08	0.06	NA	NA	**-0.08**	NA	NA	**2.98**
40	3	2453	-0.14	0.07	NA	NA	**-0.14**	NA	NA	**2.29**
40	1	2632	-0.01	0.08	NA	NA	**-0.01**	NA	NA	**2.21**
Rainbow Close East (Station 12)										
27	23	43	0.20	0.06	NA	NA	**0.20**	0.37	0.07	**0.13**
27	20	107	0.27	0.10	NA	NA	**0.27**	NA	NA	**0.20**
27	18	401	0.37	0.05	NA	NA	**0.37**	NA	NA	**0.43**
27	15	701	0.58	0.04	NA	NA	**0.58**	NA	NA	**0.62**
27	13	900	0.38	0.04	NA	NA	**0.38**	NA	NA	**0.75**
27	12	1200	0.26	0.08	NA	NA	**0.26**	NA	NA	**0.80**
27	10	1751	0.25	0.05	0.21	0.05	**0.23**	NA	NA	**1.87**
27	8	2000	0.08	0.06	-0.06	0.04	**0.01**	NA	NA	**2.84**

27	6	2100	-0.11	0.04	-0.11	0.04	**-0.11**	NA	NA	**3.54**
27	5	2150	-0.06	0.06	-0.11	0.05	**-0.09**	NA	NA	**3.00**
27	2	2349	0.00	0.03	-0.01	0.04	**0.00**	NA	NA	**3.32**
Rainbow 200 km East (Station 11)										
25	20	148	0.08	0.06	NA	NA	**0.08**	NA	NA	**0.19**
25	13	929	0.19	0.04	0.28	0.09	**0.23**	NA	NA	**0.71**
25	11	1399	0.26	0.05	NA	NA	**0.26**	NA	NA	**0.66**
25	8	1798	0.24	0.04	NA	NA	**0.24**	NA	NA	**0.64**
25	6	2403	0.38	0.04	NA	NA	**0.38**	NA	NA	**0.66**
25	3	2747	0.32	0.04	NA	NA	**0.32**	NA	NA	**0.61**
25	1	2868	0.69	0.10	NA	NA	**0.69**	NA	NA	**0.60**

Numbers *(1), (2)* represent two replicate MC-ICP-MS measurements on the same sample solution. * means replicate analysis by separate chemical extractions of samples from the same bottle or the same water depth (not included in calculating the average δ^{56}Fe value that is presented in the main text). 2SE is the internal error of each MC-ICP-MS measurement and reflects the analytical uncertainty. The external reproducibility (2SD) for δ^{56}Fe is ± 0.10‰ based on the long-term precision of the iron isotope standard (ETH). NA = not available. Depths for hydrothermal plumes and particle-rich plumes are highlighted.

B.3 Cr data for all samples measured in this study

CTD no.	ROS no.	Depth (m)	δ^{53}Cr (‰)							Cr (nM)
			(1)	2SE	*(2)*	2SE	*(3)*	2SE	Average	Average
TAG (Station 35/38)										
78	22	100	1.31	0.01	1.31	0.01	NA	NA	**1.31**	**2.34**
78	18	250	1.30	0.02	1.33	0.02	NA	NA	**1.32**	**2.31**
78	14	800	1.25	0.01	1.22	0.01	NA	NA	**1.23**	**2.45**
78	9	1500	1.19	0.02	1.21	0.01	NA	NA	**1.20**	**2.51**
78	7	1999	1.09	0.01	1.15	0.02	NA	NA	**1.12**	**2.45**
76	18	3194	1.11	0.03	1.07	0.02	NA	NA	**1.09**	**2.69**
76	17	3236	1.21	0.02	1.24	0.02	NA	NA	**1.23**	**2.62**
76	13	3314	1.18	0.01	1.24	0.02	NA	NA	**1.21**	**2.63**
76	12	3322	1.17	0.02	1.18	0.02	NA	NA	**1.18**	**2.71**
76	11	3334	1.16	0.02	1.15	0.02	1.09	0.03	**1.13**	**2.64**
76	8	3350	1.18	0.01	1.20	0.02	NA	NA	**1.19**	**2.70**
76	2	3601	1.08	0.01	1.15	0.01	NA	NA	**1.11**	**2.78**
Rainbow (Station 16/39)										
43	23	60	1.34	0.01	1.35	0.01	NA	NA	**1.34**	**2.28**
43	19	353	1.15	0.02	1.22	0.02	NA	NA	**1.19**	**2.27**
43	17	768	1.27	0.02	1.23	0.02	NA	NA	**1.25**	**2.37**
43	16	978	1.27	0.02	1.24	0.07	NA	NA	**1.25**	**2.40**
43	14	1601	0.97	0.01	0.95	0.01	NA	NA	**0.96**	**2.40**
43	12	1896	1.31	0.02	1.29	0.02	NA	NA	**1.30**	**2.39**
36	5	2051	1.86	0.03	1.88	0.03	NA	NA	**1.87**	**2.13**
36	4	2072	1.41	0.02	1.63	0.02	NA	NA	**1.52**	**2.23**
36	3	2108	1.72	0.02	1.67	0.03	NA	NA	**1.69**	**2.34**
36	2	2200	1.30	0.02	1.31	0.02	NA	NA	**1.30**	**2.37**
43	1	2283	1.24	0.04	1.22	0.03	NA	NA	**1.23**	**2.37**

Numbers *(1)*, *(2)*, *(3)* represent three replicate MC-ICP-MS measurements on the same sample solution. 2SE is the internal error of each MC-ICP-MS measurement and reflects the analytical uncertainty. The external reproducibility (2SD) for δ^{53}Cr is ± 0.05‰ based on the long-term precision of the chromium isotope standard (NBS979). NA = not available. Hydrothermal plume depths are highlighted.

B.4 Fe isotope compositions ($\delta^{56}Fe$) of dFe in seawater samples from 8 stations of the GA13 transect

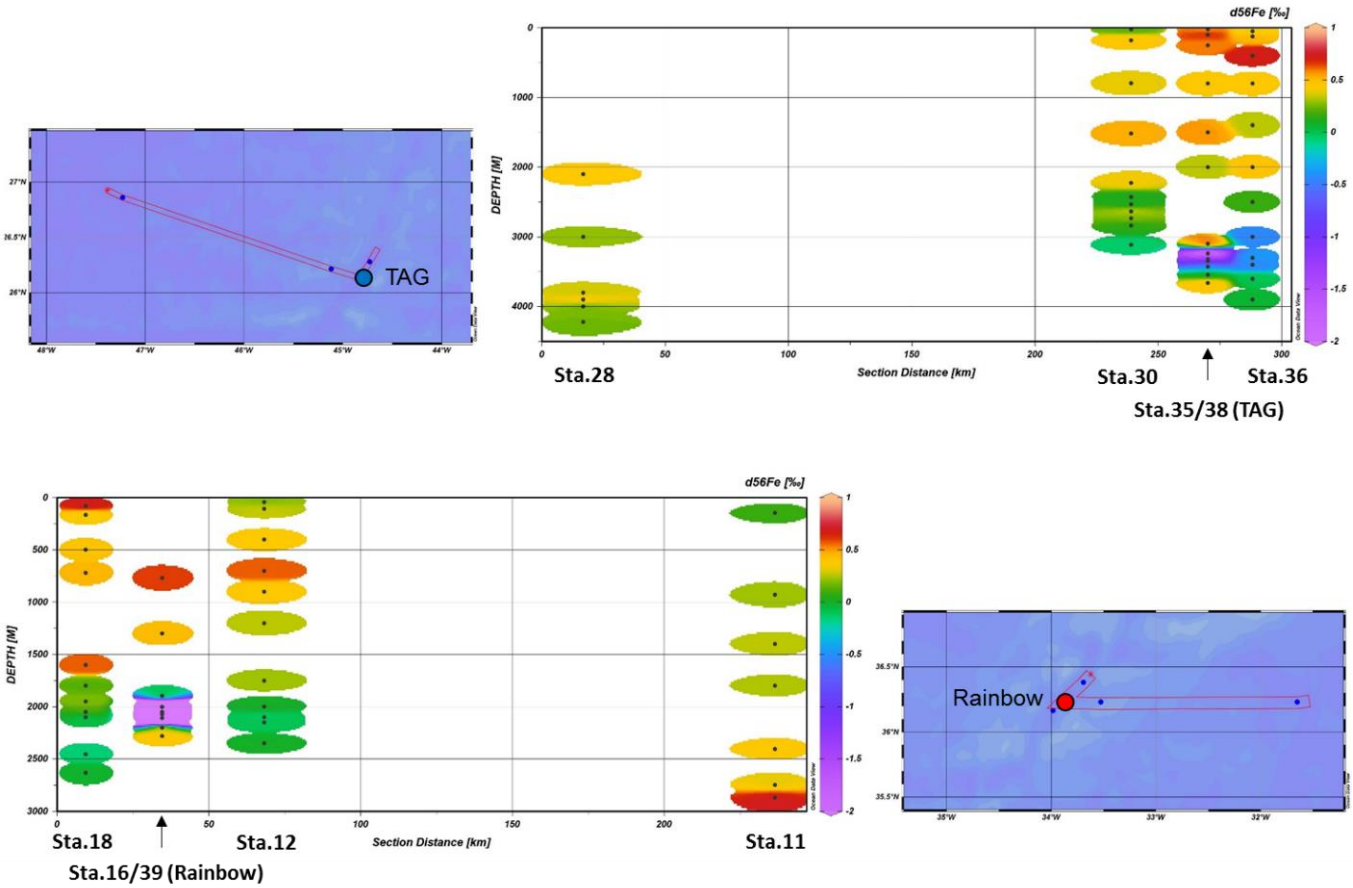

Data are available and can be found in Table B2. Figure was made using Ocean Data View (Schlitzer, 2009).

Appendix C Supporting information for Chapter 4

C.1 Cr data for all seawater samples measured in this study

Depth	δ^{53}Cr (‰)							Cr (nM)	Salinity	O_2
(m)	*(1)*	2SE	*(2)*	2SE	*(3)*	2SE	Average	Average		(μmol/kg)
Station 1										
40	1.44	0.01	1.29	0.03	NA	NA	**1.36**	**2.31**	37.2	207
100	1.33	0.02	1.33	0.01	NA	NA	**1.33**	**2.19**	37.2	205
251	1.35	0.02	1.37	0.02	NA	NA	**1.36**	**2.06**	36.6	183
350	1.33	0.03	1.33	0.02	NA	NA	**1.33**	**2.15**	36.5	180
651	1.27	0.02	1.30	0.02	NA	NA	**1.29**	**2.26**	35.5	145
1001	1.27	0.02	1.24	0.02	NA	NA	**1.26**	**2.22**	35.0	160
1752	1.25	0.02	1.28	0.02	NA	NA	**1.27**	**2.22**	35.0	246
3504	1.16	0.02	1.18	0.02	NA	NA	**1.17**	**2.34**	34.9	252
5006	1.13	0.02	1.12	0.01	NA	NA	**1.12**	**2.50**	34.8	242
Station 4										
26	1.33	0.01	1.30	0.01	NA	NA	**1.32**	**2.28**	37.6	200
60	1.27	0.01	1.30	0.01	NA	NA	**1.29**	**2.48**	37.4	210
140	1.39	0.01	1.39	0.01	NA	NA	**1.39**	**2.15**	37.2	193
180	1.35	0.01	1.35	0.02	NA	NA	**1.35**	**2.16**	36.9	181
300	1.35	0.01	1.37	0.02	NA	NA	**1.36**	**1.89**	36.4	174
401	1.28	0.01	1.29	0.01	NA	NA	**1.28**	**1.84**	36.0	150
1001	1.30	0.02	1.34	0.02	NA	NA	**1.32**	**2.29**	35.0	151
2002	1.41	0.01	1.42	0.02	NA	NA	**1.41**	**2.00**	35.0	234
3323	1.25	0.02	1.25	0.02	NA	NA	**1.25**	**2.49**	34.9	239
3343	1.20	0.02	1.19	0.02	NA	NA	**1.20**	**2.48**	34.9	239
3505	1.04	0.04	1.08	0.04	NA	NA	**1.06**	**2.57**	34.9	239
Station 6										
15	1.36	0.01	1.34	0.02	1.34	0.02	**1.34**	**2.25**	37.3	202
80	1.44	0.02	1.41	0.02	1.40	0.02	**1.42**	**2.19**	37.3	217
120	1.42	0.02	1.39	0.02	NA	NA	**1.40**	**2.16**	37.2	208
180	1.40	0.02	1.37	0.02	1.39	0.02	**1.39**	**2.10**	36.8	190
250	1.44	0.02	1.38	0.02	1.38	0.02	**1.40**	**2.12**	36.6	181
350	1.36	0.02	1.39	0.02	NA	NA	**1.38**	**2.04**	36.2	166
550	1.37	0.02	1.33	0.02	NA	NA	**1.35**	**2.16**	35.7	148
701	1.33	0.02	1.34	0.01	NA	NA	**1.33**	**2.35**	35.4	132
901	1.26	0.01	1.22	0.02	NA	NA	**1.24**	**2.12**	35.1	138
1501	1.14	0.02	1.16	0.02	NA	NA	**1.15**	**2.63**	35.1	206
2503	1.27	0.02	1.24	0.01	NA	NA	**1.26**	**2.48**	35.0	232
5005	1.11	0.02	1.11	0.01	NA	NA	**1.11**	**2.51**	34.9	234
5780	1.11	0.02	1.13	0.02	NA	NA	**1.12**	**2.63**	34.9	236

Appendix C

NA = not available. Numbers *(1)*, *(2)*, *(3)* represent three replicate MC-ICP-MS measurements on the same sample solution. 2SE is the internal error of each MC-ICP-MS measurement and reflects the analytical uncertainty (typically between 0.01‰ and 0.04‰). The external reproducibility (2SD) for $\delta^{53}Cr$ is ± 0.05‰ based on the long-term precision of the chromium isotope standard (NBS979).

List of Reference

Abadie, C., Lacan, F., Radic, A., Pradoux, C., Poitrasson, F., 2017. Iron isotopes reveal distinct dissolved iron sources and pathways in the intermediate versus deep Southern Ocean. *Proceedings of the National Academy of Sciences*, 114(5), 858-863.

Achterberg, E.P., van den Berg, C.M., 1997. Chemical speciation of chromium and nickel in the western Mediterranean. *Deep Sea Research Part II: Topical Studies in Oceanography*, 44(3-4), 693-720.

Albarède, F., Beard, B., 2004. Analytical methods for non-traditional isotopes. *Reviews in Mineralogy and Geochemistry*, 55(1), 113-152.

Anbar, A.D., 2004. Iron stable isotopes: beyond biosignatures. *Earth and Planetary Science Letters*, 217(3-4), 223-236.

Anbar, A.D., Jarzecki, A.A., Spiro, T.G., 2005. Theoretical investigation of iron isotope fractionation between $Fe(H_2O)_6^{3+}$ and $Fe(H_2O)_6^{2+}$: implications for iron stable isotope geochemistry. *Geochimica et Cosmochimica Acta*, 69(4), 825-837.

Anderson, R. F., 2020. GEOTRACES: Accelerating Research on the Marine Biogeochemical Cycles of Trace Elements and Their Isotopes. Annual Review of Marine Science, 12(1), annurev-marine-010318-095123. DOI: 10.1146/annurev-marine-010318-095123

Andronikov, A.V., Novak, M., Borodulina, G.S., Efremenko, N.A., Andronikova, I.E., Chesalina, G.L., Levichev, M.A., Subetto, D.A., Sebek, O., Zobkova, M.V., 2019. One river, two streams: chemical and chromium isotopic features of the Neglinka River (Karelia, northwest Russia). *Hydrological Sciences Journal*, 64(8), 974-982.

Artigue, L., Lacan, F., Van Gennip, S., Lohan, M.C., Wyatt, N.J., Woodward, E.M.S., Mahaffey, C., Hopkins, J., Drillet, Y., 2020. Water mass analysis along 22° N in the subtropical North Atlantic for the JC150 cruise (GEOTRACES, GApr08). *Deep Sea Research Part I: Oceanographic Research Papers*, 158. DOI: 10.1016/j.dsr.2020.103230

Bain, D.J. and Bullen, T.D., 2005. Chromium isotope fractionation during oxidation of Cr (III) by manganese oxides. *GeCAS*, 69(10), p.A212.

Bain, D.J., Bullen, T.D., 2005. Chromium isotope fractionation during oxidation of Cr (III) by manganese oxides. *Geochimica et Cosmochimica Acta Supplement*, 69, A212.

Balci, N., Bullen, T.D., Witte-Lien, K., Shanks, W.C., Motelica, M., Mandernack, K.W., 2006. Iron isotope fractionation during microbially stimulated Fe (II) oxidation and Fe (III) precipitation. *Geochimica et Cosmochimica Acta*, 70(3), 622-639.

Ball, J.W. and Nordstrom, D.K., 1998. Critical evaluation and selection of standard state thermodynamic properties for chromium metal and its aqueous ions, hydrolysis species, oxides, and hydroxides. *Journal of Chemical & Engineering Data*, 43(6), 895-918.

Barbeau, K., Rue, E.L., Bruland, K.W., Butler, A., 2001. Photochemical cycling of iron in the surface ocean mediated by microbial iron (III)-binding ligands. *Nature*, 413(6854), 409-413.

Basu, A., Johnson, T.M., 2012. Determination of hexavalent chromium reduction using Cr stable isotopes: isotopic fractionation factors for permeable reactive barrier materials. *Environmental Science & Technology*, 46(10), 5353-5360.

Basu, A., Johnson, T.M., Sanford, R.A., 2014. Cr isotope fractionation factors for Cr(VI) reduction by a metabolically diverse group of bacteria. *Geochimica et Cosmochimica Acta*, 142, 349-361.

Basu, S., Gledhill, M., de Beer, D., Matondkar, S.P., Shaked, Y., 2019. Colonies of marine cyanobacteria Trichodesmium interact with associated bacteria to acquire iron from dust. *Communications Biology*, 2(1), 1-8. DOI: 10.1038/s42003-019-0534-z

Bauer, K.W., Cole, D.B., Asael, D., Francois, R., Calvert, S.E., Poulton, S.W., Planavsky, N.J., Crowe, S.A., 2019. Chromium isotopes in marine hydrothermal sediments. *Chemical Geology*, 529, 119286.

Beard, B.L., Johnson, C.M., Cox, L., Sun, H., Nealson, K.H., Aguilar, C., 1999. Iron isotope biosignatures. *Science*, 285(5435), 1889-1892.

Beard, B.L., Johnson, C.M., Skulan, J.L., Nealson, K.H., Cox, L., Sun, H., 2003. Application of Fe isotopes to tracing the geochemical and biological cycling of Fe. *Chemical Geology*, 195(1-4), 87-117.

Beard, B.L., Johnson, C.M., Von Damm, K.L., Poulson, R.L., 2003. Iron isotope constraints on Fe cycling and mass balance in oxygenated Earth oceans. *Geology*, 31(7), 629-632.

Bennett, S.A., Achterberg, E.P., Connelly, D.P., Statham, P.J., Fones, G.R., German, C.R., 2008. The distribution and stabilisation of dissolved Fe in deep-sea hydrothermal plumes. *Earth and Planetary Science Letters*, 270(3-4), 157-167.

Bennett, S.A., Rouxel, O., Schmidt, K., Garbe-Schönberg, D., Statham, P.J., German, C.R., 2009. Iron isotope fractionation in a buoyant hydrothermal plume, 5 S Mid-Atlantic Ridge. *Geochimica et Cosmochimica Acta*, 73(19), 5619-5634.

Bergquist, B.A., Boyle, E.A., 2006. Iron isotopes in the Amazon River system: Weathering and transport signatures. *Earth and Planetary Science Letters*, 248(1-2), 54-68.

Blowes, D.W., Ptacek, C.J., Jambor, J.L., 1997. In-situ remediation of Cr (VI)-contaminated groundwater using permeable reactive walls: laboratory studies. *Environmental Science & Technology*, 31(12), 3348-3357.

Bonnand, P., James, R., Parkinson, I., Connelly, D., Fairchild, I., 2013. The chromium isotopic composition of seawater and marine carbonates. *Earth and Planetary Science Letters*, 382, 10-20.

Bowie, A.R., Achterberg, E.P., Ussher, S., Worsfold, P.J., 2005. Design of an automated flow injection-chemiluminescence instrument incorporating a miniature photomultiplier tube for monitoring picomolar concentrations of iron in seawater. *Journal of Analytical Methods in Chemistry*, 2005(2), 37-43.

Boyd, P.W., Ellwood, M.J., 2010. The biogeochemical cycle of iron in the ocean. *Nature Geoscience*, 3(10), 675-682.

Boyd, P.W., Jickells, T., Law, C., Blain, S., Boyle, E., Buesseler, K., Coale, K., Cullen, J., De Baar, H., Follows, M., 2007. Mesoscale iron enrichment experiments 1993-2005: Synthesis and future directions. *Science*, 315(5812), 612-617.

Boyle, E.A., Edmond, J.M., Sholkovitz, E.R., 1977a. The mechanism of iron removal in estuaries. *Geochimica et Cosmochimica Acta*, 41(9), 1313-1324.

Boyle, E.A., Sclater, F.R., Edmond, J.M., 1977b. The distribution of dissolved copper in the Pacific. *Earth and Planetary Science Letters*, 37(1), 38-54.

Bruggmann, S., Scholz, F., Klaebe, R.M., Canfield, D.E., Frei, R., 2019. Chromium isotope cycling in the water column and sediments of the Peruvian continental margin. *Geochimica et Cosmochimica Acta*, 257, 224-242.

Bruland, K.W., Lohan, M.C., 2006. Controls of trace metals in seawater. In *The oceans and marine geochemistry* (eds. Elderfield, H., Holland, H.D., Turekian, K.K.), 6, 23-47.

Buerge, I.J., Hug, S.J., 1997. Kinetics and pH dependence of chromium (VI) reduction by iron (II). *Environmental Science & Technology*, 31(5), 1426-1432.

Buerge, I.J., Hug, S.J., 1999. Influence of mineral surfaces on chromium (VI) reduction by iron (II). *Environmental Science & Technology*, 33(23), 4285-4291.

Butler, I.B., Archer, C., Vance, D., Oldroyd, A., Rickard, D., 2005. Fe isotope fractionation on FeS formation in ambient aqueous solution. *Earth and Planetary Science Letters*, 236(1), 430-442.

Campbell, J.A., Yeats, P.A., 1981. Dissolved chromium in the northwest Atlantic Ocean. *Earth and Planetary Science Letters*, 53(3), 427-433.

Campbell, J.A., Yeats, P.A., 1984. Dissolved chromium in the St. Lawrence estuary. *Estuarine, Coastal and Shelf Science*, 19(5), 513-522.

Carazzo, G., Jellinek, A.M., Turchyn, A.V., 2013. The remarkable longevity of submarine plumes: Implications for the hydrothermal input of iron to the deep-ocean. *Earth and Planetary Science Letters*, 382, 66-76.

Charlou, J.L., Donval, J.P., Fouquet, Y., Jean-Baptiste, P., Holm, N., 2002. Geochemistry of high H_2 and CH_4 vent fluids issuing from ultramafic rocks at the Rainbow hydrothermal field (36°14′N, MAR). *Chemical geology*, 191(4), 345-359.

Charlou, J.L., Fouquet, Y., Donval, J.P., Auzende, J.M., Jean-Baptiste, P., Stievenard, M., Michel, S., 1996. Mineral and gas chemistry of hydrothermal fluids on an ultrafast spreading ridge: East Pacific Rise, 17° to 19°S (Naudur cruise, 1993) phase separation processes controlled by volcanic and tectonic activity. *Journal of Geophysical Research: Solid Earth*, 101(B7), 15899-15919.

Charlou, J.L., Fouquet, Y., Donval, J.P., Auzende, J.M., Jean-Baptiste, P., Stievenard, M., Michel, S., 1996. Mineral and gas chemistry of hydrothermal fluids on an ultrafast spreading ridge: East Pacific Rise, 17° to 19°S (Naudur cruise, 1993) phase separation processes controlled by volcanic and tectonic activity. *Journal of Geophysical Research: Solid Earth*, 101(B7), 15899-15919.

Chester, R., Hughes, M.J., 1969. The trace element geochemistry of a North Pacific pelagic clay core. *Deep Sea Research and Oceanographic Abstracts*, 16(6), 639-654.

Chester, R., Murphy, K.J.T., 1990. Metals in the marine atmosphere. In *Heavy metals in the marine environment*, 27-49. CRC Press Boca Raton, FL.

Chiba, H., Masuda, H., Lee, S.Y., Fujioka, K., 2001. Chemistry of hydrothermal fluids at the TAG active mound, MAR 26°N, in 1998. *Geophysical Research Letters*, 28(15), 2919-2922.

Connelly, D.P., Copley, J.T., Murton, B.J., Stansfield, K., Tyler, P.A., German, C.R., Van Dover, C.L., Amon, D., Furlong, M., Grindlay, N., Hayman, N., 2012. Hydrothermal vent fields and chemosynthetic biota on the world's deepest seafloor spreading centre. *Nature Communications*, 3, 620. DOI: 10.1038/ncomms1636

Connelly, D.P., Statham, P.J., Knap, A.H., 2006. Seasonal changes in speciation of dissolved chromium in the surface Sargasso Sea. *Deep Sea Research Part I: Oceanographic Research Papers*, 53(12), 1975-1988.

Conway, T.M., Hamilton, D.S., Shelley, R.U., Aguilar-Islas, A.M., Landing, W.M., Mahowald, N.M., John, S.G., 2019. Tracing and constraining anthropogenic aerosol iron fluxes to the North Atlantic Ocean using iron isotopes. *Nature Communications*, 10(1), 1-10. DOI: 10.1038/s41467-019-10457-w

Conway, T.M., John, S.G., 2014. Quantification of dissolved iron sources to the North Atlantic Ocean. *Nature*, 511(7508), 212-215.

Cranston, R.E., Murray, J.W., 1980. Chromium species in the Columbia River and estuary 1. *Limnology and Oceanography*, 25(6), 1104-1112.

Croal, L.R., Johnson, C.M., Beard, B.L., Newman, D.K., 2004. Iron isotope fractionation by Fe (II)-oxidizing photoautotrophic bacteria. *Geochimica et cosmochimica acta*, 68(6), 1227-1242.

Crosby, H.A., Johnson, C.M., Roden, E.E., Beard, B.L., 2005. Coupled Fe(II) - Fe(III) electron and atom exchange as a mechanism for Fe isotope fractionation during dissimilatory iron oxide reduction. Environmental Science & Technology, 39(17), 6698-6704.

Crowe, S.A., Døssing, L.N., Beukes, N.J., Bau, M., Kruger, S.J., Frei, R., Canfield, D.E., 2013. Atmospheric oxygenation three billion years ago. *Nature*, 501(7468), 535-538.

D'Arcy, J., Babechuk, M.G., Døssing, L.N., Gaucher, C., Frei, R., 2016. Processes controlling the chromium isotopic composition of river water: constraints from basaltic river catchments. *Geochimica et Cosmochimica Acta*, 186, 296-315.

Deng, B., Stone, A.T., 1996. Surface-catalyzed chromium (VI) reduction: reactivity comparisons of different organic reductants and different oxide surfaces. *Environmental Science & Technology*, 30(8), 2484-2494.

Dideriksen, K., Baker, J.A., Stipp, S.L.S., 2008. Equilibrium Fe isotope fractionation between inorganic aqueous Fe (III) and the siderophore complex, Fe (III)-desferrioxamine B. *Earth and Planetary Science Letters*, 269(1-2), 280-290.

Døssing, L.N., Dideriksen, K., Stipp, S.L.S., Frei, R., 2011. Reduction of hexavalent chromium by ferrous iron: a process of chromium isotope fractionation and its relevance to natural environments. *Chemical Geology*, 285(1-4), 157-166.

Douville, E., Charlou, J.L., Oelkers, E.H., Bienvenu, P., Colon, C.J., Donval, J.P., Fouquet, Y., Prieur, D., Appriou, P., 2002. The rainbow vent fluids (36 14' N, MAR): the influence of ultramafic rocks and phase separation on trace metal content in Mid-Atlantic Ridge hydrothermal fluids. *Chemical Geology*, 184(1-2), 37-48.

Duce, R.A., Liss, P.S., Merrill, J.T., Atlas, E.L., Buat-Menard, P., Hicks, B.B., Miller, J.M., Prospero, J.M., Arimoto, R.C.T.M., Church, T.M., Ellis, W., 1991. The atmospheric input of trace species to the world ocean. *Global biogeochemical cycles*, 5(3), 193-259.

Duce, R.A., Tindale, N.W., 1991. Atmospheric transport of iron and its deposition in the ocean. *Limnology and oceanography*, 36(8), 1715-1726.

Eary, L.E., Rai, D., 1987. Kinetics of chromium (III) oxidation to chromium (VI) by reaction with manganese dioxide. *Environmental Science & Technology*, 21(12), 1187-1193.

Eary, L.E., Rai, D., 1988. Chromate removal from aqueous wastes by reduction with ferrous ion. *Environmental Science & Technology*, 22(8), 972-977.

Edmond, J.M., Campbell, A.C., Palmer, M.R., Klinkhammer, G.P., German, C.R., Edmonds, H.N., Elderfield, H., Thompson, G. and Rona, P., 1995. Time series studies of vent fluids from the TAG and MARK sites (1986, 1990) Mid-Atlantic Ridge: a new solution chemistry model and a mechanism for Cu/Zn zonation in massive sulphide orebodies. *Geological Society, London, Special Publications*, 87(1), 77-86.

Edmonds, H.N. and German, C.R., 2004. Particle geochemistry in the Rainbow hydrothermal plume, Mid-Atlantic Ridge. *Geochimica et Cosmochimica Acta*, 68(4), 759-772.

Elderfield, H., 1970. Chromium speciation in sea water. *Earth and Planetary Science Letters*, 9(1), 10-16.

Elderfield, H., Schultz, A., 1996. Mid-ocean ridge hydrothermal fluxes and the chemical composition of the ocean. *Annual Review of Earth and Planetary Sciences*, 24(1), 191-224.

Ellis, A., Johnson, T., Villalobos-Aragon, A. and Bullen, T., 2008. Environmental cycling of Cr using stable isotopes: kinetic and equilibrium effects. AGUFM, 2008, H53F-08.

Ellis, A.S., Johnson, T.M., Bullen, T.D., 2002. Chromium isotopes and the fate of hexavalent chromium in the environment. *Science*, 295, 2060-2062.

Ellis, A.S., Johnson, T.M., Bullen, T.D., 2004. Using chromium stable isotope ratios to quantify Cr (VI) reduction: lack of sorption effects. *Environmental Science & Technology*, 38(13), 3604-3607.

Ellwood, M.J., Hutchins, D.A., Lohan, M.C., Milne, A., Nasemann, P., Nodder, S.D., Sander, S.G., Strzepek, R., Wilhelm, S.W., Boyd, P.W., 2015. Iron stable isotopes track pelagic iron cycling during a subtropical phytoplankton bloom. P*roceedings of the National Academy of Sciences*, 112(1), E15-E20.

Ellwood, M.J., Strzepek, R.F., Strutton, P.G., Trull, T.W., Fourquez, M., Boyd, P.W., 2020. Distinct iron cycling in a Southern Ocean eddy. *Nature communications*, 11(1). DOI: 10.1038/s41467-020-14464-0 OPE

Elrod, V.A., Berelson, W.M., Coale, K.H., Johnson, K.S., 2004. The flux of iron from continental shelf sediments: A missing source for global budgets. *Geophysical Research Letters*, 31(12). DOI: 10.1029/2004GL020216

Escoube, R., Rouxel, O.J., Sholkovitz, E., Donard, O.F., 2009. Iron isotope systematics in estuaries: The case of North River, Massachusetts (USA). *Geochimica et Cosmochimica Acta*, 73(14), 4045-4059.

Farkaš, J., Chrastný, V., Novák, M., Čadkova, E., Pašava, J., Chakrabarti, R., Jacobsen, S.B., Ackerman, L., Bullen, T.D., 2013. Chromium isotope variations (δ53/52Cr) in mantle-derived sources and their weathering products: Implications for environmental studies and the evolution of δ53/52Cr in the Earth's mantle over geologic time. *Geochimica et Cosmochimica Acta*, 123, 74-92.

Farkaš, J., Frýda, J., Paulukat, C., Hathorne, E.C., Matoušková, Š., Rohovec, J., Frýdová, B., Francova, M., Frei, R., 2018. Chromium isotope fractionation between modern seawater and biogenic carbonates from the Great Barrier Reef, Australia: Implications for the paleo-seawater δ^{53}Cr reconstruction. *Earth and Planetary Science Letters*, 498, 140-151.

Feely, R.A., Baker, E.T., Marumo, K., Urabe, T., Ishibashi, J., Gendron, J., Lebon, G.T., Okamura, K., 1996. Hydrothermal plume particles and dissolved phosphate over the superfast-spreading southern East Pacific Rise. *Geochimica et Cosmochimica Acta*, 60(13), 2297-2323.

Feely, R.A., Massoth, G.J., Trefry, J.H., Baker, E.T., Paulson, A.J., Lebon, G.T., 1994. Composition and sedimentation of hydrothermal plume particles from North Cleft segment, Juan de Fuca Ridge. *Journal of Geophysical Research: Solid Earth*, 99(B3), 4985-5006.

Fendorf, S., Wielinga, B.W., Hansel, C.M., 2000. Chromium transformations in natural environments: the role of biological and abiological processes in chromium (VI) reduction. *International Geology Review*, 42(8), 691-701.

Fendorf, S.E. and Li, G., 1996. Kinetics of chromate reduction by ferrous iron. *Environmental Science & Technology*, 30(5), 1614-1617.

Field, C.B., Behrenfeld, M.J., Randerson, J.T., Falkowski, P., 1998. Primary production of the biosphere: integrating terrestrial and oceanic components. *Science*, 281(5374), 237-240.

Field, M.P., Sherrell, R.M., 2000. Dissolved and particulate Fe in a hydrothermal plume at 9°45'N, East Pacific Rise: Slow Fe (II) oxidation kinetics in Pacific plumes. *Geochimica et Cosmochimica Acta*, 64(4), 619-628.

Findlay, A.J., Estes, E.R., Gartman, A., Yücel, M., Kamyshny, A., Luther, G.W., 2019. Iron and sulfide nanoparticle formation and transport in nascent hydrothermal vent plumes. *Nature communications*, 10(1), pp.1-7.

Findlay, A.J., Gartman, A., Shaw, T.J., Luther, G.W., 2015. Trace metal concentration and partitioning in the first 1.5 m of hydrothermal vent plumes along the Mid-Atlantic Ridge: TAG, Snakepit, and Rainbow. *Chemical Geology*, 412, 117-131.

Fitzsimmons, J.N., Carrasco, G.G., Wu, J., Roshan, S., Hatta, M., Measures, C.I., Conway, T.M., John, S.G., Boyle, E.A., 2015. Partitioning of dissolved iron and iron isotopes into soluble and colloidal phases along the GA03 GEOTRACES North Atlantic Transect. *Deep Sea Research Part II: Topical Studies in Oceanography*, 116, 130-151.

Fitzsimmons, J.N., John, S.G., Marsay, C.M., Hoffman, C.L., Nicholas, S.L., Toner, B.M., German, C.R., Sherrell, R.M., 2017. Iron persistence in a distal hydrothermal plume supported by dissolved-particulate exchange. *Nature Geoscience*, 10(3), 195-201.

Frank, A.B., Klaebe, R.M., Frei, R., 2019. Fractionation Behavior of Chromium Isotopes during the Sorption of Cr (VI) on Kaolin and its Implications for Using Black Shales as a Paleoredox Archive. *Geochemistry, Geophysics, Geosystems*, 20(5), 2290-2302.

Frei, R., Gaucher, C., Poulton, S.W., Canfield, D.E., 2009. Fluctuations in Precambrian atmospheric oxygenation recorded by chromium isotopes. *Nature*, 461, 250-253.

Frei, R., Poiré, D., Frei, K.M., 2014. Weathering on land and transport of chromium to the ocean in a subtropical region (Misiones, NW Argentina): a chromium stable isotope perspective. *Chemical Geology*, 381, 110-124.

German, C.R., Bowen, A., Coleman, M.L., Honig, D.L., Huber, J.A., Jakuba, M.V., Kinsey, J.C., Kurz, M.D., Leroy, S., McDermott, J.M., de Lépinay, B.M., 2010. Diverse styles of submarine venting on the ultraslow spreading Mid-Cayman Rise. *Proceedings of the National Academy of Sciences*, 107(32), 14020-14025.

German, C.R., Campbell, A.C., Edmond, J.M., 1991. Hydrothermal scavenging at the Mid-Atlantic Ridge: modification of trace element dissolved fluxes. *Earth and Planetary Science Letters*, 107(1), 101-114.

German, C.R., Casciotti, K.A., Dutay, J.C., Heimbürger, L.E., Jenkins, W.J., Measures, C.I., Mills, R.A., Obata, H., Schlitzer, R., Tagliabue, A., Turner, D.R., 2016. Hydrothermal impacts on trace element and isotope ocean biogeochemistry. *Philosophical Transactions of the Royal Society A: Mathematical, Physical and Engineering Sciences*, 374(2081). DOI: 10.1098/rsta.2016.0035

German, C.R., Seyfried, W.E., 2014. Hydrothermal processes. In *Treatise on Geochemistry* (eds Holland H. & Turekian K.), 191-233.

Glazer, B.T., Rouxel, O.J., 2009. Redox speciation and distribution within diverse iron-dominated microbial habitats at Loihi Seamount. *Geomicrobiology Journal*, 26(8), 606-622.

Gledhill, M., Buck, K.N., 2012. The organic complexation of iron in the marine environment: a review. *Frontiers in microbiology*, 3, 69.

Goring-Harford, H.J., Klar, J.K., Donald, H.K., Pearce, C.R., Connelly, D.P. and James, R.H., 2020. Behaviour of chromium and chromium isotopes during estuarine mixing in the Beaulieu Estuary, UK. *Earth and Planetary Science Letters*, 536. DOI: 10.1016/j.epsl.2020.116166

Goring-Harford, H.J., Klar, J.K., Pearce, C.R., Connelly, D.P., Achterberg, E.P., James, R.H., 2018. Behaviour of chromium isotopes in the eastern sub-tropical Atlantic Oxygen Minimum Zone. *Geochimica et Cosmochimica Acta*, 236, 41-59.

Gueguen, B., Reinhard, C.T., Algeo, T.J., Peterson, L.C., Nielsen, S.G., Wang, X., Rowe, H., Planavsky, N.J., 2016. The chromium isotope composition of reducing and oxic marine sediments. *Geochimica et Cosmochimica Acta*, 184, 1-19.

Guelke, M. and Von Blanckenburg, F., 2007. Fractionation of stable iron isotopes in higher plants. *Environmental Science & Technology*, 41(6), 1896-1901.

Hatta, M., Measures, C.I., Wu, J., Roshan, S., Fitzsimmons, J.N., Sedwick, P., Morton, P., 2015. An overview of dissolved Fe and Mn distributions during the 2010–2011 US GEOTRACES north Atlantic cruises: GEOTRACES GA03. *Deep Sea Research Part II: Topical Studies in Oceanography*, 116, 117-129.

Hawkes, J.A., Connelly, D., Gledhill, M., Achterberg, E.P., 2013. The stabilisation and transportation of dissolved iron from high temperature hydrothermal vent systems. *Earth and Planetary Science Letters*, 375, 280-290.

Hodgkinson, M.R., Webber, A.P., Roberts, S., Mills, R.A., Connelly, D.P., Murton, B.J., 2015. Talc-dominated seafloor deposits reveal a new class of hydrothermal system. *Nature Communications*, 6. DOI: 10.1038/ncomms10150

Hoffman, C.L., Nicholas, S.L., Ohnemus, D.C., Fitzsimmons, J.N., Sherrell, R.M., German, C.R., Heller, M.I., Lee, J.M., Lam, P.J., Toner, B.M., 2018. Near-field iron and carbon chemistry of non-buoyant hydrothermal plume particles, Southern East Pacific Rise 15°S. *Marine Chemistry*, 201, 183-197.

Holmes, T.M., Chase, Z., van der Merwe, P., Townsend, A.T., Bowie, A.R., 2017. Detection, dispersal and biogeochemical contribution of hydrothermal iron in the ocean. *Marine and Freshwater Research*, 68(12), 2184-2204.

Homoky, W.B., John, S.G., Conway, T.M., Mills, R.A., 2013. Distinct iron isotopic signatures and supply from marine sediment dissolution. *Nature Communications*, 4. DOI: 10.1038/ncomms3143

Homoky, W.B., Severmann, S., Mills, R.A., Statham, P.J., Fones, G.R., 2009. Pore-fluid Fe isotopes reflect the extent of benthic Fe redox recycling: evidence from continental shelf and deep-sea sediments. *Geology*, 37(8), 751-754.

Hopwood, M.J., Carroll, D., Höfer, J., Achterberg, E.P., Meire, L., Le Moigne, F.A., Bach, L.T., Eich, C., Sutherland, D.A., González, H.E., 2019. Highly variable iron content modulates iceberg-ocean fertilisation and potential carbon export. *Nature Communications*, 10(1). DOI: 10.1038/s41467-019-13231-0 |

Huang, J., Hao, J., Huang, F., Sverjensky, D.A., 2019. Mobility of chromium in high temperature crustal and upper mantle fluids. *Geochemical Perspective Letters*, 12, 1-6. DOI: 10.7185/geochemlet.1926

Icopini, G.A., Anbar, A.D., Ruebush, S.S., Tien, M., Brantley, S.L., 2004. Iron isotope fractionation during microbial reduction of iron: the importance of adsorption. *Geology*, 32(3), 205-208.

Izbicki, J.A., Ball, J.W., Bullen, T.D., Sutley, S.J., 2008. Chromium, chromium isotopes and selected trace elements, western Mojave Desert, USA. *Applied Geochemistry*, 23(5), 1325-1352.

James, R.H., Green, D.R., Stock, M.J., Alker, B.J., Banerjee, N.R., Cole, C., German, C.R., Huvenne, V.A., Powell, A.M. and Connelly, D.P., 2014. Composition of hydrothermal fluids and mineralogy of associated chimney material on the East Scotia Ridge back-arc spreading centre. *Geochimica et Cosmochimica Acta*, 139, 47-71.

Jamieson-Hanes, J.H., Lentz, A.M., Amos, R.T., Ptacek, C.J., Blowes, D.W., 2014. Examination of Cr (VI) treatment by zero-valent iron using in situ, real-time X-ray absorption spectroscopy and Cr isotope measurements. *Geochimica et Cosmochimica Acta*, 142, 299-313.

Janssen, D.J., Rickli, J., Quay, P.D., White, A.E., Nasemann, P., Jaccard, S.L., 2019. Biological control of chromium redox and stable isotope composition in the surface ocean. *Global Biogeochemical Cycles*. DOI: 10.1029/2019GB006397

Jeandel, C., Minster, J.F., 1987. Chromium behavior in the ocean: Global versus regional processes. *Global Biogeochemical Cycles*, 1(2), 131-154.

Jenkins, W.J., Smethie Jr, W.M., Boyle, E.A., Cutter, G.A., 2015. Water mass analysis for the US GEOTRACES (GA03) North Atlantic sections. *Deep Sea Research Part II: Topical Studies in Oceanography*, 116, 6-20.

Jickells, T.D., An, Z.S., Andersen, K.K., Baker, A.R., Bergametti, G., Brooks, N., Cao, J.J., Boyd, P.W., Duce, R.A., Hunter, K.A., Kawahata, H., 2005. Global iron connections between desert dust, ocean biogeochemistry, and climate. *Science*, 308(5718), 67-71.

John, S. G., Helgoe, J., Townsend, E., Weber, T., DeVries, T., Tagliabue, A., Moore, K., Lam, P., Marsay, C. M., Till, C., 2018. Biogeochemical cycling of Fe and Fe stable isotopes in the Eastern Tropical South Pacific. *Marine Chemistry*, 201, 66-76.

John, S.G., Adkins, J., 2012. The vertical distribution of iron stable isotopes in the North Atlantic near Bermuda. *Global Biogeochemical Cycles*, 26(2). DOI: 10.1029/2011GB004043

John, S.G., Adkins, J.F., 2010. Analysis of dissolved iron isotopes in seawater. *Marine Chemistry*, 119(1), 65-76.

John, S.G., Helgoe, J., Townsend, E., Weber, T., DeVries, T., Tagliabue, A., Moore, K., Lam, P., Marsay, C.M., Till, C., 2018. Biogeochemical cycling of Fe and Fe stable isotopes in the Eastern Tropical South Pacific. *Marine Chemistry*, 201, 66-76.

John, S.G., Mendez, J., Moffett, J., Adkins, J., 2012. The flux of iron and iron isotopes from San Pedro Basin sediments. *Geochimica et Cosmochimica Acta*, 93, 14-29.

Johns, W.E., Townsend, T.L., Fratantoni, D.M., Wilson, W.D., 2002. On the Atlantic inflow to the Caribbean Sea. *Deep Sea Research Part I: Oceanographic Research Papers*, 49(2), 211-243.

Johnson, C.M., Beard, B.L., Albarède, F. eds., 2018. Geochemistry of non-traditional stable isotopes (Vol. 55). Walter de Gruyter GmbH & Co KG.

Johnson, C.M., Roden, E.E., Welch, S.A., Beard, B.L., 2005. Experimental constraints on Fe isotope fractionation during magnetite and Fe carbonate formation coupled to dissimilatory hydrous ferric oxide reduction. *Geochimica et Cosmochimica Acta*, 69(4), 963-993.

Kadko, D., 1993. An assessment of the effect of chemical scavenging within submarine hydrothermal plumes upon ocean geochemistry. *Earth and Planetary Science Letters*, 120(3-4), 361-374.

Kagaya, S., Maeba, E., Inoue, Y., Kamichatani, W., Kajiwara, T., Yanai, H., Saito, M., Tohda, K., 2009. A solid phase extraction using a chelate resin immobilizing carboxymethylated pentaethylenehexamine for separation and preconcentration of trace elements in water samples. *Talanta*, 79(2), 146-152.

Kitchen, J.W., Johnson, T.M., Bullen, T.D., Zhu, J., Raddatz, A., 2012. Chromium isotope fractionation factors for reduction of Cr (VI) by aqueous Fe (II) and organic molecules. *Geochimica et Cosmochimica Acta*, 89, 190-201.

Klar, J.K., James, R.H., Gibbs, D., Lough, A., Parkinson, I., Milton, J.A., Hawkes, J.A., Connelly, D.P., 2017. Isotopic signature of dissolved iron delivered to the Southern Ocean from hydrothermal vents in the East Scotia Sea. *Geology*, 45(4), 351-354.

Klar, J.K., Schlosser, C., Milton, J.A., Woodward, E.M.S., Lacan, F., Parkinson, I.J., Achterberg, E.P., James, R.H., 2018. Sources of dissolved iron to oxygen minimum zone waters on the Senegalese continental margin in the tropical North Atlantic Ocean: Insights from iron isotopes. *Geochimica et Cosmochimica Acta*, 236, 60-78.

Kleint, C., Hawkes, J.A., Sander, S.G., Koschinsky, A., 2016. Voltammetric investigation of hydrothermal iron speciation. *Frontiers in Marine Science*, 3, 75.

Klunder, M.B., Laan, P., Middag, R., De Baar, H.J.W., Bakker, K., 2012. Dissolved iron in the Arctic Ocean: Important role of hydrothermal sources, shelf input and scavenging removal. *Journal of Geophysical Research: Oceans*, 117(C4). DOI: 10.1029/2011JC007135.

Klunder, M.B., Laan, P., Middag, R., De Baar, H.J.W., Van Ooijen, J.C., 2011. Dissolved iron in the Southern Ocean (Atlantic sector). *Deep Sea Research Part II: Topical Studies in Oceanography*, 58(25-26), 2678-2694.

Kunde, K., Wyatt, N.J., González-Santana, D., Tagliabue, A., Mahaffey, C., Lohan, M.C., 2019. Iron Distribution in the Subtropical North Atlantic: The Pivotal Role of Colloidal Iron. *Global Biogeochemical Cycles*. DOI: 10.1029/2019GB006326

Lacan, F., Radic, A., Labatut, M., Jeandel, C., Poitrasson, F., Sarthou, G., Pradoux, C., Chmeleff, J., Freydier, R., 2010. High-precision determination of the isotopic composition of dissolved iron in iron depleted seawater by double spike multicollector-ICPMS. *Analytical chemistry*, 82(17), 7103-7111.

Lam, P.J., Bishop, J.K., 2008. The continental margin is a key source of iron to the HNLC North Pacific Ocean. *Geophysical Research Letters*, 35(7). DOI: 10.1029/2008GL033294

Ledwell, J.R., Montgomery, E.T., Polzin, K.L., Laurent, L.S., Schmitt, R.W., Toole, J.M., 2000. Evidence for enhanced mixing over rough topography in the abyssal ocean. *Nature*, 403(6766), 179-182.

Li, S.X., Zheng, F.Y., Hong, H.S., Deng, N.S., Lin, L.X., 2009. Influence of marine phytoplankton, transition metals and sunlight on the species distribution of chromium in surface seawater. *Marine environmental research*, 67(4-5), 199-206.

Lough, A., 2016. Trace metal chemistry of hydrothermal plumes. Doctoral dissertation, University of Southampton.

Lough, A., Klar, J., Homoky, W., Comer-Warner, S., Milton, J., Connelly, D., James, R., Mills, R., 2017. Opposing authigenic controls on the isotopic signature of dissolved iron in hydrothermal plumes. *Geochimica et Cosmochimica Acta*, 202, 1-20.

Lough, A.J.M., Connelly, D.P., Homoky, W.B., Hawkes, J.A., Chavagnac, V., Castillo, A., Kazemian, M., Nakamura, K.I., Araki, T., Kaulich, B., Mills, R.A, 2019b. Diffuse hydrothermal venting: A hidden source of iron to the oceans. *Frontiers in Marine Science*, 6. DOI: 10.3389/fmars.2019.00329

Lough, A.J.M., et al., *in prep*. Iron supply from the Mid Atlantic Ridge to the North Atlantic Ocean.

Lough, A.J.M., Homoky, W.B., Connelly, D.P., Comer-Warner, S.A., Nakamura, K., Abyaneh, M.K., Kaulich, B., Mills, R.A., 2019a. Soluble iron conservation and colloidal iron dynamics in a hydrothermal plume. *Chemical Geology*, 511 (225-237).

Loyaux-Lawniczak, S., Lecomte, P., Ehrhardt, J.J., 2001. Behavior of hexavalent chromium in a polluted groundwater: redox processes and immobilization in soils. Environmental Science & Technology, 35(7), 1350-1357.

Martin, J.H., 1990. Glacial-interglacial CO_2 change: The iron hypothesis. *Paleoceanography*, 5(1), 1-13.

Martin, J.H., Fitzwater, S.E., 1988. Iron deficiency limits phytoplankton growth in the north-east Pacific subarctic. *Nature*, 331(6154), 341-343.

McClain, C.N., Maher, K., 2016. Chromium fluxes and speciation in ultramafic catchments and global rivers. *Chemical Geology*, 426, 135-157.

McDermott, J.M., 2015. Geochemistry of deep-sea hydrothermal vent fluids from the Mid-Cayman Rise, Caribbean Sea. Doctoral dissertation, Massachusetts Institute of Technology.

McDermott, J.M., Seewald, J.S., German, C.R., Sylva, S.P., 2015. Pathways for abiotic organic synthesis at submarine hydrothermal fields. *Proceedings of the National Academy of Sciences*, 112(25), 7668-7672.

McDermott, J.M., Sylva, S.P., Ono, S., German, C.R., Seewald, J.S., 2018. Geochemistry of fluids from Earth's deepest ridge-crest hot-springs: Piccard hydrothermal field, Mid-Cayman Rise. *Geochimica et Cosmochimica Acta*, 228, 95-118.

Mellett, T., et al., *in prep*. Using shipboard incubations to assess the cycling of iron (Fe) and Fe-binding ligands in hydrothermal vent plumes along the Mid-Atlantic Ridge.

Middleton, S.S., Latmani, R.B., Mackey, M.R., Ellisman, M.H., Tebo, B.M., Criddle, C.S., 2003. Cometabolism of Cr (VI) by Shewanella oneidensis MR-1 produces cell-associated reduced chromium and inhibits growth. *Biotechnology and Bioengineering*, 83(6), 627-637.

Millero, F.J., Sotolongo, S., Izaguirre, M., 1987. The oxidation kinetics of Fe (II) in seawater. *Geochimica et Cosmochimica Acta*, 51(4), 793-801.

Moore, C.M., Mills, M.M., Arrigo, K.R., Berman-Frank, I., Bopp, L., Boyd, P.W., Galbraith, E.D., Geider, R.J., Guieu, C., Jaccard, S.L., Jickells, T.D., 2013. Processes and patterns of oceanic nutrient limitation. *Nature Geoscience*, 6(9), 701-710.

Moore, J.K., Doney, S.C., Glover, D.M., Fung, I.Y., 2001. Iron cycling and nutrient-limitation patterns in surface waters of the World Ocean. *Deep Sea Research Part II: Topical Studies in Oceanography*, 49(1-3), 463-507.

Moore, W.S., 1984. Review of the GEOSECS project. *Nuclear Instruments and Methods in Physics Research*, 223 (2-3): 459-465.

Moos, S.B., 2018. The marine biogeochemistry of chromium isotopes. Doctoral dissertation, Massachusetts Institute of Technology.

Moos, S.B., Boyle, E.A., 2019. Determination of accurate and precise chromium isotope ratios in seawater samples by MC-ICP-MS illustrated by analysis of SAFe Station in the North Pacific Ocean. *Chemical Geology*, 511, 481-493.

Moos, S.B., Boyle, E.A., Altabet, M.A., Bourbonnais, A., 2020. Investigating the cycling of chromium in the oxygen deficient waters of the Eastern Tropical North Pacific Ocean and the Santa Barbara Basin using stable isotopes. *Marine Chemistry*, 221. DOI: 10.1016/j.marchem.2020.103756

Morgan, J.J., 2005. Kinetics of reaction between O_2 and Mn (II) species in aqueous solutions. *Geochimica et Cosmochimica Acta*, 69(1), 35-48.

Morgan, J.L., Wasylenki, L.E., Nuester, J., Anbar, A.D., 2010. Fe isotope fractionation during equilibration of Fe-organic complexes. *Environmental Science & Technology*, 44(16), 6095-6101.

Mottl, M.J., McConachy, T.F., 1990. Chemical processes in buoyant hydrothermal plumes on the East Pacific Rise near 21°N. *Geochimica et Cosmochimica Acta*, 54(7), 1911-1927.

Murray, J.W., Spell, B., Paul, B., 1983. The contrasting geochemistry of manganese and chromium in the eastern tropical Pacific Ocean. In *Trace metals in sea water*, 643-669. Springer, Boston, MA.

Nasemann, P., Gault-Ringold, M., Stirling, C.H., Koschinsky, A., Sander, S.G., 2018. Processes affecting the isotopic composition of dissolved iron in hydrothermal plumes: A case study from the Vanuatu back-arc. *Chemical Geology*, 476, 70-84.

Nasemann, P., Janssen, D.J., Rickli, J., Grasse, P., Frank, M., Jaccard, S.L., 2020. Chromium reduction and associated stable isotope fractionation restricted to anoxic shelf waters in the Peruvian Oxygen Minimum Zone. *Geochimica et Cosmochimica Acta*. DOI: 10.1016/j.gca.2020.06.027

Obata, H., Karatani, H., Nakayama, E., 1993. Automated determination of iron in seawater by chelating resin concentration and chemiluminescence detection. *Analytical Chemistry*, 65(11), 1524-1528.

Ohnemus, D.C., Lam, P.J., 2015. Cycling of lithogenic marine particles in the US GEOTRACES North Atlantic transect. *Deep Sea Research Part II: Topical Studies in Oceanography*, 116, 283-302.

Ohnemus, D.C., Torrie, R., Twining, B.S., 2019. Exposing the distributions and elemental associations of scavenged particulate phases in the ocean using basin-scale multi-element data sets. *Global Biogeochemical Cycles*, 33(6), 725-748.

Oze, C., Bird, D.K., Fendorf, S., 2007. Genesis of hexavalent chromium from natural sources in soil and groundwater. *Proceedings of the National Academy of Sciences*, 104(16), 6544-6549.

Oze, C., Sleep, N.H., Coleman, R.G., Fendorf, S., 2016. Anoxic oxidation of chromium. *Geology*, 44(7), 543-546.

Patterson, C., 1974. Lead in seawater. *Science*, 183(4124), 553-554.

Paulukat, C., Døssing, L.N., Mondal, S.K., Voegelin, A.R. and Frei, R., 2015. Oxidative release of chromium from Archean ultramafic rocks, its transport and environmental impact - A Cr isotope perspective on the Sukinda valley ore district (Orissa, India). *Applied Geochemistry*, 59, 125-138.

Paulukat, C., Gilleaudeau, G.J., Chernyavskiy, P., Frei, R., 2016. The Cr isotope signature of surface seawater - a global perspective. *Chemical Geology*, 444, 101-109.

Person, R., Aumont, O., Madec, G., Vancoppenolle, M., Bopp, L., Merino, N., 2019. Sensitivity of ocean biogeochemistry to the iron supply from the Antarctic Ice Sheet explored with a biogeochemical model. *Biogeosciences*, 16, 3583-3603. DOI: 10.5194/bg-16-3583-2019

Pettine, M., D'ottone, L., Campanella, L., Millero, F.J., Passino, R., 1998. The reduction of chromium (VI) by iron (II) in aqueous solutions. *Geochimica et Cosmochimica Acta*, 62(9), 1509-1519.

Pettine, M., Millero, F.J., 1990. Chromium speciation in seawater: The probable role of hydrogen peroxide. *Limnology and Oceanography*, 35(3), 730-736.

Pettine, M., Millero, F.J., Passino, R., 1994. Reduction of chromium (VI) with hydrogen sulfide in NaCl media. *Marine Chemistry*, 46(4), 335-344.

Planavsky, N.J., Asael, D., Hofmann, A., Reinhard, C.T., Lalonde, S.V., Knudsen, A., Wang, X., Ossa, F.O., Pecoits, E., Smith, A.J., Beukes, N.J., 2014b. Evidence for oxygenic photosynthesis half a billion years before the Great Oxidation Event. *Nature Geoscience*, 7(4), 283-286.

Planavsky, N.J., Reinhard, C.T., Wang, X., Thomson, D., McGoldrick, P., Rainbird, R.H., Johnson, T., Fischer, W.W., Lyons, T.W., 2014a. Low Mid-Proterozoic atmospheric oxygen levels and the delayed rise of animals. *Science*, 346(6209), 635-638.

Radic, A., Lacan, F., Murray, J.W., 2011. Iron isotopes in the seawater of the equatorial Pacific Ocean: New constraints for the oceanic iron cycle. *Earth and Planetary Science Letters*, 306(1-2), 1-10.

Rai, D., Sass, B.M., Moore, D.A., 1987. Chromium (III) hydrolysis constants and solubility of chromium (III) hydroxide. *Inorganic Chemistry*, 26(3), 345-349.

Reinhard, C.T., Planavsky, N.J., Robbins, L.J., Partin, C.A., Gill, B.C., Lalonde, S.V., Bekker, A., Konhauser, K.O., Lyons, T.W., 2013. Proterozoic ocean redox and biogeochemical stasis. *Proceedings of the National Academy of Sciences*, 110(14), 5357-5362.

Reinhard, C.T., Planavsky, N.J., Wang, X., Fischer, W.W., Johnson, T.M., Lyons, T.W., 2014. The isotopic composition of authigenic chromium in anoxic marine sediments: A case study from the Cariaco Basin. *Earth and Planetary Science Letters*, 407, 9-18.

Resing, J.A., Mottl, M.J., 1992. Determination of manganese in seawater using flow injection analysis with on-line preconcentration and spectrophotometric detection. *Analytical Chemistry*, 64(22), 2682-2687.

Resing, J.A., Sedwick, P.N., German, C.R., Jenkins, W.J., Moffett, J.W., Sohst, B.M., Tagliabue, A., 2015. Basin-scale transport of hydrothermal dissolved metals across the South Pacific Ocean. *Nature*, 523(7559), 200-203.

Richard, F.C., Bourg, A.C., 1991. Aqueous geochemistry of chromium: a review. *Water research*, 25(7), 807-816.

Rickli, J., Janssen, D.J., Hassler, C., Ellwood, M.J., Jaccard, S.L., 2019. Chromium biogeochemistry and stable isotope distribution in the Southern Ocean. *Geochimica et cosmochimica acta*, 262, 188-206.

Rolison, J.M., Stirling, C.H., Middag, R., Gault-Ringold, M., George, E., Rijkenberg, M.J., 2018. Iron isotope fractionation during pyrite formation in a sulfidic Precambrian ocean analogue. *Earth and Planetary Science Letters*, 488, 1-13.

Rosenberg, N.D., Lupton, J.E., Kadko, D., Collier, R., Lilley, M.D., Pak, H., 1988. Estimation of heat and chemical fluxes from a seafloor hydrothermal vent field using radon measurements. *Nature*, 334(6183), 604-607.

Rouxel, O., Dobbek, N., Ludden, J., Fouquet, Y., 2003. Iron isotope fractionation during oceanic crust alteration. *Chemical Geology*, 202(1-2), 155-182.

Rouxel, O., Fouquet, Y., Ludden, J.N., 2004. Subsurface processes at the lucky strike hydrothermal field, Mid-Atlantic ridge: evidence from sulfur, selenium, and iron isotopes. *Geochimica et Cosmochimica Acta*, 68(10), 2295-2311.

Rouxel, O., Shanks, W.C., Bach, W., Edwards, K.J., 2008. Integrated Fe- and S-isotope study of seafloor hydrothermal vents at East Pacific Rise 9-10°N. *Chemical Geology*, 252(3), 214-227.

Rouxel, O., Toner, B., Germain, Y., Glazer, B., 2018. Geochemical and iron isotopic insights into hydrothermal iron oxyhydroxide deposit formation at Loihi Seamount. *Geochimica et Cosmochimica Acta*, 220, 449-482.

Rouxel, O., Toner, B.M., Manganini, S.J., German, C.R., 2016. Geochemistry and iron isotope systematics of hydrothermal plume fall-out at East Pacific Rise 9°50' N. *Chemical Geology*, 441, 212-234.

Rubin, M., Berman-Frank, I., Shaked, Y., 2011. Dust- and mineral-iron utilization by the marine dinitrogen-fixer Trichodesmium. *Nature Geoscience*, 4(8), 529-534.

Rudnicki, M.D., Elderfield, H., 1993. A chemical model of the buoyant and neutrally buoyant plume above the TAG vent field, 26 degrees N, Mid-Atlantic Ridge. *Geochimica et Cosmochimica Acta*, 57(13), 2939-2957.

Rudnicki, M.D., James, R.H., Elderfield, H., 1994. Near-field variability of the TAG non-buoyant plume, 26°N, Mid-Atlantic Ridge. *Earth and Planetary Science Letters*, 127(1-4), 1-10.

Rue, E.L., Smith, G.J., Cutter, G.A., Bruland, K.W., 1997. The response of trace element redox couples to suboxic conditions in the water column. *Deep Sea Research Part I: Oceanographic Research Papers*, 44(1), 113-134.

Saad, E.M., Wang, X., Planavsky, N.J., Reinhard, C.T., Tang, Y., 2017. Redox-independent chromium isotope fractionation induced by ligand-promoted dissolution. *Nature communications*, 8(1), 1-10.

Saito, M.A., Noble, A.E., Tagliabue, A., Goepfert, T.J., Lamborg, C.H., Jenkins, W.J., 2013. Slow-spreading submarine ridges in the South Atlantic as a significant oceanic iron source. *Nature Geoscience*, 6(9), 775-779.

Sander, S. and Koschinsky, A., 2000. Onboard-ship redox speciation of chromium in diffuse hydrothermal fluids from the North Fiji Basin. *Marine Chemistry*, 71(1-2), 83-102.

Scheiderich, K., Amini, M., Holmden, C., Francois, R., 2015. Global variability of chromium isotopes in seawater demonstrated by Pacific, Atlantic, and Arctic Ocean samples. *Earth and Planetary Science Letters*, 423, 87-97.

Schlitzer, R., 2009. Ocean data view. http://odv. awi. de

Schoenberg, R., Zink, S., Staubwasser, M., von Blanckenburg, F., 2008. The stable Cr isotope inventory of solid Earth reservoirs determined by double spike MC-ICP-MS. *Chemical Geology*, 249(3-4), 294-306.

Scholz, F., McManus, J., Mix, A.C., Hensen, C., Schneider, R.R., 2014. The impact of ocean deoxygenation on iron release from continental margin sediments. *Nature Geoscience*, 7(6), 433-437.

Schroeder, D.C., Lee, G.F., 1975. Potential transformations of chromium in natural waters. *Water, Air, and Soil Pollution*, 4(3-4), 355-365.

Sedlak, D.L., Chan, P.G., 1997. Reduction of hexavalent chromium by ferrous iron. *Geochimica et Cosmochimica Acta*, 61(11), 2185-2192.

Semeniuk, D.M., Maldonado, M.T. and Jaccard, S.L., 2016. Chromium uptake and adsorption in marine phytoplankton - Implications for the marine chromium cycle. *Geochimica et Cosmochimica Acta*, 184, 41-54.

Severmann, S., Johnson, C., Beard, B., German, C., Edmonds, H., Chiba, H., Green, D., 2004. The effect of plume processes on the Fe isotope composition of hydrothermally derived Fe in the deep ocean as inferred from the Rainbow vent site, Mid-Atlantic Ridge, 36°14′ N. *Earth and Planetary Science Letters*, 225(1), 63-76.

Severmann, S., Johnson, C.M., Beard, B.L., McManus, J., 2006. The effect of early diagenesis on the Fe isotope compositions of porewaters and authigenic minerals in continental margin sediments. *Geochimica et Cosmochimica Acta*, 70(8), 2006-2022.

Sharma, M., Polizzotto, M., Anbar, A., 2001. Iron isotopes in hot springs along the Juan de Fuca Ridge. *Earth and Planetary Science Letters*, 194(1), 39-51.

Shelley, R.U., Morton, P.L., Landing, W.M., 2015. Elemental ratios and enrichment factors in aerosols from the US-GEOTRACES North Atlantic transects. *Deep Sea Research Part II: Topical Studies in Oceanography*, 116, 262-272.

Sikora, E.R., Johnson, T.M., Bullen, T.D., 2008. Microbial mass-dependent fractionation of chromium isotopes. Geochimica et Cosmochimica Acta, 72, 3631-3641.

Sirinawin, W., Turner, D.R., Westerlund, S., 2000. Chromium (VI) distributions in the Arctic and the Atlantic Oceans and a reassessment of the oceanic Cr cycle. *Marine chemistry*, 71(3-4), 265-282.

Skulan, J.L., Beard, B.L., Johnson, C.M., 2002. Kinetic and equilibrium Fe isotope fractionation between aqueous Fe (III) and hematite. *Geochimica et Cosmochimica Acta*, 66, 2995-3015.

St Laurent, L.C., Thurnherr, A.M., 2007. Intense mixing of lower thermocline water on the crest of the Mid-Atlantic Ridge. *Nature*, 448(7154), 680-683.

Statham, P., German, C., Connelly, D., 2005. Iron (II) distribution and oxidation kinetics in hydrothermal plumes at the Kairei and Edmond vent sites, Indian Ocean. *Earth and Planetary Science Letters*, 236(3), 588-596.

Stordal, M.C., Santschi, P.H., Gill, G.A., 1996. Colloidal pumping: evidence for the coagulation process using natural colloids tagged with ^{203}Hg. *Environmental Science & Technology*, 30(11), 3335-3340.

Strzepek, R.F., Maldonado, M.T., Hunter, K.A., Frew, R.D., Boyd, P.W., 2011. Adaptive strategies by Southern Ocean phytoplankton to lessen iron limitation: Uptake of organically complexed iron and reduced cellular iron requirements. *Limnology and oceanography*, 56(6), 1983-2002.

Tagliabue, A., Aumont, O., Bopp, L., 2014. The impact of different external sources of iron on the global carbon cycle. *Geophysical Research Letters*, 41(3), 920-926.

Tagliabue, A., Bopp, L., Dutay, J.-C., Bowie, A.R., Chever, F., Jean-Baptiste, P., Bucciarelli, E., Lannuzel, D., Remenyi, T., Sarthou, G., 2010. Hydrothermal contribution to the oceanic dissolved iron inventory. *Nature Geoscience*, 3(4), 252-256.

Tagliabue, A., Bowie, A.R., Boyd, P.W., Buck, K.N., Johnson, K.S., Saito, M.A., 2017. The integral role of iron in ocean biogeochemistry. *Nature*, 543(7643), 51-59.

Tagliabue, A., Bowie, A.R., DeVries, T., Ellwood, M.J., Landing, W.M., Milne, A., Ohnemus, D.C., Twining, B.S., Boyd, P.W., 2019. The interplay between regeneration and scavenging fluxes drives ocean iron cycling. *Nature Communications*, 10(1), 1-8.

Tagliabue, A., Resing, J., 2016. Impact of hydrothermalism on the ocean iron cycle. *Phil. Trans. R. Soc. A* 374 (2081). DOI: 10.1098/rsta.2015.0291

Teng, F.Z., Dauphas, N., Huang, S., Marty, B., 2013. Iron isotopic systematics of oceanic basalts. *Geochimica et Cosmochimica Acta*, 107, 12-26.

Thompson, G., Humphris, S. E., Schroeder, B., Sulanowska, M., Rona, P. A., 1988. Active vents and massive sulfides at 26 degrees N (TAG) and 23 degrees N (Snakepit) on the Mid-Atlantic Ridge. *The Canadian Mineralogist*, 26(3), 697-711.

Toner, B.M., Fakra, S.C., Manganini, S.J., Santelli, C.M., Marcus, M.A., Moffett, J.W., Rouxel, O., German, C.R., Edwards, K.J., 2009. Preservation of iron (II) by carbon-rich matrices in a hydrothermal plume. *Nature Geoscience*, 2(3), 197-201.

Tribovillard, N., Algeo, T.J., Lyons, T., Riboulleau, A., 2006. Trace metals as paleoredox and paleoproductivity proxies: an update. *Chemical Geology*, 232(1-2), 12-32.

Trocine, R.P., Trefry, J.H., 1988. Distribution and chemistry of suspended particles from an active hydrothermal vent site on the Mid-Atlantic Ridge at 26°N. *Earth and Planetary Science Letters*, 88(1-2), 1-15.

Tuerena, R.E., Williams, R.G., Mahaffey, C., Vic, C., Green, J.M., Naveira-Garabato, A., Forryan, A., Sharples, J., 2019. Internal tides drive nutrient fluxes into the deep chlorophyll maximum over mid-ocean ridges. *Global Biogeochemical Cycles*, 33(8), 995-1009.

Turick, C.E., Apel, W.A., Carmiol, N.S., 1996. Isolation of hexavalent chromium-reducing anaerobes from hexavalent-chromium-contaminated and noncontaminated environments. *Applied Microbiology and Biotechnology*, 44(5), 683-688.

Ussher, S.J., Achterberg, E.P., Worsfold, P.J., 2004. Marine biogeochemistry of iron. *Environmental Chemistry*, 1(2), 67-80.

Vic, C., Naveira Garabato, A.C., Green, J.M., Spingys, C., Forryan, A., Zhao, Z., Sharples, J., 2018. The lifecycle of semidiurnal internal tides over the northern Mid-Atlantic Ridge. *Journal of Physical Oceanography*, 48(1), 61-80.

Von Damm, K.L., 2000. Chemistry of hydrothermal vent fluids from 9-10 N, East Pacific Rise: "Time zero," the immediate posteruptive period. *Journal of Geophysical Research: Solid Earth*, 105(B5), 11203-11222.

Von Damm, K.L., Lilley, M.D., Shanks Iii, W.C., Brockington, M., Bray, A.M., O'grady, K.M., Olson, E., Graham, A. Proskurowski, G., 2003. Extraordinary phase separation and segregation in vent fluids from the southern East Pacific Rise. *Earth and Planetary Science Letters*, 206(3-4), 365-378.

Waeles, M., Baker, A.R., Jickells, T., Hoogewerff, J., 2007. Global dust teleconnections: aerosol iron solubility and stable isotope composition. *Environmental Chemistry*, 4, 233-237.

Wang, X., Glass, J.B., Reinhard, C.T. Planavsky, N.J., 2019. Species-dependent chromium isotope fractionation across the eastern tropical North Pacific oxygen minimum zone. *Geochemistry, Geophysics, Geosystems*, 20(5), 2499-2514.

Wang, X., Johnson, T.M., Ellis, A.S., 2015. Equilibrium isotopic fractionation and isotopic exchange kinetics between Cr (III) and Cr (VI). Geochimica et Cosmochimica Acta, 153, 72-90.

Watson, A., Bakker, D., Ridgwell, A., Boyd, P., Law, C., 2000. Effect of iron supply on Southern Ocean CO_2 uptake and implications for glacial atmospheric CO_2. *Nature*, 407(6805), 730-733.

Webber, A.P., Roberts, S., Murton, B.J., Hodgkinson, M.R., 2015. Geology, sulfide geochemistry and supercritical venting at the Beebe Hydrothermal Vent Field, Cayman Trough. *Geochemistry, Geophysics, Geosystems*, 16(8), 2661-2678.

Wei, W., Klaebe, R., Ling, H.F., Huang, F., Frei, R., 2020. Biogeochemical cycle of chromium isotopes at the modern Earth's surface and its applications as a paleo-environment proxy. *Chemical Geology*. DOI: 10.1016/j.chemgeo.2020.119570

Welch, S., Beard, B., Johnson, C., Braterman, P., 2003. Kinetic and equilibrium Fe isotope fractionation between aqueous Fe (II) and Fe (III). *Geochimica et Cosmochimica Acta*, 67(22), 4231-4250.

Wu, J., Boyle, E., Sunda, W., Wen, L.S., 2001. Soluble and colloidal iron in the oligotrophic North Atlantic and North Pacific. *Science*, 293(5531), 847-849.

Wu, L., Beard, B.L., Roden, E.E., Johnson, C.M., 2011. Stable iron isotope fractionation between aqueous Fe (II) and hydrous ferric oxide. *Environmental Science & Technology*, 45(5), 1847-1852.

Wu, W., Wang, X., Reinhard, C.T., Planavsky, N.J., 2017. Chromium isotope systematics in the Connecticut River. *Chemical Geology*, 456, 98-111.

Ye, Y., Völker, C., 2017. On the role of dust-deposited lithogenic particles for iron cycling in the tropical and subtropical Atlantic. *Global Biogeochemical Cycles*, 31(10), 1543-1558.

Yücel, M., Gartman, A., Chan, C.S., Luther III, G.W., 2011. Hydrothermal vents as a kinetically stable source of iron-sulphide-bearing nanoparticles to the ocean. *Nature Geoscience*, 4(6), 367-371.

Zhang, Q., Amor, K., Galer, S.J., Thompson, I., Porcelli, D., 2018. Variations of stable isotope fractionation during bacterial chromium reduction processes and their implications. *Chemical Geology*, 481, 155-164.

Zhang, Q., Amor, K., Galer, S.J., Thompson, I., Porcelli, D., 2019. Using stable isotope fractionation factors to identify Cr (VI) reduction pathways: metal-mineral-microbe interactions. *Water Research*. 151, 98-109.

Zhang, R., John, S.G., Zhang, J., Ren, J., Wu, Y., Zhu, Z., Liu, S., Zhu, X., Marsay, C.M., Wenger, F., 2015. Transport and reaction of iron and iron stable isotopes in glacial meltwaters on Svalbard near Kongsfjorden: From rivers to estuary to ocean. E*arth and Planetary Science Letters*, 424, 201-211.

Zhu, X.K., Guo, Y., Williams, R.J.P., O'nions, R.K., Matthews, A., Belshaw, N.S., Canters, G.W., De Waal, E.C., Weser, U., Burgess, B.K., Salvato, B., 2002. Mass fractionation processes of transition metal isotopes. *Earth and Planetary Science Letters*, 200(1-2), 47-62.

Zink, S., Schoenberg, R., Staubwasser, M., 2010. Isotopic fractionation and reaction kinetics between Cr (III) and Cr (VI) in aqueous media. *Geochimica et Cosmochimica Acta*, 74(20), 5729-5745.